eXPRESS Polymer Letters Vol.7, No.9 (2013) 722
Available online at www.expresspolymlett.com
DOI: 10.3144/expresspolymlett.2013.69

Editorial corner – a personal view

Cyanate ester resins – 'old newcomers' among high performance composite materials

A. Toldy[*]

Department of Polymer Engineering, Faculty of Mechanical Engineering, Budapest University of Technology and Economics, Műegyetem rkp. 3., H-1111 Budapest, Hungary

Among high performance and high temperature resistant thermosetting polymer materials, cyanate ester resins offer numerous advantages over the widely used commodity resins. Due to the high aromatic content of the monomer and the cured polymer, they possess higher glass transition temperatures (T_g) than epoxy resins (up to 400°C), while the triazine ring formed during addition polymerization is responsible for high thermal stability, high char yield and low smoke generation. Balanced dipoles in the cured state and absence of hydrogen bonding functionality provide further important advantages as low dielectric properties and low moisture absorption. This latter is one of the most significant advantages, as high water uptake would plasticize the resins, lower the T_g value and thus limit the hot/wet service temperature of it. As for the mechanical properties, the relatively low crosslink density and high free volume is responsible for appropriate toughness. These properties can be further fine-tuned through backbone structure (using different linking groups between the aromatic rings of the monomer) or by blending them with other polymers as epoxy resins, phenolic resins, bismaleimides, benzoxazines. Further advantage of the cyanate ester resins is that they can be processed using the same composite preparation methods (resin transfer moulding (RTM), vacuum-assisted resin transfer moulding (VARTM), moulding, filament winding, prepregging) as epoxy resins. But in comparison to epoxy resins, they offer greater dimensional stability due to reduced outgassing during the addition type polymerization reaction.

Despite the listed advantages and the fact that they were commercialized already in 1976, cyanate esters are still considered as relative newcomers in the composite industry. The reason behind is not only their relatively high cost (approximately twice as high performance epoxy resins), but also lack of formulation knowledge (moisture sensitivity of the uncured resin, toughness). Moisture sensitivity of the cyanate ester curing process is a known issue: the hydrolysis of the cyanate function leads to formation of carbamates, decomposing to amine and CO_2 over 190°C, resulting in voids in the composite structure, decrease in mechanical properties, lower crosslink density and T_g. The use of rapidly developing process analytical technologies during composite preparation (e.g. in-line fibre-optic-coupled Raman spectrometric monitoring of the curing reaction and moisture uptake with possible feedback to process parameters itself) may offer a key to overcome these problems and facilitate the headway of cyanate esters in high-tech composite applications.

Dr. Andrea Toldy
Member of Executive Editorial Board

---

[*]Corresponding author, e-mail: atoldy@mail.bme.hu

eXPRESS Polymer Letters Vol.7, No.9 (2013) 723–732
Available online at www.expresspolymlett.com
DOI: 10.3144/expresspolymlett.2013.70

Synthesis, characterization and properties of Se nanowires intercalated polyaniline/Se nanocomposites

Shumaila[1,2], *M. Alam*[2], *A. M. Siddiqui*[1], *M. Husain*[1,3*]

[1]Department of Physics, Faculty of Natural Sciences, Jamia Millia Islamia, 110025 New Delhi, India
[2]Department of Applied Sciences and Humanities, Faculty of Engineering and Technology, Jamia Millia Islamia, 110025 New Delhi, India
[3]Centre for Nanoscience & Nanotechnology, Jamia Millia Islamia, 110025 New Delhi, India

Received 27 February 2013; accepted in revised form 16 May 2013

Abstract. Present work reports novel synthesis of Polyaniline (PANI)/Se nanocomposites. Se nanowires are prepared from SeO_2 under assistance of vitamin C and polyaniline is synthesized through chemical oxidation. The effect of composition of Se nanowires on the properties of polyaniline was investigated and five orders increase in conductivity after doping has been observed. The electrical properties of nanocomposites show that conduction is through hopping process due to the wide range of localized states present near fermi level. FTIR (Fourier Transform Infrared spectroscopy) and ultraviolet (UV)-visible studies confirm the occurrence of polyaniline in conducting emeraldine salt form in the composites and suggest incorporation of Se in polymer. The optical studies indicate that absorption mechanism is due to indirect allowed transition and the optical band gap tends to decrease after doping. The thermal stability of composites has been ascertained on the basis of DSC (Differential Scanning Calorimetery) measurements. TEM (Transmission Electron Microscopy) and SEM (Scanning Electron Microscopy) analysis have also been carried out for morphological studies.

Keywords: *polymer composites, DC conductivity, FTIR, UV-visible, thermal properties*

1. Introduction

In recent years, with the rapid development of nanotechnology and composite materials, polyanline (PANI) nanocomposites have attracted considerable interest. PANI is one of the most promising conducting polymers due to its high conductivity, easy preparation, good environmental stability and large variety of applications [1]. Unlike other conjugated polymers, PANI has a simple and reversible acid/base doping/dedoping chemistry, enabling control over properties such as solubility, electrical conductivity and optical activity [2].

Polymer nanocomposites show quite different properties from the constituent materials due to interfacial interactions between nanostructured semiconductors and polymers. Synthesis of PANI based nanocomposites has led to a number of potential applications in electronic and optical devices, catalysis and analytical sensors etc. Some examples of these PANI nanocomposites are PANI/TiO_2, PANI/MnO_2, PANI/Ag, PANI/CdS, PANI/Poly(vinyl chloride) etc. [3–7]. However, studies on the interactions between PANI and chalcogenide nanoparticles are scarce. In our previous work, interactions of bulk Se with PANI have been reported [9]. To the best of our knowledge, Se nanowires containing polyaniline nanocomposites have not been reported elsewhere till now. Among chalcogenides Se nanoparticles have triggered great interest in researchers and therefore numbers of methods have been exploited for their synthesis and they have been widely used in electrical rectifiers, photocells, photographic

---

[*]Corresponding author, e-mail: mush_reslab@rediffmail.com

exposure meters, xerography etc. [8]. We have employed a template free two step process to prepare Se nanowires. We believe that utilization of Se nanowires with polyaniline can result in a new material with useful properties. In this communication, we report synthesis, characterization and properties of PANI/Se nanocomposites.

2. Experimental

2.1. Materials

Aniline (Merck India, AR grade) refrigerated after distillation, Ammonium peroxodisulphate (APS) (Merck India, AR grade), Hydrochloric acid (Qualigens Fine Chemicals, LR grade), Ammonia solution in water (99%, Merck India), Chloroform (Merck India, Spectroscopic Grade), SeO_2 (Merck India, AR Grade) and β-cyclodextrin (Merck), Ascorbic acid (Sigma-Aldrich) and Ethanol (Merck) were used as such without further purification.

2.2. Synthesis and doping of polyaniline

PANI was synthesized through oxidative polymerization under assistance of APS [10]. APS was added to the acidified solution of aniline, followed by constant stirring for 12 hours at temperature between 0–5°C. A green colored powder, emeraldine salt (ES), was obtained which is the conducting form of polyaniline. This ES was then converted to insulating blue emeraldine base (EB) by treating with liquid ammonia and washed several times with distilled water and finally dried in the oven to a powdered form.

2.3. Synthesis of Se nanowires

Se nanowires were synthesized by using Ascorbic Acid as reducing agent for SeO_2 under the assistance of β-cyclodextrin followed by dispersion in ethanol in a room temperature synthesis method [11]. In this procedure, SeO_2 and β-cyclodextrin were dissolved in distilled water. The solution was promptly added to vitamin C (L-ascorbic acid) solution. After 4 h of reaction, product was collected by centrifugation followed by washing with distilled water. Gray colored Se nanowires of average diameter 60±15 nm and upto several micrometers in length (see Figures 3 and 4) were obtained in this procedure. The chemical reaction may be represented by Equations (1) and (2):

$$SeO_2 + H_2O \rightarrow H_2SeO_3 \qquad (1)$$

$$H_2SeO_3 + 2C_6H_8O_6 \rightarrow 2C_6H_6O_6 + 3H_2O_3 + Se \qquad (2)$$

2.4. Synthesis of nanocomposites

Finally dried emeraldine base was chemically doped with different concentrations of Se nanowires at room temperature. Se nanowires were ultrasonically dispersed in chloroform for 10 min at room temperature and added to swollen PANI (swollen by the effect of solvent). This solution was stirred for 24 h at room temperature in different ratios (80:20, 85:15, 90:10, 95:10, and 97.5:2.5 by weight). The doped PANI/Se nanocomposites were dried and grinded for making the samples. Samples were prepared in the form of pellets by using hydraulic press at a pressure of 767 kPa.

2.5. Characterization

Electrical conductivity of the pellets was measured in the temperature range of 300–450 K. The pellets were placed between two steel electrodes, fixed inside a metallic sample holder for conductivity measurements. A voltage of 1.5 V (through regulated DC supply) was applied to the pellet and resulting current was measured with a Keithley Electrometer model 6157A. The temperature measurements were done through a calibrated chromel alumel thermocouple mounted near the samples. Annealing of the samples was done before conductivity measurements at a vacuum of 10^{-3} Torr to avoid the effect of moisture absorption. Thermal analysis was carried out by Differential Scanning Calorimeter (Model-DSC plus, Rheometric Scientific Co. UK). The temperature precision of this equipment is ±0.1°C. DSC scans were taken for undoped and Se nanowires doped PANI at 10°C/min heating rates. The temperature range covered in DSC was from room temperature to 180°C. Undoped and doped nanocomposites were dissolved in chloroform to measure UV-visible absorption spectra using a Camspec M-550 double beam scanning UV-visible spectrophotometer. Scanning Electron Microscopy (SEM) was used to study the morphology of the sample using JEOL JSM 6380 SEM. Transmission Electron Microscopy (TEM) used to for the structural analysis of Se nanowires using FEI Tecnai G2 HRTEM at 200 kV. Samples for TEM were prepared by dropcasting a dispersion of Se nanowires onto a carbon coated copper grid. Fourier Transform Infrared (FTIR) spectra of undoped and doped PANI/Se-KBr pellets were obtained by using Perkin Elmer FTIR spectrometer in the range from 400 to 4000 cm^{-1} at a resolution of 4 cm^{-1}.

3. Results and discussion

The DC conductivity of both undoped and doped composites is in good agreement with the Arrhenius relation [12], shown by Equation (3):

$$\sigma = \sigma_0^{(-\Delta E/k_b T)} \qquad (3)$$

where ΔE is the activation energy, k_b is Boltzmann constant; T is temperature and σ_0 is the pre-exponential factor. The Arrhenius plots of conductivity of all the samples are shown in Figure 1. It is evident from this figure that conductivity increases exponentially with temperature. The DC conductivity of undoped PANI is found to be 1.27×10^{-8} S/cm. On doping with different levels of Se nanowires, conductivity increases from 10^{-8} to 10^{-3} S/cm attaining a maximum value in 10% (w/w) doped sample and then reducing in 20% (w/w) doped sample. If we compare these results with bulk Se doped PANI [9], we find a remarkable increase in σ and decrease in activation energy on addition of Se nanowires to PANI. This increase in conductivity after doping may be due to increase in the number of polarons formed during the doping process. The electrical conductivity of conducting polymers results from mobile charge carriers introduced into the electronic system through doping. At low doping levels these charge carriers are self-localized and form nonlinear configurations. Because of large interchain transfer integrals, the transport of charge is believed to be principally along the conjugated chains, with interchain hopping as a necessary condition [13, 14] The nonlinear formation may be more in the case of heavy doping of 15% (w/w) doped composite, due to which it exhibits lesser conductivity than 10% (w/w) doped polymer and continues to decrease up to 20% (w/w) doped sample.

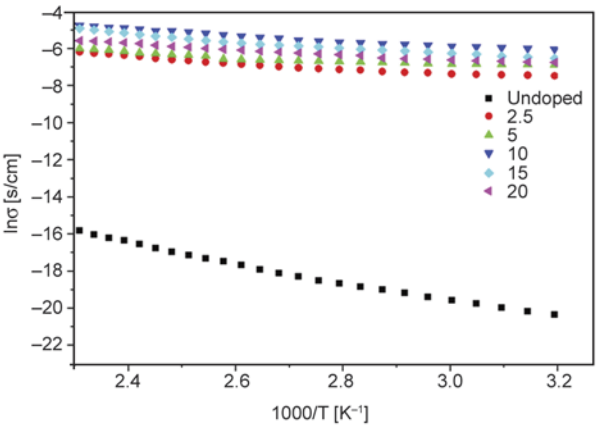

Figure 1. Temperature dependence of DC conductivity in the temperature range (300–450) K for undoped PANI and PANI/Se nanocomposites with different concentrations of Se nanowires (w/w)

The Arrhenius plot of σ is a straight line, which indicates that conduction in samples is taking place via an activated process, having single activation energy in the temperature range 300–450 K. The values of σ_0, ΔE and σ of the undoped and doped PANI samples have been calculated and are given in Table 1. It is clear from data that activation energy decreases after doping. The concentration dependent DC conductivity and activation energy values of all samples are shown in Figure 2. An increase in DC conductivity with corresponding decrease in activation energy is found to be associated with a shift of Fermi level in doped samples [15]. From a single value of activation energy, it is clear that the conduction is through the carrier concentration at the Fermi level. But the activation energy (ΔE) alone does not provide any information whether the conduction takes place in extended states or by hopping in localized states. This can be explained on the basis of the values of pre-exponential factor (σ_0). According to Mott and Davis [16, 17] value of σ_0 in the range 10^3–10^4 S·cm^{-1} indicates that the

Table 1. Electrical and optical parameters for PANI/Se nanocomposites doped with different concentrations of Se at temperature 350 K

S. No.	Samples	DC conductivity (σ_{dc}) [S·cm^{-1}]	Activation energy (ΔE) [eV]	Pre-exponential factor (σ_0) [S·cm^{-1}]	Optical band gap (E_g) [eV]	Extinction co-efficient (k) (at 550 nm)
1.	Undoped PANI	$1.27\cdot10^{-8}$	0.62	7.54	2.06	36.80
2.	2.5% doped PANI	$1.28\cdot10^{-3}$	0.13	$9.6\cdot10^{-2}$	1.77	13.73
3.	5% doped PANI	$1.87\cdot10^{-3}$	0.11	$7.06\cdot10^{-2}$	1.69	11.35
4.	10% doped PANI	$6.34\cdot10^{-3}$	0.12	$3.10\cdot10^{-1}$	1.59	32.18
5.	15% doped PANI	$4.50\cdot10^{-3}$	0.14	$9.80\cdot10^{-1}$	1.45	26.99
6.	20% doped PANI	$2.68\cdot10^{-3}$	0.16	$8.95\cdot10^{-1}$	1.56	31.36

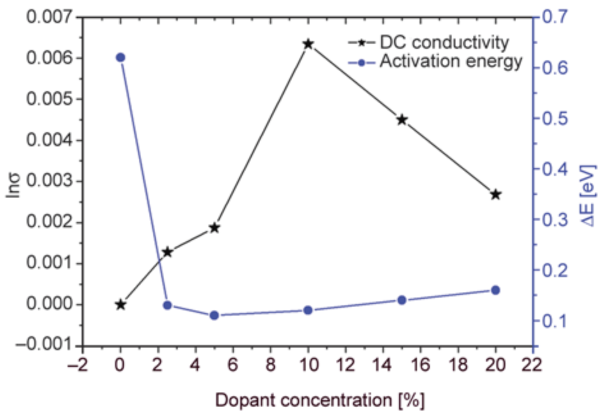

Figure 2. Variation of DC conductivity (lnσ) and activation energy (ΔE) versus undoped and doped PANI composites with different concentration of Se nanowires (w/w)

conduction takes place mostly in extended states. A smaller value of σ_0 indicates a wide range of localized states and the conduction is taking place by hopping process. In our case, the values of σ_0 are found to lie between the orders of $10–10^{-2}$. Therefore, the conduction takes place by the hopping process due to wide range of localized states present in the sample. From the above results we may conclude that hopping mechanism is responsible for conduction in all of the nanocomposites. A smaller value of σ_0 also designates that the density of defect states increases in the sample and further supports our argument that the conduction mostly takes place by hopping process in all the composites.

Figures 3a, 3b show SEM and 3c, 3d show TEM images of Se nanowires. The nanowires are aesthetically dispersed in a uniform manner. These nanowires have an average diameter of 60±15 nm with length upto several micrometers. Figure 4 shows the SEM micrograph of undoped PANI and PANI/Se nanocomposites in different compositions (w/w). These images depict that the doping of Se nanowires has a strong effect on PANI's morphology and with the increase of dopant contents, a transformation in morphology of PANI particles is observed. Figure 5 shows TEM image of 10% (w/w) doped PANI/Se nanocomposite which confirms encapsulation of Se nanowires by polymer. Figure 4a is typical SEM image of undoped PANI, when we compare it with the SEM images of composites, there we discover exfoliated dispersion of dopant in polymer giving rise to formation of intercalated nanocomposites (Figure 4b, 4c and 4d) and the size of polymer particles also increases upto the 10% (w/w) doped sample favouring the increase in conductivity up to this level of composition. At higher concentration, the particle size does not increase appreciably (Figure 4e). The cluster size is found to reduce at 20% concentration of nanowires which is evident from (Figure 4f).

FTIR spectra of all the PANI/Se composites are shown in Figure 6. The five characteristic bands of PANI at 1580 cm^{-1} (assigned as C–C stretching of the quinoid rings), 1502 cm^{-1} (C–C stretching of benzenoid rings), 1300 cm^{-1} (C-N stretching mode), 1130 cm^{-1} (N–Q–N, where Q represents the quinoid ring) and 800 cm^{-1} (out-of-plane bending vibration of C–H on para-disubstituted rings) have been observed in the FTIR spectra of PANI/Se nanocomposites. This indicates that the spectrum of nanocomposites is identical to the emeraldine salt form of PANI [18]. Relative intensities of PANI bands decrease with decreasing PANI contents. Subsequently Se and Se containing organic compounds demonstrates absorption in far-infrared region only and do not exhibit specific absorption bands in the region between 400 and 4000 cm^{-1} of spectra. Se–Se stretching vibration shows absorption at 285 cm^{-1}. A new inherent peak at 830 cm^{-1} is observed in spectra of all of the nanocomposites. Pure PANI does not give absorption at this frequency. It is suggested that 830 cm^{-1} peak is an overtone of Se–Se stretching vibration, which has its main absorption peak at 285 cm^{-1}. Thorough information on PANI-Se interactions can be obtained by using spectrometric equipment which provides spectral data on far IR region (200–400 cm^{-1}) [19]. Proposed scheme of the formation of PANI/Se nanocomposites is shown in Figure 7.

The UV–visible absorption and reflection spectra are given in Figure 8. The $\pi \rightarrow \pi^*$ transitions of aromatic ring gives an absorbance peak at λ around 365 nm whereas inter-band $\pi \rightarrow \pi^*$ transition of excitation in the aromatic ring demonstrates a peak at 295 nm. Both the peaks show red shift of about 10 nm after doping with the increase in the dopant concentration. Red shift usually occurs due to the change in $\pi \rightarrow \pi^*$ transitions. The relation between optical band gap E_g, absorption coefficient α and the energy $h\nu$ of the incident photon is given by Equation (4) [20]:

$$\alpha h\nu \propto (h\nu - E_g)^n \qquad (4)$$

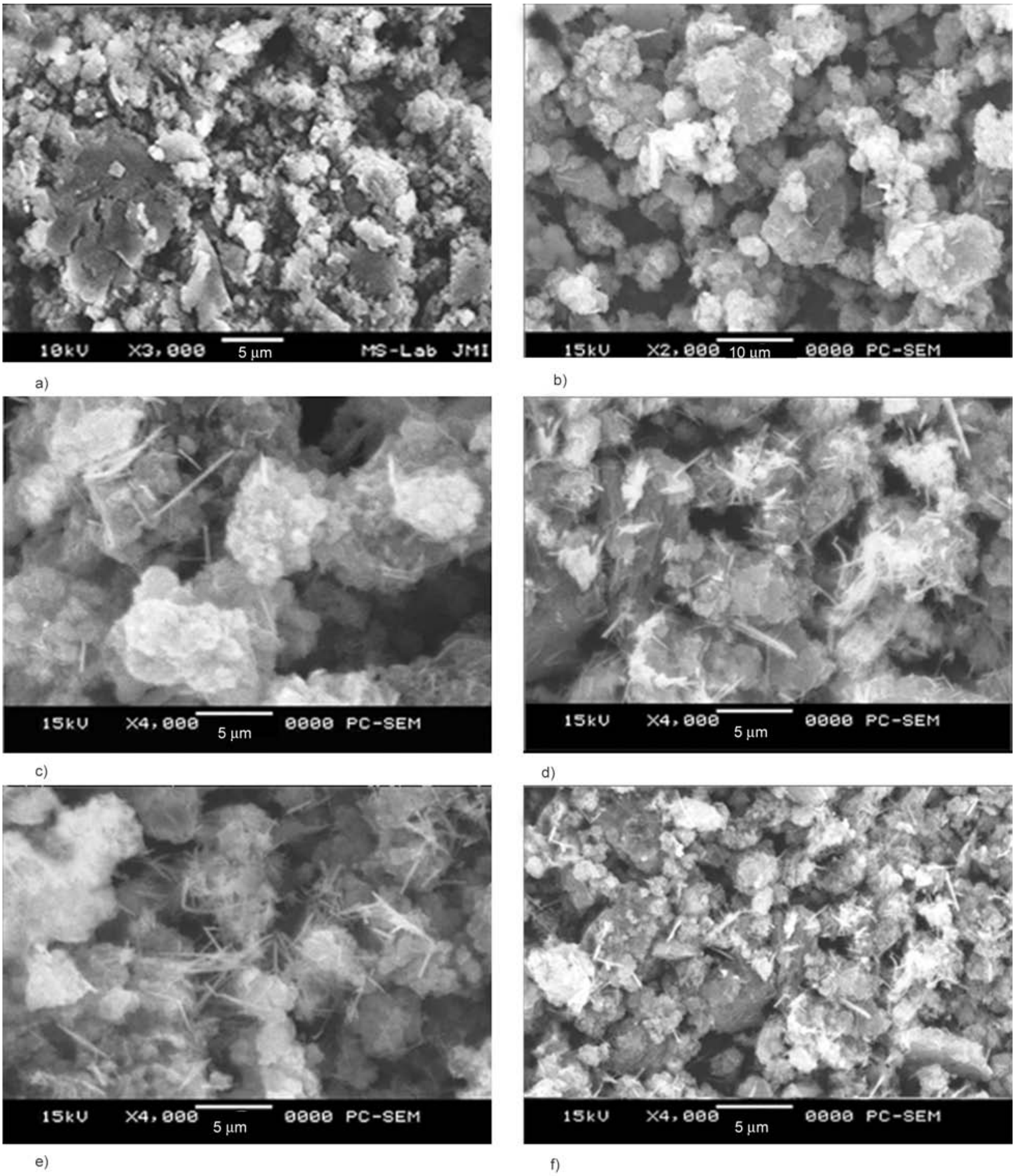

Figure 3. SEM images of PANI\Se nanocomposites with different contents of Se nanowires (a) 0, (b) 2.5, (c) 5, (d) 10, (e) 15 and (f) 20 wt%

The phonon absorption in many amorphous materials is found to obey the Tauc's relation (2).The index n has discrete values such as 1/2, 3/2, 2 or more depending on whether the transition is direct or indirect and allowed or forbidden, respectively. In the present case the photon energy is plotted against $\alpha h\nu$, for $n = 2$ it gives a straight line fit, which implies that the samples obey indirect transition. From the absorption spectra the band gaps of all the samples are estimated by plotting energy ($h\nu$) versus $(\alpha h\nu)^{1/2}$ (Figure 9). When compared to the undoped polymer, the optical band gaps of doped composites are found to decrease for all compositions. The decrease in band gap may occur due to the broadening of polaron bands, which is attributed to the increase in carrier concentration in

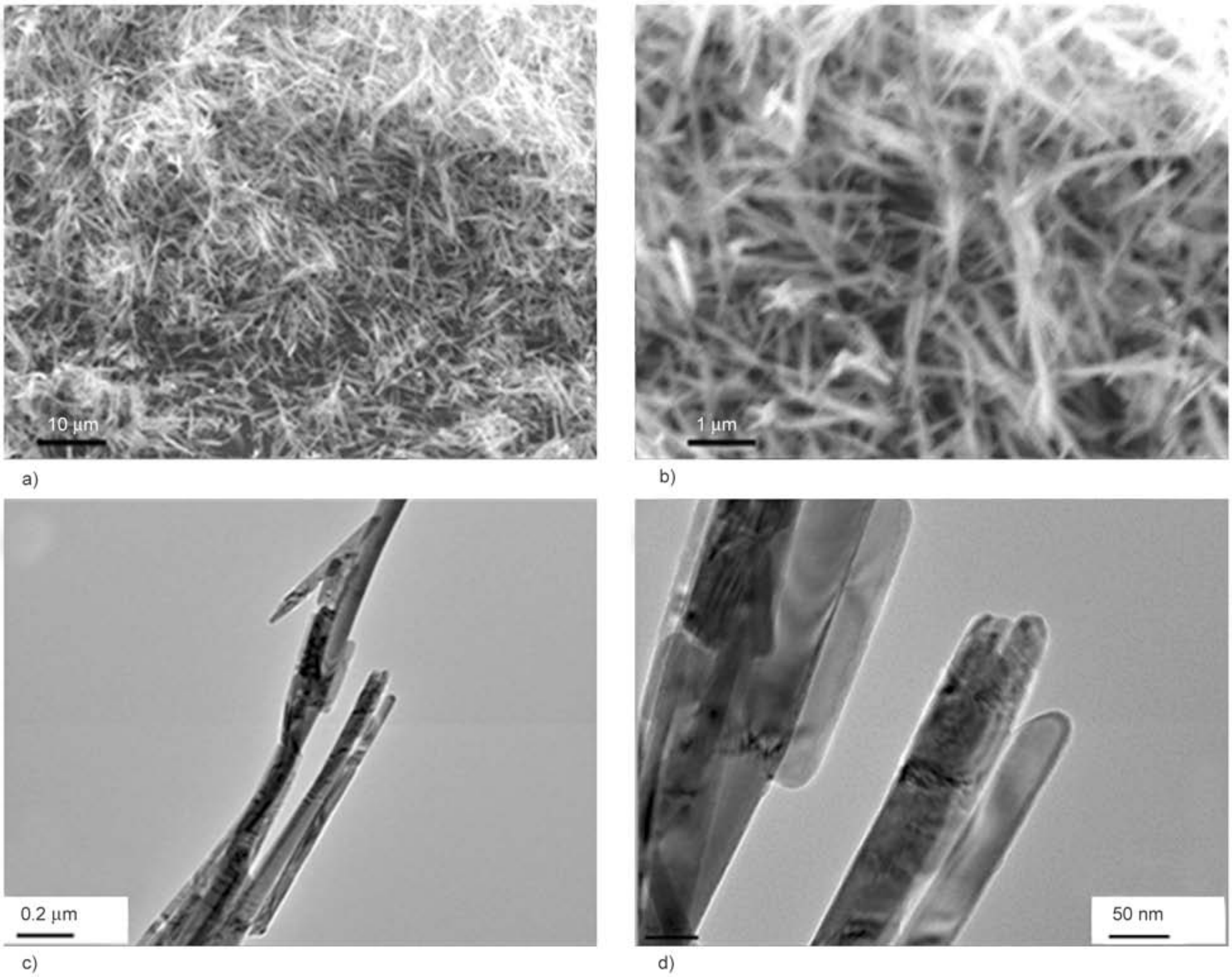

Figure 4. SEM micrographs of Se nanowires (a, b) and TEM of Se nanowires at different resolutions (c, d)

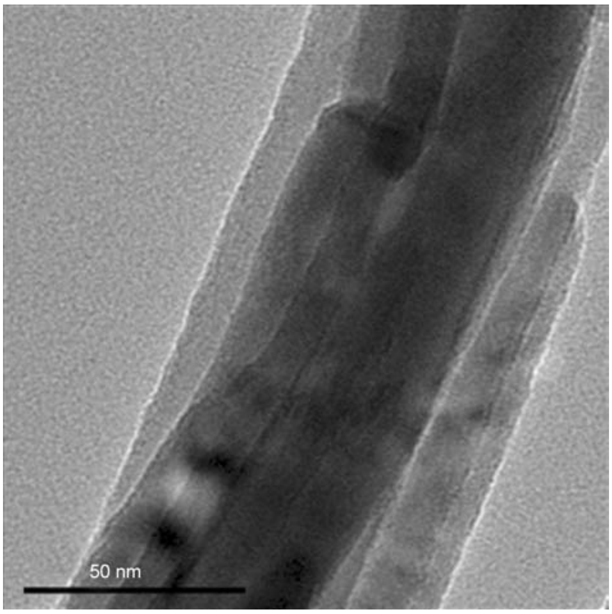

Figure 5. TEM of 10% (w/w) doped PANI/Se nanocomposite

the polymer after doping. The extinction coefficient (k) has been calculated using well known relation shown by Equation (5) [21]:

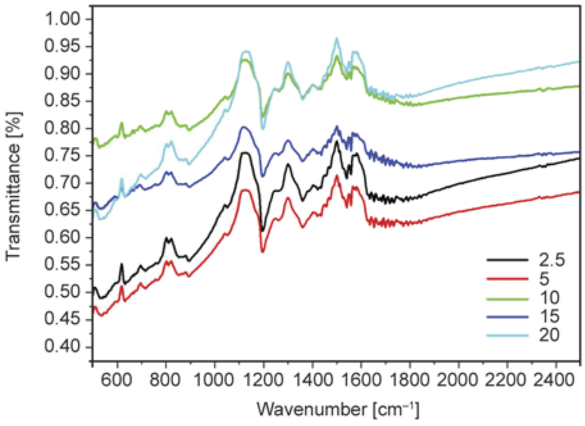

Figure 6. FTIR spectra of undoped and doped PANI at different Se nanowires concentrations (w/w)

$$k = \frac{\alpha\lambda}{4\pi} \tag{5}$$

where λ is the wavelength of the incident photon and α is the absorption coefficient. The optical parameters calculated from the UV-visible spectra are given in Table 1.

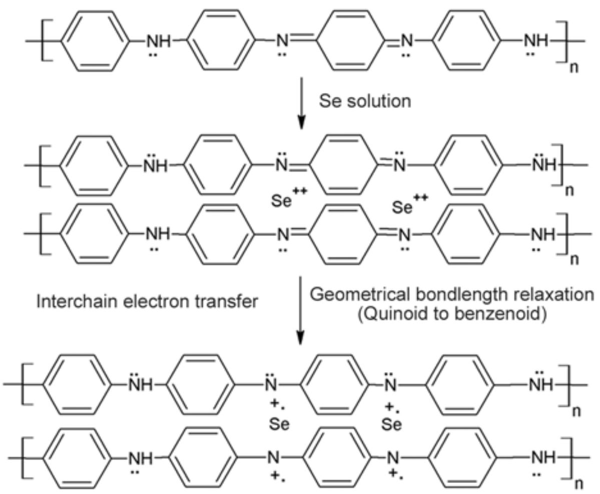

Figure 7. Schematic doping mechanism of PANI by Se

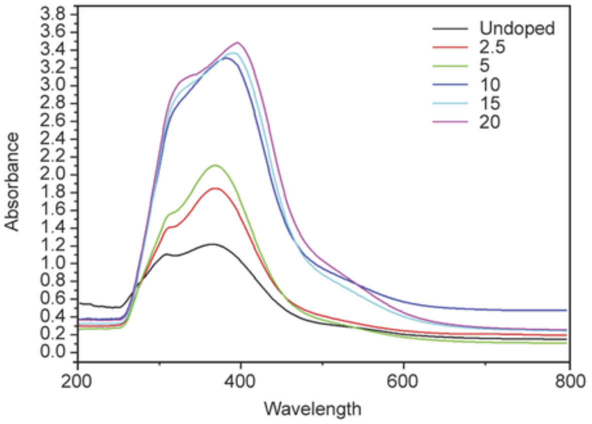

Figure 8. UV-visible absorption spectra of undoped PANI and PANI doped with different concentration of Se nanowires

Thermal properties of all the composites have been investigated by DSC study under non-isothermal conditions at heating rate of 10°C/min. Typical DSC curves for different samples are shown in Figure 10. The DSC traces of all the composites show single glass transition and single crystallization thus confirming the homogeneity of the material. Estimated values of glass transition temperature (T_g), crystallization temperature (T_c) and enthalpy change of the reaction (ΔH) are given in Table 2. It has been observed that T_g and T_c increase after doping. The increase in T_g may be explained on the basis of the fact that when dopant is added to polymer, it forms cross links between chains, owing to which the matrix become heavily cross linked and the steric-hindrance increases. This further makes the system more rigid and retards the tendency of crystallization. This rigid structure requires higher energy for softening and therefore T_g and T_c are observed at higher temperatures.

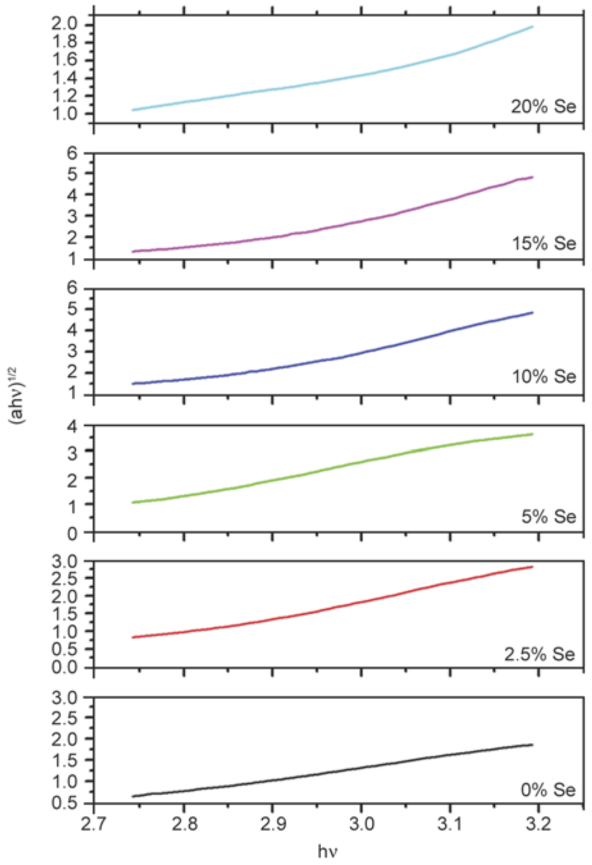

Figure 9. The photon energy ($h\nu$) versus $(\alpha h\nu)^{1/2}$

Thermal stability of the samples has been ascertained through the $T_c - T_g$ difference. It is clear from Figure 11 that the value of $T_c - T_g$ increases up to 10% (w/w) doped composites; after this concentration a slight decrease is observed in $T_c - T_g$ values. Therefore, 10% (w/w) doped PANI/Se is the most stable composition among all other studied samples. In the non-isothermal study, the stability is usually investigated in terms of two independent factors. The first has already been discussed ($T_c - T_g$) and other is the heat content of the samples, i.e. enthalpy. The experimental evaluation of the crystallization enthalpy (ΔH_c) has been determined by measuring the area under the peak and converted into Joul through the use of instrument constant using the formula [22] (Equation (6)):

$$\Delta H_c = \frac{KA}{M} \tag{6}$$

where A is the area of crystallization peak, M is the mass of sample and K is the instrument constant which is found to be 1.2. It is observed that ΔH_c decreases with the increase in Se concentration because the samples being in the metastable state try to minimize its enthalpy as well as Gibbs free

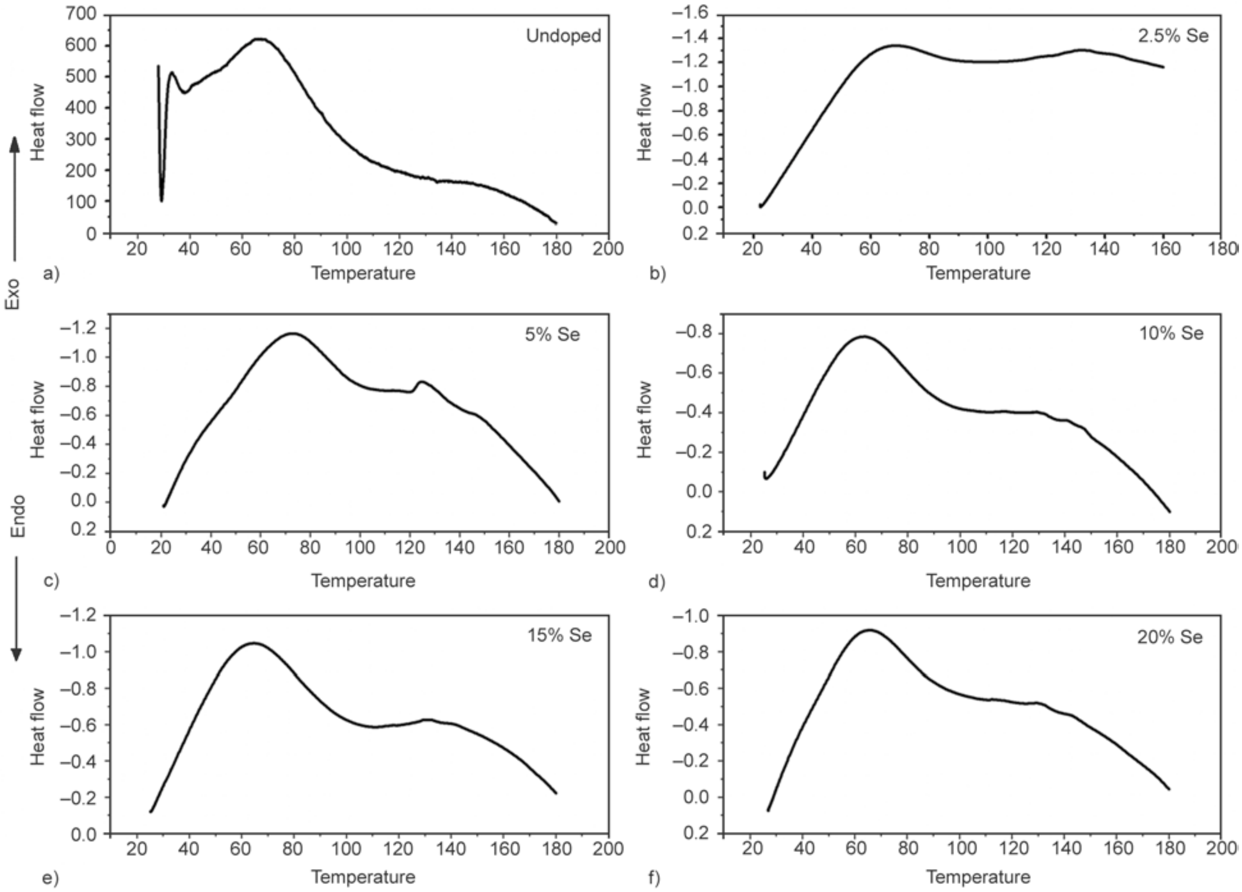

Figure 10. DSC curves for all samples at heating rate 10°C/min (a) Undoped, (b) 2.5%, (c) 5%, (d) 10%, (e) 15%, (f) 20% Se nanowires doped PANI samples

Table 2. Thermal parameters of all samples at heating rate 10°C/min

S. No	Samples	T_c [°C]	T_g [°C]	ΔH_c [J/g]
1.	Undoped PANI	33±0.1	65±0.1	103.94±0.1
2.	2.5% doped PANI	46±0.1	101±0.1	85.63±0.1
3.	5% doped PANI	47±0.1	120±0.1	57.24±0.1
4.	10% doped PANI	43±0.1	124±0.1	28.76±0.1
5.	15% doped PANI	44±0.1	112±0.1	30.95±0.1
6.	20% doped PANI	45±0.1	123±0.1	30.38±0.1

energy at every temperature by elementary atomic motion to gain stability. The most stable composite will release the least energy to gain stability, as it already possesses a stable atomic configuration. Therefore, the most stable composite will have the least value of ΔH_c. In our case least value of ΔH_c corresponds to 10% (w/w) doped sample. Hence this composition (10% (w/w)) is most stable among all of the compositions of the series which is also confirmed from $T_c - T_g$ plots. The change in enthalpy and $T_c - T_g$ verses dopant concentration is shown in Figure 11.

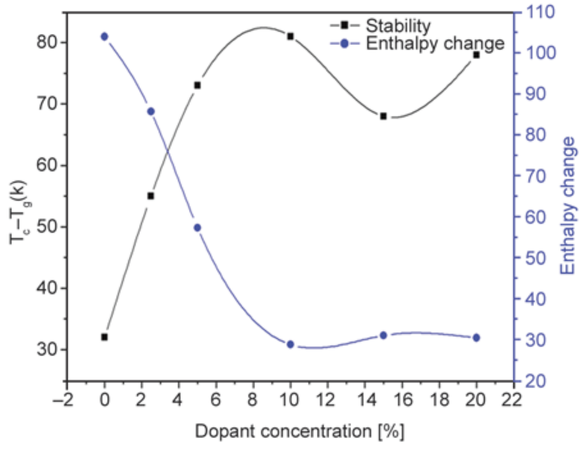

Figure 11. Variation of $T_c - T_g$ and enthalpy change (ΔH_c) vs. PANI/Se nanocomposites in different compositions (w/w)

4. Conclusions

The semiconducting polyaniline and Se nanowires were successfully synthesized and PANI/Se nanocomposites were produced with different concentrations of Se. It has been observed that the conductivity increases by five orders of magnitude after doping. Conduction mechanism has been explained on the basis of pre-exponential factor range. SEM images show that dopant has been dispersed in polymer matrix and formation of clusters takes place supporting the variation in DC conductivity. The optical studies indicate that absorption mechanism is due to indirect allowed transition and optical band gap was found to decrease after doping. FTIR spectra corroborate the structural changes of PANI after doping of Se and confirm the presence of polyaniline in the form of conducting emeraldine salt. Stability of the composites has been explained on the basis of variation in $T_c - T_g$ and ΔH_c, which confirms that PANI/Se composites containing 10% Se (w/w) is most stable among all the nanocomposites. A similar trend in properties has also been observed in band gap measurements, SEM and DC conductivity measurements. Thus, we may conclude that Se nanowires doping has superior effect on properties of PANI in comparison to its bulk counterpart.

Acknowledgements

One of the Authors, Shumaila, is thankful to University Grants Commission (UGC) for providing financial support in the form of Senior Research Fellowship (MANF-SRF).

References

[1] Wang S. X., Sun L. X., Tan Z. C., Xu F., Li Y. S.: Synthesis, characterization and thermal analysis of polyaniline (PANI)/Co_3O_4 composites. Journal of Thermal Analysis and Calorimetry, **89**, 609–612 (2007).
DOI: 10.1007/s10973-006-7569-3

[2] Xia Y., Wiesinger J. M., McDiarmid A. G., Epstein A. J.: Camphorsulfonic acid fully doped polyaniline emeraldine salt: Conformations in different solvents studied by an ultraviolet/visible/near-infrared spectroscopic method. Chemistry of Materials, **7**, 443–445 (1995).
DOI: 10.1021/cm00051a002

[3] Li X., Chen W., Bian C., He J., Xu N., Xue G.: Surface modification of TiO_2 nanoparticles by polyaniline. Applied Surface Science, **217**, 16–22 (2003).
DOI: 10.1016/S0169-4332(03)00565-8

[4] Biswas M., Ray S. S., Liu Y.: Water dispersible conducting nanocomposites of poly(*N*-vinylcarbazole), polypyrrole and polyaniline with nanodimensional manganese (IV) oxide. Synthetic Metals, **105**, 99–105 (1999).
DOI: 10.1016/S0379-6779(99)00049-1

[5] Zhou H. H., Ning X. H., Li S. L., Chen J. H., Kuang Y. F.: Synthesis of polyaniline-silver nanocomposite film by unsymmetrical square wave current method. Thin Solid Films, **510**, 164–168 (2006).
DOI: 10.1016/j.tsf.2005.12.310

[6] Chandrakanthi R. L. N., Careem M. A.: Preparation and characterization of CdS and Cu_2S nanoparticle/polyaniline composite films. Thin Solids Film, **417**, 51–56 (2002).
DOI: 10.1016/S0040-6090(02)00600-4

[7] Zhou Z., Cai N., Zhou Y.: Capacitive of characteristics of manganese oxides and polyaniline composite thin film deposited on porous carbon. Materials Chemistry and Physics, **94**, 371–375 (2005).
DOI: 10.1016/j.matchemphys.2005.05.018

[8] Cao X. B., Xie Y., Zhang S. Y., Li F. Q.: Ultra-thin trigonal selenium nanoribbons developed from series-wound beads. Advanced Materials, **16**, 649–653 (2004).
DOI: 10.1002/adma.200306317

[9] Shumaila, Lakshmi G. B. V. S., Alam M., Siddiqui A. M., Zulfequar M., Husain M.: Synthesis and characterization of Se doped polyaniline. Current Applied Physics, **11**, 217–222 (2011).
DOI: 10.1016/j.cap.2010.07.010

[10] Wei Y., Jang G-W., Hsuesh K. F., Scherr E. M., MacDiarmid A. G., Epstein A. J.: Thermal transitions and mechanical properties of films of chemically prepared polyaniline. Polymer, **33**, 314–322 (1992).
DOI: 10.1016/0032-3861(92)90988-9

[11] Li Q., Yam V. W-W.: High-yield synthesis of selenium nanowires in water at room temperature. Chemical Communications, **9**, 1006–1008 (2006).
DOI: 10.1039/B515025F

[12] Khan Z. H., Malik M. M., Zulfequar M., Husain M.: Electrical conduction mechanism in a-$Se_{80-x}Te_xGa_{20}$ films (0<or=x<or=20). Journal of Physics Condensed Matter, **7**, 8979–8991 (1995).
DOI: 10.1088/0953-8984/7/47/017

[13] Grant P. M., Batra I. P.: Band structure of polyacetylene, $(CH)_x$. Solid State Communications, **29**, 225–229 (1979).
DOI: 10.1016/0038-1098(79)91043-3

[14] Fink J., Leising G.: Momentum-dependent dielectric functions of oriented *trans*-polyacetylene. Physical Review B, **34**, 5320–5328 (1986).
DOI: 10.1103/PhysRevB.34.5320

[15] Okano S., Suzuki M., Imura K., Fukada N., Hiraki A.: Impurity effects of some metals on electrical properties of amorphous $As_2Se_1Te_2$ films. Journal of Non Crystalline Solids, **59–60**, 969–972 (1983).
DOI: 10.1016/0022-3093(83)90330-7

[16] Mott N. F., Davis E. A.: Electronic process in non crystalline materials. Clarendon, Oxford (1979).

[17] Davis E. A., Mott N. F.: Conduction in non-crystalline systems V. Conductivity, optical absorption and photoconductivity in amorphous semiconductors. Philosophical Magazine, **22**, 903–922 (1970).
DOI: 10.1080/14786437008221061

[18] Asturias G. E., MacDiarmid A. G., MacCall R. P., Epstein A. J.: The oxidation state of 'emeraldine' base. Synthetic Metals, **29**, 157–162 (1989).
DOI: 10.1016/0379-6779(89)90291-9

[19] Bormashenko E., Pogreb R., Sutovski S., Shulzinger A., Sheshnev A., Gladkikh A.: Preparation of Se-doped polyaniline emeraldine base films. Synthetic Metals, **139**, 321–325 (2003).
DOI: 10.1016/S0379-6779(03)00182-6

[20] Sharma T., Aggarwal S., Kumar S., Mittal V. K., Kalsi P. C., Manchanda V. K.: Effect of gamma irradiation on the optical properties of CR-39 polymer. Journal of Materials Science, **42**, 1127–1130, (2007).
DOI: 10.1007/s10853-006-0516-7

[21] Elliot S. R.: A unified model for reversible photostructural effects in chalcogenide glasses. Journal of Non-Crystalline Solids, **81**, 71–98 (1986).
DOI: 10.1016/0022-3093(86)90260-7

[22] Imran M. M. A., Saxena N. S., Bhandari D., Husain M.: Glass transition phenomena, crystallization kinetics and enthalpy released in binary $Se_{100-x}In_x$ ($x = 2$, 4 and 10) semiconducting glasses. Physica Status Solidi, **181**, 357–368 (2000).
DOI: 10.1002/1521-396X(200010)181:2<357::AID-PSSA357>3.0.CO;2-H

eXPRESS Polymer Letters Vol.7, No.9 (2013) 733–746
Available online at www.expresspolymlett.com
DOI: 10.3144/expresspolymlett.2013.71

Guar gum/borax hydrogel: Rheological, low field NMR and release characterizations

T. Coviello[1], P. Matricardi[1], F. Alhaique[1], R. Farra[2], G. Tesei[2], S. Fiorentino[2], F. Asaro[3], G. Milcovich[3], M. Grassi[2*]

[1]Department of Drug Chemistry and Technologies, ‘Sapienza’, University of Rome, Piazzale Aldo Moro 5, 00185 Rome, Italy
[2]Department of Engineering and Architecture, University of Trieste, Piazzale Europa 1, 34127 Trieste, Italy
[3]Department of Chemical and Pharmaceutical Sciences, University of Trieste, Via Giorgeri 1, 34127 Trieste, Italy

Received 26 March 2013; accepted in revised form 19 May 2013

Abstract. Guar gum (GG) and Guar gum/borax (GGb) hydrogels are studied by means of rheology, Low Field Nuclear Magnetic Resonance (LF NMR) and model drug release tests. These three approaches are used to estimate the mesh size (ξ) of the polymeric network. A comparison with similar Scleroglucan systems is carried out. In the case of GGb, the rheological and Low Field NMR estimations of ξ lead to comparable results, while the drug release approach seems to underestimate ξ. Such discrepancy is attributed to the viscous effect of some polymeric chains that, although bound to the network to one end, can freely fluctuate among meshes. The viscous drag exerted by these chains slows down drug diffusion through the polymeric network. A proof for this hypothesis is given by the case of Scleroglucan gel, where the viscous contribution is not so significant and a good agreement between the rheological and release test approaches was found.

Keywords: *polymer gels, rheology, low field NMR, transport processes, mesh-size*

1. Introduction

Guar gum (GG) is a neutral galactomannan, extracted from the seeds of *Cyamopsis tetragonoloba*. It consists of a linear backbone of β(1→4)-linked D-mannopyranose units (Man) and with the presence of randomly attached α(1→6)-linked galactopyranose units (Gal) as side chains [1]. Due to the presence of these galactose units, the polymer is soluble in water [2]. The ratio of mannose to galactose units (M/G) depends on climate variations and ranges from 1.5:1 to 1.8:1. Because of its low cost and its ability to produce a highly viscous solution even at low concentrations, GG finds important applications in food [3], in oil recovery [4] and in personal care industries [5]. The high viscosity of GG solutions arises from the high molecular weight of GG (up to 2 million and further) [6] and from the presence of extensive intermolecular associations (entanglements) by means of hydrogen bonds.

In aqueous solution GG assumes a flexible coil conformation as evidenced by the Mark-Houwink-Sakurada exponent and by the relatively low value of its characteristic ratio and its persistence length [7]. GG, crosslinked with glutaraldehyde, was proposed for colon delivery [8], and it was also tested as a matrix for oral solid dosage forms [9].

Scleroglucan (SCLG), a water soluble polysaccharide produced by fungi of the genus Sclerotium, consists of a main chain of (1→3)-linked β-D-glucopyranosyl units bearing, every third unit, a single β-D-glucopyranosyl unit linked (1→6). It is known that SCLG assumes a triple-stranded helical confor-

---

[*] Corresponding author, e-mail: mariog@dicamp.univ.trieste.it

mation in aqueous solution and a single coiled disordered conformation in methylsulphoxide or at high pH values (NaOH > 0.2 M) [10, 11]. Due to its peculiar properties, SCLG was extensively used for various commercial applications (secondary oil recovery, ceramic glazes, food, paints, cosmetics, etc.) [12] and it was also investigated for modified/sustained release formulations and ophthalmic preparations [13].

Actually, it is well known that borax is an efficient crosslinker for polymers bearing hydroxyl groups but the type of formed linkages is still debated and so far two main models have been proposed. The most popular one implies the existence of pure chemical crosslinks between the polymeric chains and borax [14], and it was proposed for the GG/borax interactions. According to the other model, the borax ions hold together the polymeric chains by means of mixed physical/chemical linkages. This model was firstly proposed for poly-(vinyl-alcohol) [15] and it was recently suggested also for SCLG [16, 17].

The considerable effort devoted to the study of polymer-ion complexes is due to the wide range of application of these systems. In particular, the complex between GG and borate was previously studied by several authors [18, 19] that investigated the effect of polymer and borate concentration, temperature, environmental pH conditions, and GG molecular weight on the peculiar rheological properties detected by the frequency dependence of relaxation spectra. Furthermore, a detailed study of the crosslinking reaction of borate ion with polyhydroxy polymers was carried out by means of ^{11}B NMR spectroscopy on dilute mixtures of borate ions and GG, for the acquisition of further insight into the complexation mechanism. Thus, the values of complexation equilibrium constants and the complexation enthalpy at various measuring conditions were calculated [14, 20–22]. In addition, specific investigations on the rheological properties of the schizophyllan/borate system were reported (schizophyllan has the same repeating unit of SCLG) in other papers [23, 24]. It is interesting to note that both, GG and SCLG, interact with borax leading to a three-dimensional network that, besides the intrinsic differences between the two polymers (see below), shows a peculiar anisotropic elongation during swelling, when tablets of these two systems are prepared. In particular, GG and SCLG show important different characteristics: (a) GG dissolves in water as a random coil while SCLG exhibits a triple helix conformation in aqueous solution with a persistence length of about 200 nm [10, 25]; (b) borax promotes a rapid gelation of GG [26] by means of crosslinks characterized by a lifetime of the order of seconds [27], leading to self-healing properties of the network. On the other side, SCLG requires several hours for gelation in the presence of borax and no self-healing occurs. Nevertheless, both, GG and SCLG, in the presence of borax, are capable to give self-sustaining gels [28]. Furthermore, also the interaction with borax takes place in a different way. In the case of SCLG the borax promotes mixed (chemical and physical) interactions between triplexes; on the other side, in the case of GG the borax forms chemical bridges between chains by means of reversible linkages. In addition, molecular dynamics simulation and AFM images indicate that the borax groups increase the stiffness of GG making such system more similar to SCLG/borax (SCLGb). During the swelling the labile nature of the borax cross-links in the GG makes the interchain interactions able to undergo the needed rearrangement, similar to that of SCLG where full chemical bridges are not present. These similarities explain the quite unexpected parallel swelling behaviour of GG and SCLG, in the presence of borax [16, 28].

However, in all these previous research works, no attention was specifically focused on the estimation of the mesh sizes of the networks, a very important parameter for the numerous implications that it may have on these hydrogel systems when used for industrial and/or pharmaceutical applications.

In this frame, aim of the present work was to characterise GG and GG/borax (GGb) systems resorting to three different approaches, rheology, Low Field NMR (LF NMR) and release tests. In fact, the joint use of these approaches provides, for the first time at our best knowledge, more complete information about the polymeric chain architectures (polymeric networks), also in terms of mesh size estimation, and their possible modifications with temperature in physiological conditions (25 and 37°C). In addition, the characteristics of GG and GGb systems were compared with those of the SCLG and SCLGb systems.

2. Experimental section

2.1. Materials

Guar Gum (GG) was provided by CarboMer (San Diego, USA). The ratio between mannose and galactose was estimated by means of ^{1}H NMR (carried out at 70°C with a Brucker AVANCE AQS 600 spectrometer, operating at 600.13 MHz) and an M/G value of $\approx$1.5 was found. The molecular weight ($1.2\cdot10^6$) was estimated by means of viscometric measurements carried out at 25°C. Scleroglucan (SCLG) was provided by Degussa (Germany). The molecular weight ($1.1\cdot10^6$) was estimated by means of viscometric measurements carried out at 25°C in 0.01 M NaOH. For the viscosity measurements, an automatic viscometer (Instrument Schott AVS 370, Lauda, Germany) with a water bath (Lauda 0.15 T) allowing the temperature control to 0.1°C was used. An Ubbelohde capillary viscometer (Type No 531 01, with a capillary diameter = 0.54 mm, Schott-Geräte) for dilution sequences was used. The GG solutions were prepared in distilled water while the SCLG solutions were prepared in 0.01 N NaOH (in order to break possible aggregates). Before measurements, the samples were filtered twice with 1.2 μ Millipore filters. From the flux time of solvent and solutions the intrinsic viscosity, $[\eta]$ [cm^3/g], was estimated for each polymer. According to the Mark-Houwink-Sakurada equation, the intrinsic viscosity is related to the molar mass of the sample: $[\eta] = KM_w^a$, where K and a are constants for each polymer-solvent system at a given temperature. From the value of K and a found in the literature for the GG [11] and for the SCLG [7] samples, the molecular weight of the two polymers were evaluated.

Theophylline (TPH, molecular weight 198) and borax were Carlo Erba products (Italy), Vitamin B_{12} (Vit B_{12}, molecular weight 13 500) was purchased from Fluka (Germany). All other products and reagents were of analytical grade. Distilled water was always used.

2.2. Polymer purification

A given amount of polymer (GG and SCLG) was dissolved in distilled water (polymer concentration, c_p = 0.5% w/v). GG samples were kept under magnetic and mechanical stirring at 60°C for 24 h and then at room temperature for 24 additional hours [29]. SCLG samples were kept under magnetic and mechanical stirring for 24 h at room temperature. The resulting solutions were exhaustively dialysed at 7°C against distilled water with dialysis membranes of a cut-off 12 000–14 000 and then freeze dried. The lyophilized products were stored in a desiccator until use.

2.3. Hydrogel preparations

A given amount of GG or SCLG (200 mg for the release experiments and 35 mg for the rheological analysis and for NMR measurements; c_p = 0.7% w/v) was dissolved in water for 24 h. GG and SCLG crosslinking was carried out by addition of 0.1 M borax solution to the homogeneous polymer system in order to get a unitary value of the ratio between borax moles and moles of the repeating GG or SCLG units (r = 1). The resulting mixture was magnetically stirred for 5 min and then left for 2 days at 7°C for gel setting. For the release experiments, a known amount of model drug was first dissolved in water before the addition of the polymer.

2.4. Rheological characterization

The rheological characterization, carried out at 25 and 37°C, was performed by means of a controlled stress rheometer, Haake Rheo-Stress RS300 model, with a Thermo Haake DC50 water bath. Two geometries were used: a cone–plate device (C60/1 Ti with a cone diameter of 60 mm and a cone angle of 1° and a MP60 steel 8/800 plate with a diameter of 60 mm, Haake) for the GG and SCLG samples and a grained plate-plate device (Haake PP35/S: diameter = 35 mm; gap between plates = 1 mm) was used for the SCLGb and GGb samples in order to prevent wall slippage phenomena [30]. To perform the measurements on SCLGb and GGb, the hydrogels, obtained with a thickness of 1.0–3.0 mm, were removed with the aid of a small spatula from the beaker in which they had settled, and they were laid with care on the lower plate of the rheometer. The upper plate was then lowered until it reached the hydrogel surface. Gap-setting optimizations were undertaken according to a procedure described elsewhere [31]. When GG or SCLG were tested, an appropriate amount of the samples was spread onto the plate geometry to obtain a sample of the appropriate height. To avoid gel shrinking due to a possible solvent evaporation, the equipment was kept inside a glass bell with a constant moisture level. Rheological properties were studied by means of oscillatory tests. In particular, the hydrogel linear viscoelastic regions were assessed, at 1 Hz, by stress sweep experiments. Frequency sweep tests were carried out in the frequency (*f*) range 0.01–100 Hz at constant deformations $\gamma = 0.01$ (well inside the linear viscoelastic range for all the studied hydrogels). Each test was carried out in duplicate.

The generalized Maxwell model [30] was used for the theoretical dependence of the elastic (G') and viscous (G'') moduli on pulsation $\omega = 2\pi f$ (f = solicitation frequency) (Equations (1) and (2)):

$$G' = \sum_{i=1}^{n} G_i \frac{(\lambda_i \omega)^2}{1 + (\lambda_i \omega)^2}, \quad G_i = \frac{\eta_i}{\lambda_i} \tag{1}$$

$$G'' = \sum_{i=1}^{n} G_i \frac{\omega \lambda_i}{1 + (\lambda_i \omega)^2} \tag{2}$$

where n is the number of Maxwell elements considered while G_i, η_i and λ_i represent, respectively, the spring constant, the dashpot viscosity and the relaxation time of the i^th^ Maxwell element. The simultaneous fitting of Equation (1) and (2) to experimental G' and G'' data was performed assuming that relaxation times (λ_i) were scaled by a factor 10 [32]. Hence, the parameters of the model are $1 + n$ (i.e. λ_1 plus G_i). Based on a statistical procedure [33], n was selected in order to minimize the product $\chi^2(1 + n)$, where χ^2 is the sum of the squared errors. G' and G'' data represent the average of three experiments.

Flory's theory (see Equation (3)) [34] enables the determination of polymeric network crosslink density ρ_x (defined as the moles of junctions between different polymeric chains per hydrogel unit volume):

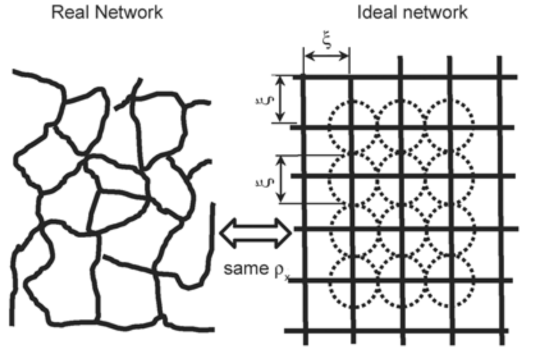

Figure 1. The equivalent network theory [36] suggests replacing the real network topology by and idealized one made up by a collection of spheres (see dotted lines) whose diameter coincides with the average real network mesh size ξ. The ideal network and the real one share the same crosslink density ρ_x.

$$\rho_x = \frac{G}{RT} \tag{3}$$

where R is the universal gas constant, T is the temperature and G (shear modulus) can be computed as the sum of the elastic contributions (G_i) pertaining to each element of the generalized Maxwell model describing the hydrogel mechanical spectrum [35]. Finally, the equivalent network theory (see Equation (4)) [36] allows evaluating the average network mesh size ξ (see Figure 1):

$$\xi = \sqrt[3]{\frac{6}{\pi \rho_x N_A}} \tag{4}$$

where N_A is the Avogadro number.

2.5. Low field NMR characterization

Low Field NMR (LF NMR) characterization was performed, at 25 and 37°C, by means of a Bruker Minispec mq20 (0.47 T, 20 MHz). Transverse relaxation time (T_2) measurements were carried out according to the (Carr-Purcell-Meiboom-Gill; CPMG) sequence (number of scans = 4; delay = 5 s). In the case of distilled water, due to the high mobility of water molecules, the determination of the transverse relaxation time (T_{2H_2O}), at both temperatures, was determined considering three different 90–180° pulse separation times (τ): 0.25, 0.5 and 1 ms. For each τ, the time (t) decay of the signal intensity (I), related to the extinction of the x–y component of the magnetization vector (M_{xy}), was fitted by the exponential function $I(t) = A_{H_2O} e^{-t/T_{2H_2O}}$. Thus, the water relaxation time was determined by a linear extrapolation to zero of the function $T_{2H_2O}(\tau)$ ($F_{25°C}$ (1, 2, 0.95) < 642; $F_{37°C}$ (1, 2, 0.95) < 197) as suggested by the Bruker company. Accordingly, we obtained $T_{2H_2O}^{25°C} = 3007 \pm 20$ ms and $T_{2H_2O}^{37°C} = 3694 \pm 60$ ms. In the case of hydrogels, due to the reduced water molecules mobility, there was no need to use three different τ values and the transverse relaxation time measurements were performed setting $\tau = 0.5$ ms. In order to determine the T_2 discrete distribution, $I(t)$ was fitted by the following sum of exponential functions (Equation (5)):

$$I(t) = \sum_{i=1}^{m} A_i e^{-t/T_{2i}} \quad \left\langle \frac{1}{T_2} \right\rangle = \frac{\sum_{i=1}^{m} \frac{A_i}{T_{2i}}}{\sum_{i=1}^{m} A_i} \tag{5}$$

where A_i are the pre-exponential factors (dimensionless) proportional to the number of protons relaxing with the relaxation time T_{2i} and $\langle 1/T_2\rangle$ is the average value of the inverse relaxation time of protons. Again, m was determined by minimizing the product $\chi^2\cdot(2m)$, where χ^2 is the sum of the squared errors and $2m$ represents the number of fitting parameters of Equation (5) [33]. The continuous relaxation time distribution was determined according to a procedure shown in a previous work [37] (Equation (6)):

$$I(t) = \int_{T_{2\min}}^{T_{2\max}} \left(f(T_2)\exp\left(-\frac{t}{T_2}\right)\right) \mathrm{d}T_2$$

$$f(T_2)=\sum_{i=1}^{m} \frac{B_i\delta_i}{\varepsilon_i}\left(\frac{T_2-T_{2\min}}{\varepsilon_i}\right)^{\delta_i-1}\exp\left(-\left(\frac{T_2-T_{2\min}}{\varepsilon_i}\right)^{\delta_i}\right) \qquad (6)$$

$$\varepsilon_i = (T_2 - T_{2\min})\left(\frac{\delta_i}{\delta_i - 1}\right)^{1/\delta_i} \qquad (7)$$

where $T_{2\max}$ (= T_{2H_2O}) and $T_{2\min}$ (= 0 ms) indicate, respectively, the lower and upper values of the continuous T_2 distribution. B_i, δ_i and ε_i are the $f(T_2)$ (sum of Weibull equations) parameters. Equation (7) simply ensures that the maximum of each Weibull distribution occurs exactly in T_{2i}. Equation (6) was numerically evaluated and fitted to experimental $I(t)$ data subdividing the relaxation spectrum wideness ($T_{2\max} - T_{2\min}$) into 200 parts (higher subdivision was not necessary).

In order to study water mobility inside the hydrogel network, Pulsed Gradient Spin Echo (PGSE) measurements were performed. The applied sequence consists in the classical echo sequence with two equal gradient pulses (of length $\delta = 0.5$ ms) occurring at $x_1 = 0.1$ ms and $x_2 = 0.1$ ms after the 90 and 180° pulses, respectively. The time separation, indicated by Δ ($\approx \tau - x_1 - \delta + x_2$), is related to the diffusion time, t_d, according to $t_d = (\Delta - \delta/3)$. After an appropriate calibration procedure, based on the knowledge of the free water self-diffusion coefficient (D_{H_2O}), it is possible measuring the average water self-diffusion coefficient inside the hydrogel (D). The details of this calibration procedure can be found in the Bruker Manual, mq Gradient Unit Users Guide, version 1, January 2000, and it essentially replicates the standard procedures for the D determination used in high field NMR [38]. In the case of T_2 measurements, data are the average of 27 experiments (9 repetitions for three different samples), while in the case of PGSE measurements, data are the average of 15 experiments (5 repetitions for three different samples).

The combination of the information coming from the relaxation and PGSE experiments were used for the estimation of the mesh size distribution of our polymeric gels. Indeed, owing to the interactions between water molecules and polymeric chains, water protons near the surface of the polymeric chains relax faster than those in the bulk [39, 40]. On the basis of this evidence and the Scherer theory [41], we very recently demonstrated [42] that, for diluted gel systems (polymer volume fraction $\varphi \leq 0.1$), the average polymeric network mesh size (ξ) can be expressed by Equation (8):

$$\xi = \sqrt{3\pi\frac{1-\varphi}{\varphi}}\,R_f \qquad (8)$$

where R_f is the radius of the polymeric chain (see Figure 2). In addition, the '*Fiber-Cell*' theory [39] ensures that the following relation holds (Equation (9)):

$$\left\langle\frac{1}{T_2}\right\rangle = \frac{1}{T_{2H_2O}} + \frac{2}{\alpha}\frac{\langle\mathcal{M}\rangle}{\xi}, \quad \alpha = \sqrt{\frac{1-\varphi}{\varphi 3\pi}} \qquad (9)$$

where $\langle 1/T_2\rangle$ is the inverse of the average relaxation time of the protons of the water molecules trapped within the polymeric network of the gel, T_{2H_2O} is the relaxation time of the protons of the bulk water (i.e. protons of the free water, whose relaxation is not

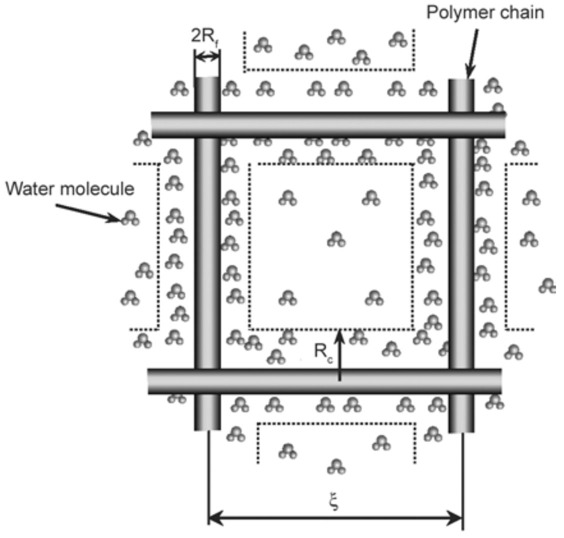

Figure 2. According to Scherer [41], the polymeric network can be represented by an ensemble of cylinders of radius R_f (fibers, i.e. polymeric chains) intersecting in a regular, cubic, array. R_c indicates the radial position where the effect of the polymeric chains on water protons relaxation becomes negligible (see dotted lines). ξ is the mesh size.

affected by the presence of the polymeric chains) and $\langle\mathcal{M}\rangle$ (length/time) is an empirical parameter, called relaxivity, accounting for the effect of polymer chains surface on proton relaxations. While Equation (9) holds on average for all the polymeric network meshes, similar expressions can be written for polymeric network meshes of different dimensions (ξ_i) (Equation (10)):

$$\frac{1}{T_{2i}} = \frac{1}{T_{2H_2O}} + \frac{2}{\alpha}\frac{\langle\mathcal{M}\rangle}{\xi_i} \tag{10}$$

where T_{2i} is the relaxation time of the water molecules protons trapped in polymeric meshes of size ξ_i. Equations (9) and (10) hold in fast-diffusion regime, i.e when the mobility of the water molecules, expressed by their self-diffusion coefficient D, is high compared to the rate of magnetization loss, identifiable with $\langle\mathcal{M}\rangle R_c$($\langle\mathcal{M}\rangle R_c/D << 1$). R_c indicates the distance from the polymer chain axis where the effect of polymeric chains on water protons relaxation becomes negligible (see Figure 2). It can be expressed [39] by Equation (11):

$$R_c = \frac{R_f}{\sqrt{\varphi}} \tag{11}$$

As $\langle 1/T_2\rangle$ (see Equation (5)), T_{2H_2O} and ξ (see Equation (8)) are known, Equation (9) allows the determination of $\langle\mathcal{M}\rangle$. Furthermore, by knowing $\langle\mathcal{M}\rangle$ and T_{2i} (see Equation (5)), Equation (10) makes possible the evaluation of ξ_i for each class of polymeric network meshes. In addition, once $\langle\mathcal{M}\rangle$ and the continuous T_2 distribution $f(T_2)$ (see Equation (6)) are known, it is possible determining the continuous ξ distribution $f(\xi)$. Indeed, the combination of Equation (8) and (10) allows to find the relation between $d\xi$ and dT_2 (Equation (12)):

$$\xi = \frac{\frac{2\langle\mathcal{M}\rangle}{\alpha}}{\frac{1}{T_2} - \frac{1}{T_{2H_2O}}}, \quad d\xi = \frac{2\langle\mathcal{M}\rangle}{\alpha}\left(\frac{T_{2H_2O}}{T_{2H_2O} - T_2}\right)^2 dT_2 \tag{12}$$

Consequently, $f(\xi)$ is given by Equation (13):

$$f(\xi) = \frac{dT_2}{d\xi}f(T_2) = \frac{\sqrt{\frac{1-\varphi}{\varphi 3\pi}}}{2\langle\mathcal{M}\rangle}\left(\frac{T_{2H_2O} - T_2}{T_{2H_2O}}\right)^2 f(T_2) \tag{13}$$

Furthermore, for a better comparison among different gels, it is convenient defining the probability $P(\xi)$ of finding a mesh of size ξ inside the polymeric network, given by Equation (14):

$$P(\xi) = \frac{f(\xi)d\xi}{\int_{\xi_{min}}^{\xi_{max}} f(\xi)d\xi} \tag{14}$$

2.6. Release experiments

The hydrogels, freshly prepared in a beaker (thus in their swollen form), assumed the cylindrical shape of the vessel (height = 1.0 cm, diameter = 2.2 cm) and they were tested for the release of the two model drugs TPH and Vit B_{12}, at 37°C. The gels were immersed in 200 mL (V_r) of distilled water (pH = 5.4), and they were kept at a certain height from the bottom of the container by a thin web (see Figure 3). The medium was gently magnetically stirred and 3 mL samples were withdrawn from the solution at appropriate time intervals and replaced with the same amount of fresh solvent (thus, experimental concentration data were corrected for dilution). The amount of the released model drug was spectrophotometrically detected (TPH at 272 nm, Vit. B_{12} at 361 nm), by means of a Perkin-Elmer (lambda 3a, UV–Vis) spectrometer using quartz cells with pathlengths of 1.0 or 0.1 cm. All experiments were car-

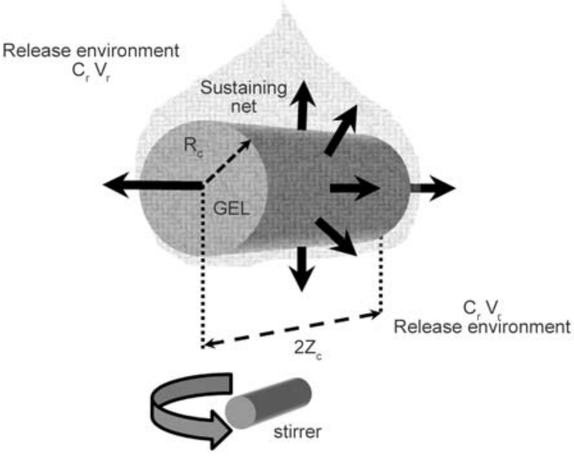

Figure 3. Drug release occurs from a cylindrical gel kept suspended in the release environment by a thin sustaining web. The release process (indicated by black thick arrows) implies the decrease of drug concentration in the gel and the contemporaneous increase of drug concentration (C_r) in the release environment (volume V_r). Release environment homogeneity is ensured by a magnetic stirrer.

ried out in triplicate. The possible erosion of the gel, in terms of polymer dissolution in the medium during the release experiments, was quantitatively determined by a colorimetric method [43] using phenol in the presence of sulphuric acid. Obtained results indicate that such erosion, in the first 8 h, is almost negligible (≤ 4%).

In order to evaluate model drug diffusion coefficients inside the gel network, release data were fitted by a mathematical model presented elsewhere [44]. Briefly, this model relays on Fick's law and on the observation that in the first 8 hours our gel did not undergo significant erosion or further swelling in the release environment. Due to gel symmetry, the intrinsically three dimensional diffusive problem could be reduced to a simpler two dimensional one (Equation (15)):

$$\frac{\partial C}{\partial t} = \frac{D_\mathrm{d}}{R_\mathrm{a}}\frac{\partial}{\partial R_\mathrm{a}}\left(R\frac{\partial C}{\partial R_\mathrm{a}}\right) + D_\mathrm{d}\frac{\partial^2 C}{\partial Z^2} \tag{15}$$

where D_d is the drug diffusion coefficient in the gel, t is time, C is the drug concentration (mass/volume) in the cylinder, R_a and Z are the radial and axial axes, respectively. This equation must satisfy the following initial and boundary conditions (Equations (16)–(19)):

Initial conditions:

$$C(Z,R_\mathrm{a}) = C_0, \quad -Z_\mathrm{c} \le Z \le Z_\mathrm{c}, \quad 0 \le R_\mathrm{a} \le R_\mathrm{c} \tag{16}$$

$$C_\mathrm{r} = 0 \tag{17}$$

Boundary conditions:

$$C(Z,R_\mathrm{c},t) = C(\pm Z_\mathrm{c}, R_\mathrm{a}, t) = k_\mathrm{p}\cdot C_\mathrm{r}(t) \tag{18}$$

$$V_\mathrm{r}C_\mathrm{r}(t) = \pi R_\mathrm{c}^2 2Z_\mathrm{c}C_0 - \int_0^{Z_\mathrm{c}}\int_0^{R_\mathrm{c}} C(Z,R_\mathrm{a},t)2\pi R_\mathrm{a}\mathrm{d}R_\mathrm{a}\mathrm{d}Z \tag{19}$$

where $2Z_\mathrm{c}$ and R_c are, respectively, cylinder height and radius (see Figure 3), C_0 is the initial and uniform drug concentration in the cylinder, C_r and V_r are the drug concentration and the volume of the release medium while k_p is the drug partition coefficient between the cylindrical gel and the environmental release fluid. Equation (19) is a drug mass balance for the gel/release fluid system allowing to state the relation between C_r and $C(Z,R_\mathrm{a},t)$. In order to account for the diffusion resistance exerted by the thin web surrounding the cylindrical gel (it slightly reduces release surface and favours the formation of a thick aqueous boundary layer at the gel/release environment interface), an interfacial diffusion coefficient (D_di), lower than the bulk one (D_d), is introduced. Thus, inside the gel, drug transport is ruled by Equation (15) while, at the interface, drug transport is governed by Equation (15) where D is replaced by D_di. As, in our case, polymer concentration is low and model drug solubility in the release environment fluid is high, k_p can be set equal to 1 [45]. Accordingly, the proposed model is characterized by two fitting (unknowns) parameters (D_d and D_di). Model numerical solution was performed according to the control volume method [46] subdividing the cylindrical gel into 100 control volumes in the radial and axial directions (for a total of 10^4 control volumes) and considering an integration time step equal to 22.5 s.

Once D_d is known from Equation (15) fitting to experimental release data, the Peppas equation allows to estimate the polymeric network average mesh size ξ [47] (Equation (20)):

$$\frac{D_\mathrm{d}}{D_\mathrm{d0}} = \left(1 - \frac{2r_\mathrm{s}}{\xi}\right)\exp\left(-\frac{\varphi}{1-\varphi}\right) \tag{20}$$

where r_s and D_d0 indicate, respectively, the radius of the diffusing drug and its diffusion coefficient in the pure solvent filling the polymeric network.

3. Results and discussion

Stress sweep tests, carried out at 25 and 37°C, indicated that for all studied systems (GG, GGb, SCLG and SCLGb), the critical deformation γ_c is always much higher than the constant one ($\gamma = 0.01$) applied in frequency sweep tests. Figures 4 and 5 show the mechanical spectra referring to the four systems, studied at 25 and 37°C, respectively.

It can be noticed (see Figure 4a) that, at 25°C, SCLG exhibits a gel behavior as the elastic modulus (G') is always bigger than the viscous one (G'') and both are, almost, pulsation (ω) independent. On the other side, GG shows the typical solution behavior as G'' prevails on G' and both moduli depend on ω. Five and four Maxwell elements are, respectively, necessary for a statistically good description (see F test values in Figure 4a caption) of the GG and SCLG mechanical spectra (see fitting parameters values in Table 1). Figure 4b clearly shows the different effect of borax addition to the GG and SCLG systems. In fact, while borax presence plays a marginal role in

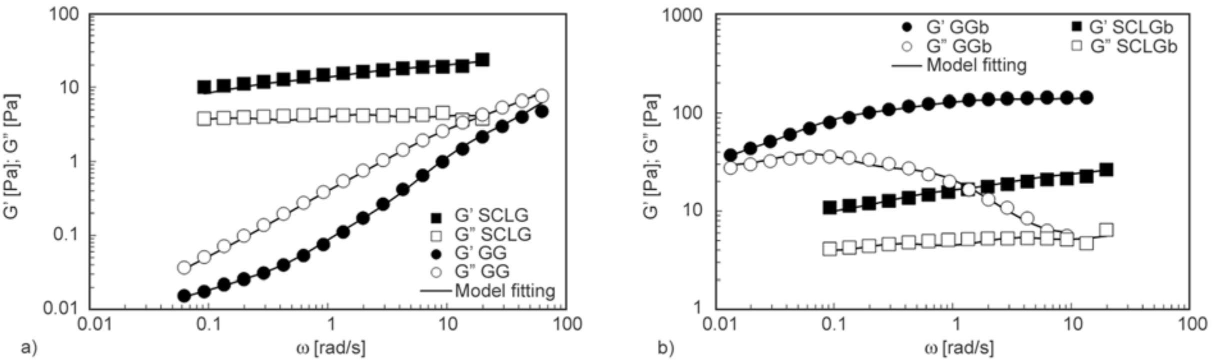

Figure 4. a) mechanical spectra (*G′* elastic modulus, *G″* viscous modulus) referring to the Guar gum (GG) and Scleroglucan (SCLG) systems at 25°C. Solid lines indicate the best fitting of the generalized Maxwell Model (Equations (1), (2)) (*F* test always positive: $F_{GG}(5,32,0.95) < 150$, $F_{SCLG}(4,25,0.95) < 374$). b) mechanical spectra (*G′* elastic modulus, *G″* viscous modulus) referring to the Guar gum/borax (GGb) and Scleroglucan/borax (SCLGb) systems at 25°C. Solid lines indicate the best fitting of the generalized Maxwell Model (Equations (1), (2)) (*F* test always positive: $F_{GGb}(4,32,0.95) < 103.5$, $F_{SCLGb}(5,24,0.95) < 251$).

Table 1. Generalized Maxwell model (Equations (1), (2)) parameters (± standard deviation) deriving from the fitting of data shown in Figures 1 and 2. λ_1 is the first relaxation time, G_i represents the spring constant of the ith Maxwell element, G is the shear modulus (sum of all G_i), ρ_x is the crosslink density calculated according to Equation (3), while ξ is the average network mesh size calculated according to Equation (4).

25°C	**GG**	**SCLG**	**GGb**	**SCLGb**
λ_1 [s]	$(7.7\pm3)\cdot10^{-3}$	$(81.7\pm11)\cdot10^{-3}$	$(15.7\pm4)\cdot10^{-3}$	$(30.0\pm5)\cdot10^{-3}$
G_1 [Pa]	20.3 ±4.4	7.0±0.4	21.8±6.1	9.7±0.84
G_2 [Pa]	2.3±1.1	6.2±0.36	0	7.4±0.5
G_3 [Pa]	0.12±0.07	5.0±0.37	36.5±8.4	6.4±0.5
G_4 [Pa]	0.014±0.007	7.4±0.53	61.6±9.8	6.1±0.76
G_5 [Pa]	0.012±0.004	–	42.0±13	4.0±0.9
G [Pa]	22.9±4.5	25.6±0.8	162±19	33.6±1.6
ρ_x [mol/cm^3]	–	$(1.0\pm0.03)\cdot10^{-8}$	$(6.5\pm0.79)\cdot10^{-8}$	$(1.4\pm0.06)\cdot10^{-8}$
ξ [nm]	–	67.4±0.8	36.5±1.4	61.6±1.0
37°C	**GG**	**SCLG**	**GGb**	**SCLGb**
λ_1 [s]	$(11.6\pm2)\cdot10^{-3}$	$(62.5\pm6.6)\cdot10^{-3}$	$(22.7\pm6.4)\cdot10^{-3}$	$(18.9\pm2)\cdot10^{-3}$
G_1 [Pa]	7.6±1.1	5.4±0.23	7.9±2.5	8.3±0.32
G_2 [Pa]	0.40±0.22	4.1±0.16	10.0±3.8	5.5±0.27
G_3 [Pa]	0.049±0.045	2.9±0.15	36.1±3.8	4.0±0.2
G_4 [Pa]	0.04±0.038	0	9.8±2.9	3.5±0.24
G_5 [Pa]	0.069±0.043	1.8±0.5	1.6±0.6	1.5±0.3
G [Pa]	8.2±1.1	14.2±0.75	65.5±6.6	22.9±0.6
ρ_x [mol/cm^3]	–	$(5.5\pm0.3)\cdot10^{-9}$	$(2.5\pm0.25)\cdot10^{-8}$	$(8.9\pm0.2)\cdot10^{-9}$
ξ [nm]	–	83.2±1.5	49.9±1.7	71.0±0.6

the case of SCLG (only a very small increase of the moduli can be noticed), for the GG system a relevant change occurs in the mechanical properties. Now, *G′* prevails over *G″* in the whole experimental frequency window and the crossing point is around $\omega = 0.01$ rad/s. The ω dependence of *G′* and *G″* witnesses the weak nature of the formed hydrogel. Also in this case, the generalized Maxwell model provides a statistically good fitting (see *F* test values in Figure 4b caption) adopting, respectively, four and five elements for the GGb and SCLGb systems.

Temperature increase to 37°C does not modify the gel and the solution nature of the SCLG and GG systems. Nevertheless *G′* and *G″*, for both systems, are reduced (see Figure 5a). Again, borax addition (Figure 5b) implies a moderate increase of the SCLGb moduli and a considerable modification of the GG characteristics. Indeed, not only *G′* and *G″* are clearly increased (about one order of magnitude) but also

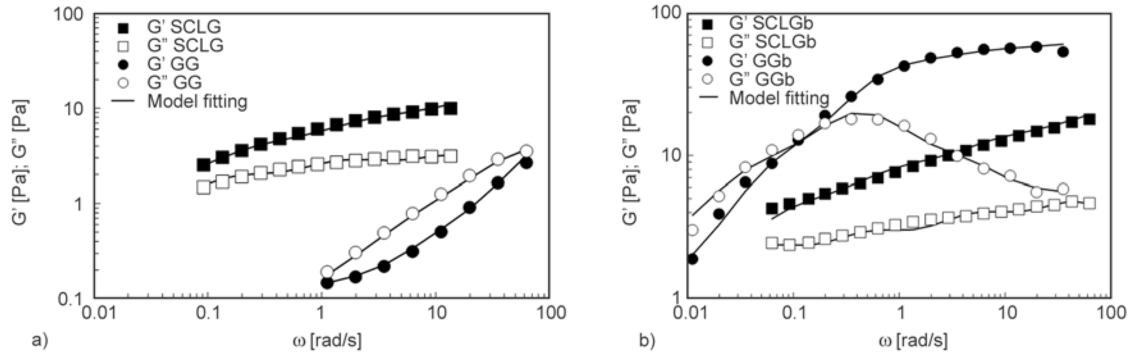

Figure 5. a) mechanical spectra (G' elastic modulus, G'' viscous modulus) referring to the Guar gum (GG) and Scleroglucan (SCLG) systems at 37°C. Solid lines indicate the best fitting of the generalized Maxwell Model (Equations (1), (2)) (F test always positive: $F_{GG}(5,10,0.95) < 38.1$, $F_{SCLG}(5,22,0.95) < 504.5$). b) mechanical spectra (G' elastic modulus, G'' viscous modulus) referring to the Guar gum/borax (GGb) and Scleroglucan/borax (SCLGb) systems at 37°C. Solid lines indicate the best fitting of the generalized Maxwell Model (Equations (1), (2)) (F test always positive: $F_{GGb}(5,24,0.95) < 55.4$, $F_{SCLGb}(5,32,0.95) < 2076$).

the system behavior shifts from that of a solution (GG) to that of an incipient weak gel (GGb) as testified by the presence of the crossover point (detectable at $\omega \approx 0.2$ rad/s) where system elastic and viscous characteristics are equal. This means that the system is moving from a sol to a gel condition, i.e, it lies in a sort of transition zone. Generalized Maxwell model gives a statistically good fitting of data shown in Figure 5a and 5b (see F test values in the captions to this figures) assuming four or five Maxwell elements (see Table 1). In conclusion, rheological characterization evidences the marked effect of borax addition to the GG system and the weak effect exerted on the SCLG system at both temperatures. While SCLG always exhibits gel properties, GG system becomes a weak gel (or incipient weak gel) only in the presence of borax.

On the basis of the crosslink density (ρ_x) evaluation (see Equation (3)), equivalent network theory (see Equation (4)) allows to estimate, for the gel systems, the average network mesh size ξ. Table 1 shows that ξ spans from 36.5 nm (GGb, 25°C) to 83.2 nm (SCLG, 37°C). The high ξ values witness the low connectivity of all tested gels.

LF NMR analysis indicates that, regardless of temperature, GG is characterized by only one relaxation time (T_{21}) (see Table 2), as expected for aqueous solutions, while the relaxation of the protons belonging to the polymeric chains are not detectable, due to their very low amount (around 0.5%) in comparison with those of water. Thus, LF NMR and rheology analysis lead to the same conclusion: the GG system is an aqueous polymer solution at both temperatures.

Table 2. Relaxation times, T_{22} and T_{21} ± standard deviation, and weight [%], A_1% and A_2% ± standard deviation, referring to GG, SCLG, GGb, SCLGb and distilled water, at 25 and 37°C. $A_i\% = 100 \cdot A_i/(A_1 + A_2)$

T [°C]		T_{21} [ms]	A_1%	T_{22} [ms]	A_2%
25	GG	2032±92	100		
	GGb	1527±46	100		
	SCLG	1359±23	100		
	SCLGb	343±84	84.5±23.5	173±77	15.5±7.8
	water	3007±20	100		
37	GG	2466±80	100		
	GGb	1912±94	100		
	SCLG	1321±46	100		
	SCLGb	451±74	100	–	–
	water	3694±60	100		

The addition of borax to the GG system induces a significant reduction of T_{21} at both temperatures. Since the addition of borax to distilled water does not substantially modify the water relaxation time T_{2H_2O} (data not shown), we can assert that the observed reduction of T_{21}, at both temperatures, cannot directly depend on the presence of borax. Thus, the T_{21} reduction is in agreement with the formation of a new, more compact, architecture of the polymeric chains (gel network) related to the addition of borax. It is interesting to point out that, in the case of a dextran system ($c_p = 0.7\%$ w/v)), the addition of borax (r = borax moles/dextran moles = 1; data not shown) does not modify T_{21}, this being a clear indication that, in this case, the presence of borax does not lead to the formation of a polymeric network. It is also interesting to notice that the relative increase of T_{21} with temperature is similar for both, GGb

(25%) and GG (21%) systems (see Table 2). This result shows that the interactions among polymeric chains and water molecules are not so strong, as expected for a weak gel.

Although the SCLG system shows, as GG, only one relaxation time at 25 and 37°C, it cannot be considered a solution, because T_{21} is, essentially, temperature independent and this behavior should not occur in a polymeric solution at such low concentration (c_p = 0.7% v/w). In addition, also the relatively small T_{21} value (recorded at both temperatures) with respect to that of water, T_{2H_2O}, is not compatible with such a low c_p. Finally, Table 2 shows that the addition of borax to the SCLG system implies a drastic reduction of the average relaxation time $\langle T_2 \rangle$ at 25°C (317 ms) and 37°C (451 ms). Again, the essential $\langle T_2 \rangle$ independence on temperature and its high reduction in comparison with water, $\langle T_{2H_2O} \rangle$, indicates the gel nature of the SCLGb system. The fact that, for this last system, two relaxation times were detected at 25°C and only one at 37°C can be explained by the formation, at 37°C, of a more homogeneous polymeric network due to a higher mobility of borax ions in the initial polymer solution. In conclusion, as far as the macroscopic behavior is concerned, the relaxation analysis shows the same findings obtained from the rheological characterization of our polymeric systems. On the other side, some differences arose in the estimation of ξ. Indeed, knowing that $\varphi = 4.35\cdot10^{-3}$ and $R_f \approx 2.15$ nm for both GG and SCLG systems [48], the application of Equation (8) leads to ξ = 99.8 nm. The comparison between the values reported in Table 1 (25 and 37°C) and Table 3 shows that the ξ values from rheological approach are about 40% for GGb and about 75% for SCLG and SCLGb of those obtained by LF NMR theory. Nevertheless, taking into account the simplifications adopted in both approaches, we believe that these cannot be considered as significant differences.

In order to estimate the continuous mesh size distribution of GGb, SCLG and SCLGb systems, Equation (9) was used for the determination of parameter $\langle \mathcal{M} \rangle$ whose values are reported in Table 3. It can be seen that $\langle \mathcal{M} \rangle$ values, regardless of temperature, increase going from GGb to SCLG and SCLGb systems. This indicates a stronger and stronger effect of polymer chain surfaces on the relaxation of protons. The diffusion coefficient, D, was practically constant with the diffusion time t_d for all studied systems (see, Figure 6), and therefore the check on the fast diffusion conditions (evaluation of the dimensionless parameter $\langle \mathcal{M} \rangle R_c/D$) was carried out taking into account the D value averaged on the measurements performed at all t_d.

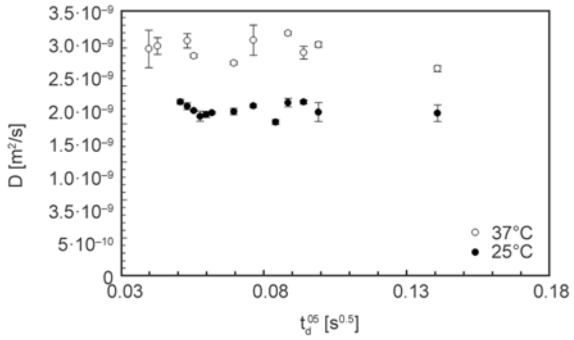

Figure 6. Experimental dependence of the water self-diffusion coefficient (D) on the square root of the diffusion time t_d for the Guar gum/borax gel (GGb) at 25 and 37°C. For t_d = 0, water self-diffusion coefficient at 25 and 37°C is, respectively, $2.3\cdot10^{-9}$ and $3.04\cdot10^{-9}$ m²/s [50]. Vertical bars indicate standard error.

Table 3. Average relaxation time $\langle T_2 \rangle$ ± standard deviation, water self-diffusion coefficient D ± standard deviation, average effect of surface on protons relaxation $\langle \mathcal{M} \rangle$ ± standard deviation, R_c = 32.6 nm (see Equation (11)) and mesh diameter ξ, referring to SCLG, GGb and SCLGb systems at 25 and 37°C. Proton relaxation times (T_{2H_2O}) at 25°C is 3007±20 ms while at 37°C it is 3694±60 ms.

T [°C]		$\langle T_2 \rangle$ [ms]	ξ [nm]	$D\cdot10^9$ [m²/s]	$\langle \mathcal{M} \rangle\cdot10^3$ [nm/ms]	$\frac{\langle \mathcal{M} \rangle R_c}{D}\cdot10^6$
25°C	GGb	1527±46	99.8	2.2±0.1	62±6	1.2
	SCLG	1359±23	99.8	2.2±0.1	99±3	1.5
	SCLGb	317±23	109±16 (84.5%) 31±9 (15.5%)	2.3±0.1	693±263	10.0
37°C	GGb	1912±94	99.8	2.9±0.2	79±5	0.7
	SCLG	1321±46	99.8	2.8±0.2	119±6	1.4
	SCLGb	451±74	99.8	2.9±0.2	477±89	5.4

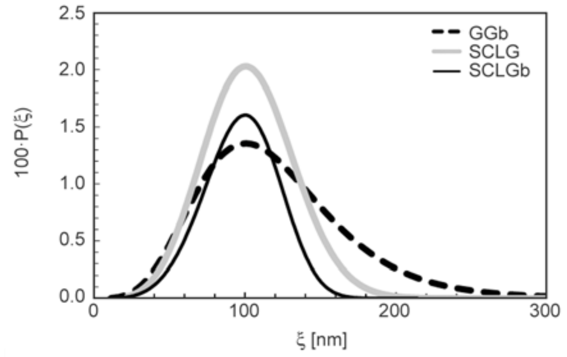

Figure 7. Mesh size distribution, $P(\xi)$, of GGb (Guar gum/borax), SCLG (Scleroglucan) and SCLGb (Scleroglucan/borax) hydrogels at 37°C

Table 3 clearly shows that in all gel systems, $\langle \mathcal{M} \rangle R_c/D$ was much less than 1, i.e. fast diffusion conditions always apply. Accordingly, Equation (10) and (13) can be used for the estimation of $f(T_2)$, $f(\xi)$ and, finally of $P(\xi)$, as shown in Figure 7 (37°C).

Figure 7 shows that, for GGb, the mesh size distribution spans, approximately, from 10 to 300 nm while it is slightly less wide for SCLG and SCLGb. As the ξ values estimated by means of rheology experiments fall inside these distributions and they are not too far from the distribution peaks, we may conclude that the two approaches do not lead to very different results (see Table 1).

Another approach to acquire some insight about polymeric network characteristics is the determination of model molecule diffusion coefficients. For this purpose, two model drugs, TPH and Vit B_{12}, were considered. Figure 8 reports TPH and Vit B_{12} release from GGb at 37°C. These two release kinetics are fitted by means of Equation (15) knowing that the release volume $V_r = 200$ cm^3 and the initial drug concentration C_0 in the gel is equal to 5.2 mg/cm^3 for the two drugs. In both cases, the fitting is statistically good as proved by the F test (F_{TPH} (1, 10, 0.95) < 75; $F_{Vit\,B_{12}}$ (1, 10, 0.95) < 30627). In the case of TPH we have $D_d = D_{di} = (2.7\pm0.5)\cdot10^{-10}$ m^2/s while, for Vit B_{12}, model fitting yields to $D_d = (2.3\pm0.1)\cdot10^{-10}$ m^2/s and $D_{di} = (3.0\pm0.1)\cdot10^{-11}$ m^2/s. These results indicate that the resistance due to the thin web, suspending the gel in the release environment, is negligible for TPH while it plays a significant role in the case of Vit B_{12}. This seems reasonable if we consider the different model drug dimensions (TPH van der Waals radius $r = 3.7$ Å; Vit B_{12} van der Waals radius $r = 8.5$ Å) [45]. On the basis of the diffusion coefficients in water at 37°C of TPH ($D_{d0} = 8.2\cdot10^{-10}$ m^2/s) and of Vit B_{12} ($D_{d0} = 3.8\cdot10^{-10}$ m^2/s) [45], Equation (20) allows estimating the polymeric network mesh size (ξ) knowing that polymer volume fraction (φ) in GGb hydrogel is equal to $4.35\cdot10^{-3}$, it turns out that $\xi = (1.1\pm0.1)$ and (4.3±0.06) nm in the case of TPH and Vit B_{12}, respectively. These values are much smaller than those estimated by means of rheology and LF NMR (49.9 nm, see Table 1, and 99.8 nm, see Table 3). Due to the low polymer concentration and crosslink density of GGb hydrogel, the ξ values estimated according to Equation (20) seem too small. The motivation for the Equation (20) failure should rely on the fact that GGb system, at 37°C, represents an incipient hydrogel condition (as previously discussed, see also Figure 5b). Here, drug diffusion is not only affected by the presence of the structured polymeric network but also by the chains that, although bound to the network to one end, can freely fluctuate among meshes. These chains are elastically inactive but can hinder drug diffusion through a viscous drag, favoured by weak van der Walls interactions with drug molecules. Tomic and coworkers [49] found that also very weak van der Waals interactions are sufficient to hinder drug molecule movements in the presence of a polymeric network with mesh size much larger than the drug molecular size. In addition, the rheological analysis suggests that the number of elastically inactive chains is high, as proved by the importance of the viscous contribution to the GGb mechanical behavior (see Figure 5b). On the contrary, in the case of a true hydrogel, such as SCLGb (where the viscous contribution is low), we found a good agreement

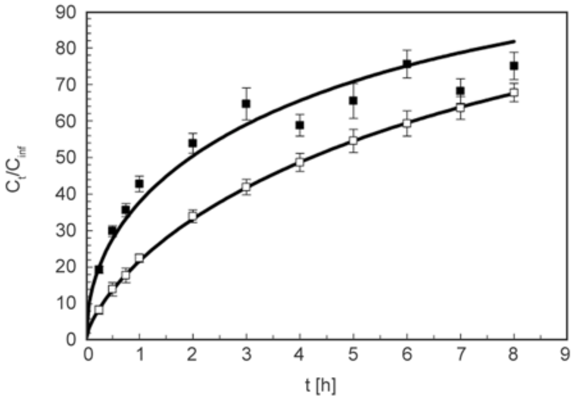

Figure 8. Theophylline (TPH; filled squares) and Vit B_{12} release (open squares) from GGb hydrogel at 37°C (vertical bars indicate standard error). C_t and C_{inf} are, respectively, drug concentration at time t and after an infinite time. Solid lines indicate model best fitting (Equation (15)).

between the estimation of ξ according to the rheological approach and Equation (20) [44].

4. Conclusions

The rheological and LF NMR analyses allow concluding that, regardless of temperature, the GG system (c_p = 0.7%) behaves as a polymeric solution while SCLG (c_p = 0.7%) is a gel. The addition of borax to GG (c_p = 0.7%) appreciably modifies the system behavior leading to the formation of a weak hydrogel that, at 37°C, can be considered as an incipient weak gel. The evaluation of the polymeric network mesh size by rheology resulted to be slightly smaller than that derived from the LF NMR approach (mesh size distribution spanning from 10 to 300 nm). On the other side, the addition of borax to SCLG mainly appears at the nanoscale level. In fact, while gel strength is slightly increased, borax leads to a considerable reduction of the proton average relaxation times. The high values of the average polymeric network mesh size of all the studied gels (GGb, SCLG, SCLGb) indicate their low connectivity. In all tested gels (GGb, SCLG and SCLGb), the fast condition diffusion was verified. In the case of GGb hydrogel, rheology and LF NMR led to an estimations of the average mesh size that does not agree with that calculated from the model drug diffusion coefficient inside the gel. As the rheology – LF NMR estimations seems to be the correct ones, the failure of the diffusion coefficient approach should rely on the nature of the GGb polymeric network. Actually, in a hydrogel where the viscous component is high, model drug movement is not only reduced by the presence of the polymeric network (elastically active chains) but also by elastic inactive chains that, although bound to the network, can freely fluctuate and can exert a viscous drag, favored by weak van der Waals interactions, on the moving model drug molecules. This hypothesis is supported by the fact that, in the case of SCLGb, where the viscous component is not so important, rheology approach and the diffusion coefficient approach lead to a similar estimation of the average mesh size.

Acknowledgements

Financial support from Sapienza University of Rome 'Ricerche Universitarie' 2011, n. C26A119N2S and 'Fondo PRIN 2010-2011 (20109PLMH2)', are acknowledged.

References

[1] Maier H., Anderson M., Karl C., Magnuson K., Whistler R. L.: Guar, locust bean gum, tara, and fenugreek gums. in 'Industrial gums: polysaccharides and their derivatives' (eds.: Whistler R. L., BeMiller J. N.) Academic Press, New York, 181–226 (1993).

[2] McCleary B. V., Clark A. H., Dea I. C. M., Rees D. A.: The fine structures of carob and guar galactomannans. Carbohydrate Research, **139**, 237–260 (1985). DOI: 10.1016/0008-6215(85)90024-2

[3] Fox J. E.: Seed gums. in 'Thickening and gelling agents for food' (ed.: Imeson A.) Blackie Academic Professional, New York, 262–283 (1997).

[4] Kucera C. H., DeMott D. N.: Drilling fluid containing crosslinked polysaccharide derivative. U.S. patent 4257903, USA (1981).

[5] Brode G. L., Goddard E. D., Harris W. C., Salensky G. A.: Cationic polysaccharides for cosmetics and therapeutics. in 'Cosmetic and pharmaceutical applications of polymers' (eds.: Gebelein C. G., Cheng T. C., Yang V. C.) Plenum Press, New York, 117–128 (1991).

[6] Vijayendran B. R., Bone T.: Absolute molecular weight and molecular weight distribution of guar by size exclusion chromatography and low-angle laser light scattering. Carbohydrate Polymers, **4**, 299–313 (1984). DOI: 10.1016/0144-8617(84)90005-5

[7] Picout D. R., Ross-Murphy S. B.: On the Mark–Houwink parameters for galactomannans. Carbohydrate Polymers, **70**, 145–148 (2007). DOI: 10.1016/j.carbpol.2007.03.010

[8] Gliko-Kabir I., Yagen B., Penasi A., Rubinstein A.: Low swelling, crosslinked guar and its potential use as colon-specific drug carrier. Pharmaceutical Research, **15**, 1019–1025 (1998). DOI: 10.1023/A:1011921925745

[9] Coviello T., Alhaique F., Dorigo A., Matricardi P., Grassi M.: Two galactomannans and scleroglucan as matrices for drug delivery: Preparation and release studies. European Journal of Pharmaceutics and Biopharmaceutics, **66**, 200–209 (2007). DOI: 10.1016/j.ejpb.2006.10.024

[10] Norisuye T., Yanaki T., Fujita H.: Triple helix of a *Schizophyllum commune* polysaccharide in aqueous solution. Journal of Polymer Science: Polymer Physics Edition, **18**, 547–558 (1980). DOI: 10.1002/pol.1980.180180314

[11] Yanaki T., Norisuye T., Fujita H.: Triple helix of *Schizophyllum commune* polysaccharide in dilute solution. 3. Hydrodynamic properties in water. Macromolecules, **13**, 1462–1466 (1980). DOI: 10.1021/ma60078a019

[12] Giavasis I., Harvey L. M., McNeil B.: Scleroglucan. in 'Biopolymers, polysaccharides II' (eds.: De Baets S., Vandamme E. J., Steinbüchel A.) Wiley, Weinheim, 37–60 (2002).

[13] Rizk S., Duru C., Gaudy D., Jacob M., Ferrari F., Bertoni M., Caramella C.: Physico-chemical characterization and tabletting properties of Scleroglucan. International Journal of Pharmaceutics, **112**, 125–131 (1994).
DOI: 10.1016/0378-5173(94)90422-7

[14] Pezron E., Leibler L., Lafuma F.: Complex formation in polymer-ion solutions. 2. Polyelectrolyte effects. Macromolecules, **22**, 2656–2662 (1989).
DOI: 10.1021/ma00196a021

[15] Shibayama M., Hiroyuki Y., Hidenobu K., Hiroshi F., Shunji N.: Sol-gel transition of poly(vinyl alcohol)-borate complex. Polymer, **29**, 2066–2071 (1988).
DOI: 10.1016/0032-3861(88)90182-6

[16] Bocchinfuso G., Palleschi A., Mazzuca C., Coviello T., Alhaique F., Marletta G.: Theoretical and experimental study on a self-assembling polysaccharide forming nanochannels: Static and dynamic effects induced by a *soft* confinement. The Journal of Physical Chemistry B, **112**, 6473–6483 (2008).
DOI: 10.1021/jp076074f

[17] Palleschi A., Coviello T., Bocchinfuso G., Alhaique F.: Investigation on a new scleroglucan/borax hydrogel: Structure and drug release. International Journal of Pharmaceutics, **322**, 13–21 (2006).
DOI: 10.1016/j.ijpharm.2006.05.029

[18] Kesavan S., Prud'homme R. K.: Rheology of guar and (hydroxypropyl) guar crosslinked by borate. Macromolecules, **25**, 2026–2032 (1992).
DOI: 10.1021/ma00033a029

[19] Tayal A., Pai V. B., Khan S. A.: Rheology and microstructural changes during enzymatic degradation of a guar–borax hydrogel. Macromolecules, **32**, 5567–5574 (1999).
DOI: 10.1021/ma990167g

[20] Pezron E., Leibler L., Ricard A., Audebert R.: Reversible gel formation induced by ion complexation. 2. Phase diagrams. Macromolecules, **21**, 1126–1131 (1988).
DOI: 10.1021/ma00182a046

[21] Pezron E., Ricard A., Lafuma F., Audebert R.: Reversible gel formation induced by ion complexation. 1. Borax-galactomannan interactions. Macromolecules, **21**, 1121–1125 (1988).
DOI: 10.1021/ma00182a045

[22] Pezron E., Leibler L., Ricard A., Lafuma F., Audebert R.: Complex formation in polymer-ion solution. 1. Polymer concentration effects. Macromolecules, **22**, 1169–1174 (1989).
DOI: 10.1021/ma00193a030

[23] Fang Y., Takahashi R., Nishinari K.: A gel network constituted by rigid schizophyllan chains and nonpermanent cross-links. Biomacromolecules, **5**, 126–136 (2004).
DOI: 10.1021/bm034261n

[24] Grisel M., Muller G.: Rheological properties of the schizophyllan–borax system. Macromolecules, **31**, 4277–4281 (1998).
DOI: 10.1021/ma970485k

[25] Bluhm L. T., Deslandes Y., Marchessault R. H., Pérez S., Rinaudo M.: Solid-state and solution conformation of scleroglucan. Carbohydrate Research, **100**, 117–130 (1982).
DOI: 10.1016/S0008-6215(00)81030-7

[26] Sandolo C., Matricardi P., Alhaique F., Coviello T.: Effect of temperature and cross-linking density on rheology of chemical cross-linked guar gum at the gel point. Food Hydrocolloids, **23**, 210–220 (2009).
DOI: 10.1016/j.foodhyd.2008.01.001

[27] Pezron E., Ricard A., Leibler L.: Rheology of galactomannan-borax gels. Journal of Polymer Science Part B: Polymer Physics, **28**, 2445–2461 (1990).
DOI: 10.1002/polb.1990.090281301

[28] Bocchinfuso G., Mazzuca C., Sandolo C., Margheritelli S., Alhaique F., Coviello T., Palleschi A.: Guar gum and Scleroglucan interactions with borax: Experimental and theoretical studies of an unexpected similarity. The Journal of Physical Chemistry B, **114**, 13059–13068 (2010).
DOI: 10.1021/jp105838t

[29] Kök M. S., Hill S. E., Mitchell J. R.: Viscosity of galactomannans during high temperature processing: Influence of degradation and solubilisation. Food Hydrocolloid, **13**, 535–542 (1999).
DOI: 10.1016/S0268-005X(99)00040-5

[30] Lapasin R., Pricl S.: Rheology of industrial polysaccharides: Theory and applications. Blackie Academic and Professional, London (1995).

[31] Kuijpers A. J., Engbers G. H. M., Feijen J., De Smedt S. C., Meyvis T. K. L., Demeester J., Krijgsveld J., Zaat S. A. J., Dankert J.: Characterization of the network structure of carbodiimide cross-linked gelatin gels. Macromolecules, **32**, 3325–3334 (1999).
DOI: 10.1021/ma981929v

[32] Grassi M., Lapasin R., Pricl S.: A study of the rheological behavior of scleroglucan weak gel systems. Carbohydrate Polymers, **29**, 169–181 (1996).
DOI: 10.1016/0144-8617(95)00120-4

[33] Draper N. R., Smith H.: Applied regression analysis. Wiley, New York (1966).

[34] Flory P. J.: Principles of polymer chemistry. Cornell University Press, Ithaca (1953).

[35] Pasut E., Toffanin R., Voinovich D., Pedersini C., Murano E., Grassi M.: Mechanical and diffusive properties of homogeneous alginate gels in form of particles and cylinders. Journal of Biomedical Materials Research Part A, **87**, 808–818 (2008).
DOI: 10.1002/jbm.a.31680

[36] Schurz J.: Rheology of polymer solutions of the network type. Progress in Polymer Science, **16**, 1–53 (1991).
DOI: 10.1016/0079-6700(91)90006-7

[37] Turco G., Donati I., Grassi M., Marchioli G., Lapasin R., Paoletti S.: Mechanical spectroscopy and relaxometry on alginate hydrogels: A comparative analysis for structural characterization and network mesh size determination. Biomacromolecules, **12**, 1272–1282 (2011). DOI: 10.1021/bm101556m

[38] Uh J., Watson A. T.: Nuclear magnetic resonance determination of surface relaxivity in permeable media. Industrial and Engineering Chemistry Research, **43**, 3026–3032 (2004). DOI: 10.1021/ie030599m

[39] Chui M. M., Phillips R. J., McCarthy M. J.: Measurement of the porous microstructure of hydrogels by nuclear magnetic resonance. Journal of Colloid and Interface Science, **174**, 336–344 (1995). DOI: 10.1006/jcis.1995.1399

[40] Brownstein K. R., Tarr C. E.: Importance of classical diffusion in NMR studies of water in biological cells. Physical Review A, **19**, 2446–2453 (1979). DOI: 10.1103/PhysRevA.19.2446

[41] Scherer G. W.: Hydraulic radius and mesh size of gels. Journal of Sol-Gel Science and Technology, **1**, 285–291 (1994). DOI: 10.1007/BF00486171

[42] Grassi M., Fiorentino S., Farra R., Dapas B., Grassi G.: Hydrogels mesh size evaluation. in: ‘Polysaccharide hydrogels: Characterization and biomedical applications’ (eds.: Matricardi P., Alhaique F., Coviello T.) Pan Stanford Publishing, Singapore, in press (2013).

[43] Dubois M., Gilles K. A., Hamilton J. K., Rebers P. A., Smith F.: Colorimetric method for determination of sugars and related substances. Analytical Chemistry, **28**, 350–356 (1956). DOI: 10.1021/ac60111a017

[44] Grassi M., Lapasin R., Coviello T., Matricardi P., Di Meo C., Alhaique F.: Scleroglucan/borax/drug hydrogels: Structure characterisation by means of rheological and diffusion experiments. Carbohydrate Polymers, **78**, 377–383 (2009). DOI: 10.1016/j.carbpol.2009.04.025

[45] Grassi M., Grassi G., Lapasin R., Colombo I.: Understanding drug release and absorption mechanisms: A physical and mathematical approach. CRC Press, Boca Raton (2007).

[46] Patankar S. V.: Numerical heat transfer and fluid flow. Hemisphere Publishing, New York (1990).

[47] Peppas N. A., Bures P., Leobandung W., Ichikawa H.: Hydrogels in pharmaceutical formulations. European Journal of Pharmaceutics and Biopharmaceutics, **50**, 27–46 (2000). DOI: 10.1016/S0939-6411(00)00090-4

[48] Palleschi A., Bocchinfuso G., Coviello T., Alhaique F.: Molecular dynamics investigations of the polysaccharide scleroglucan: First study on the triple helix structure. Carbohydrate Research, **340**, 2154–2162 (2005). DOI: 10.1016/j.carres.2005.06.026

[49] Tomić K., Veeman W. S., Boerakker M., Litvinov V. M., Dias A. A.: Lateral and rotational mobility of some drug molecules in a poly(ethylene glycol) diacrylate hydrogel and the effect of drug-cyclodextrin complexation. Journal of Pharmaceutical Sciences, **97**, 3245–3256 (2008). DOI: 10.1002/jps.21251

[50] Holz M., Heil S. R., Sacco A.: Temperature-dependent self-diffusion coefficients of water and six selected molecular liquids for calibration in accurate ^{1}H NMR PFG measurements. Physical Chemistry Chemical Physics, **2**, 4740–4742 (2000). DOI: 10.1039/B005319H

eXPRESS Polymer Letters Vol.7, No.9 (2013) 747–755
Available online at www.expresspolymlett.com
DOI: 10.3144/expresspolymlett.2013.72

The preparation of the poly(vinyl alcohol)/graphene nanocomposites with low percolation threshold and high electrical conductivity by using the large-area reduced graphene oxide sheets

T. N. Zhou, X. D. Qi, Q. Fu[*]

College of Polymer Science and Engineering, State Key Laboratory of Polymer Material Engineering, Sichuan University, 610065 Chengdu, People's Republic of China

Received 24 March 2013; accepted in revised form 19 May 2013

Abstract. We report a method to prepare the poly(vinyl alcohol)/reduced graphene oxide (PVA/rGO) nanocomposites with low percolation threshold and high electrical conductivity by using the large-area reduced graphene oxide (LrGO) sheets. The large-area graphene oxide (LGO) sheets are expected to overlap better with each other and form the continuous GO network in PVA matrix than small-area graphene oxide (SGO). During the thermal reduction process, the LGO sheets are easily restored and improve the electrical conductivity of nanocomposites due to their low damage level of conjugate-structure. As a result, the percolation threshold of PVA/LrGO nanocomposites is ~0.189 wt% lower than present reports (0.5~0.7 wt%). At the LrGO content of 0.7 wt%, the electrical conductivity of PVA/LrGO nanocomposites reaches $6.3\cdot10^{-3}$ S/m. Besides that, this method only takes 15~30 min to reduce the PVA/GO nanocomposites effectively.

Keywords: *nanocomposites, poly(vinyl alcohol), large-area rGO, thermal reduction, electrical conductivity*

1. Introduction

Conductive polymer composites have been used in a wide range of important technological applications, such as sensor, anti-static, microwave absorbing, and conductive coating. These composites are prepared by compounding the polymer and conductive nanoparticles (such as carbon black, carbon nanotubes, carbon fiber, graphite and metal particles) [1, 2]. When the content of conductive nanoparticle reaches to a critical value (i.e. percolation threshold), a continuous electrical conductive network is formed by these conductive nanoparticles, rendring the polymer composite electrically conductive [3, 4] So the nanoparticles' electrical conductivity, dispersibility and the interaction with polymer matrix directly affect the property of the electrical conductive network and define the final electrical conductivity of polymer composites. According to the percolation theories, the percolation threshold depends on the filler shape, size and aspect ratio. A larger aspect ratio filler can more effectively decrease the percolation threshold of nanocomposites than a small one [5, 6]. Besides that, the electrical conductivity of nanocomposites is also defined by the filler's pristine conductivity.

Graphene – a two-dimensional monolayer of sp^2-carbon atom, is widely considered to be an ideal material for preparing the conductive polymer composites due to its high electrical conductivity (10^6 S/cm), the high ratio of diameter to thickness and the excellent mechanical properties [7]. However, the strong π-π interaction between graphene

---

[*]Corresponding author, e-mail: qiangfu@scu.edu.cn

sheets make them hardly dispersible in some organic solvents and polymer matrix homogenously, so it is difficult for them to form the continuous conductive network in a polymer matrix, especially at low graphene content. At present, the oxidation-reduction process is an efficient and common method to improve the dispersibility of graphene sheets in many polymer matrices and organic solvents. Firstly, making the graphene surface grafted with a lot of oxygen-functional groups by oxidation reaction, these polar groups increase the repellent force between graphene sheets and then separate them, so these separated graphene oxide (GO) sheets could be homogenously dispersed in many polymer matrices and organic solvents; the second step is to remove these polar groups in order to restore the electrical conductivity of GO sheets.

Due to the partial re-aggregation of the rGO sheets during the reduction processing, the surfactant agents or ultrasonic treatment are usually used to re-disperse the rGO sheets in the polymer matrix. After the reduction of GO sheets, the surfactant agents could form a coating layer on the surface of rGO sheets, those coating layer could make the separation of these sheets from each other and then helps the dispersion of the rGO sheets in the polymer matrix homogeneously. Due to the insulating properties of the surfactant agents, the coating layer would hinder the efficient charge transport, and decrease the final electrical conductivity of composites [8]. Besides that, these surfactant agents would play the role of the plasticization, and decrease the mechanical properties of composites. The ultrasonic treatment could assist the dispersion of nanofiller, but it would decrease the size of GO sheets and increase the structure defects of the GO sheets, these factors are disadvantageous for improving the final electrical conductivity of rGO sheets.

Our aim is to achieve the high electrical conductive polymer/rGO nanocomposite, so in our work we not only need using the large aspect ratio nanofiller, but also need optimizing the dispersion.

Zhao *et al*. [9] reported that the large area reduced graphene oxide (LrGO) sheets have lower intersheet contact resistance and less damaged conjugation structure level than that of small-area reduced graphene oxide (SrGO) sheets, and could be used to prepare the transparent conductive films with 840 Ω/sq at 78% transmittance, which was lower than that be made from the SrGO (19.1 kΩ/sq at 78% transmittance). So the LrGO sheets have following two advantages which are more suitable for improving the electrical conductivity of nanocomposites than the small one: 1) there are less intersheet junctions leading to the high intrinsic electrical conductivity, and 2) the large area is prone to form a continuous electrical conductive network.

GO sheets could be reduced in different media such as water [10], ethanol, butanol, and ethylene glycol [11] at a special temperature, and the GO sheets also could be reduced in polymer matrix such as poly (vinylpyrrolidone), poly(vinyl acetate) [12] or polyvinylidene fluoride [13]. Glover *et al*. [12] reported that the GO sheets could be reduced in PVA matrix at the temperature range from 150 to 250°C, and the result of Raman peak shift shown that the C:O ratio is less than 10 after reduction. However, this method can maintain the good dispersion of rGO sheets and get rid of introducing the surfactant agents into polymer matrix [14, 15], meanwhile avoids using reducing agents, especially hazardous ones.

In this work, we use poly(vinyl alcohol) (PVA) as polymer matrix, and disperse the GO sheets in PVA matrix homogeneously through the interaction between the hydroxyl groups on the PVA chains and oxygen-functional groups located on the surface of GO sheets, and then to reduce the GO sheets through the in-situ thermal reduction at a special temperature which depends on the decomposition temperature of PVA [12, 13, 16]. In our method, there are two purposesintended, 1) usage of the LGO sheets to construct a continuous filler network, and 2) avoiding the introduction of reducing and surfactant agents during the reduction processing. The effect of electrical conductive network structure morphology on the final electrical conductivity of nanocomposites is studied through comparing the PVA/LrGO and PVA/SrGO nanocomposites.

2. Experimental

2.1. Materials

Artificial graphite power with an average size of 200 μm were purchased from Qingdao Black Dragon graphite Co., Ltd, PVA was 99% hydrolyzed with an average polymerization degree of 1700 (SINOPEC Sichuan vinylon works). Potassium permanganate ($KMnO_4$), sulfuric acid (H_2SO_4 98%), hydrogen peroxide (H_2O_2) and sodium nitrate ($NaNO_3$), sodium hydroxide (NaOH), above-mentioned chemical agents were purchased from Kermel Chemical reagent plant (Tianjin, China). They were used as received.

2.2. Preparation of the LGO and SGO sheets

GO sheets were obtained by Hummer's method [17]. Graphite (1 g) was mixed with $NaNO_3$ (1 g) in H_2SO_4 (48 ml) at 0°C (ice bath), $KMnO_4$ (6 g) was slowly added in 1 h. After that, the reaction mixture was first stirred at 0°C for 2 h and then at 30°C for 2.5 h. Deionized water (150 mL) was slowly added to the reaction system and stirred for 1.5 h to obtain a graphite oxide suspension. The mixture was treated with 5% H_2O_2 (50 mL), filtered and washed with hot water until completely remove the residual salts and acids. For obtaining the LGO sheets, a low-speed centrifugation at 4000 rpm was first used to remove thick multilayer flakes until all the visible particles were removed (15 min), then the supernatant was further centrifuged at 8000 rpm for 7 min to separate precipitate (LGO) and supernatant, the SGO sheets were prepared by ultrasonication of above-mentioned LGO sheets at the power of 100 W for 45 min. The area distribution of LGO and SGO sheets was counted by scanning electron microscopy (SEM).

2.3. Preparation of PVA/rGO nanocomposites

The PVA/LGO and PVA/SGO nanocomposites with different filler contents were prepared as follows: PVA (1 g) was dissolved in deionized water (10 mL) at 98°C for 1 h. The aqueous dispersion of the LGO or SGO sheets was gradually dropped into the PVA solution, and stirred at 98°C for 30 min. No precipitate was observed in a few hours after magnetic stirring indicating that no aggregation of the LGO or SGO sheets occurred. The homogeneous PVA/LGO or PVA/SGO solution was poured into an aluminum dish and kept at 60°C for 15 h to cast film. The thickness of the obtained films is about 0.1 mm.

The PVA/LGO or PVA/SGO nanocomposites films were reduced through thermal reduction, firstly keep these samples in the furnace filled with N_2, then increase the temperature of samples to reduction temperature at the rate of 10°C/min, and maintain the sample at special reduction temperature for 0, 10, 15, and 30 min respectively. According to the weight ratio of GO (dry weight) to PVA, the reduction temperature and time, the nanocomposites films were denoted as PVA/LrGO-*x* wt%-*y*°C-*z* min or PVA/SrGO-*x* wt%-*y*°C-*z* min, where *x*, *y* and *z* stand for the rGO content in PVA, the reduction temperature and time respectively. By the way, in section 3.3, the total time means the whole reduction period for preparing the sample which includes the heating time and reduction time.

Furthermore, the effect of the networks formed by SrGO or LrGO sheets on the electrical conductivity is studied by swelling treatment. The method is immersing the nanocomposites films in reverse osmosis water (with the resistance of 18 MΩ) for 15 h at room temperature, and then they are freeze-dried. It can be expected the network would be destroyed due to water swelling, and it causes the change of the electrical conductivity of the nanocomposites. So the above-mentioned effect may be revealed by the change of the electrical conductivity.

2.4. Characterization

The FEI Inspect F scanning electron microscopy (Inspect F, FEI Company, USA) with the an acceleration voltage of 5 kV was used to measure the area of LGO and SGO sheets which were spin-coated onto freshly cleaved ITO substrates, about 150 pieces of LGO or SGO sheets were measured.

The resistance of the films was measured with Keithley 6487 electrometer (Keithley Instruments, Inc, Ohio, USA). Two-point method was used. Silver paint was applied to both ends of the sample to ensure good contact. As a result, contact resistance is negligible comparing to sample resistance. The bulk conductivity was calculated by Equation (1):

$$\sigma = \frac{L}{R \cdot S} \tag{1}$$

where *L*, *R* and *S* are the length, resistance and cross sectional area of the specimen, respectively. In addition, the electrical conductivity of nanocomposites was measured along the films. Previous researches indicated that the GO sheets tend to align parallel with the film surface [15], indicating that the charges are prone to transport along the films surface instead in perpendicular direction. So the electrical conductivity along the films surface is expected to be higher than that in perpendicular direction.

TGA (Q500, TA Instruments, USA) was performed under N_2 from the room temperature to 260°C at a rate of 10°C/min.

3. Results and discussion

3.1. The decision of the reduction temperature

TGA and DSC are used to characterize the thermal reduction processing of GO sheets (Figure 1). TGA result shows that LGO and SGO sheets exhibit a dramatic mass loss when reduction temperature reaches 215°C. This indicates that the GO sheets lose some oxygen functional groups in the temperature range of 150~215°C, and become the rGO sheets. The derivative weight curves of LGO and SGO sheets reveal that the strong reduction reaction occurs at the temperature of 195 and 199°C. Due to the onset decomposition temperature of PVA matrix is 219°C, the reduction temperature for reducing the PVA/GO nanocomposites are set as 150, 160, 170, 175, 180 and 200°C.

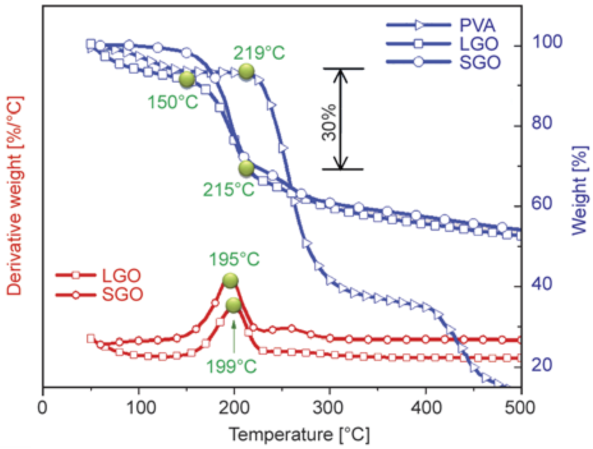

Figure 1. The TGA plots of PVA, LGO and SGO

3.2. The Properties of GO

Figures 2a and 2b show the typical SEM pictures of the LGO and SGO sheets. Based on the measurements of 150 pieces of LGO and SGO sheets, the respective area distribution is shown in Figures 2c and 2d. It can be clearly seen that about 49% of LGO sheets are larger than 500 μm^2, and 28% of LGO

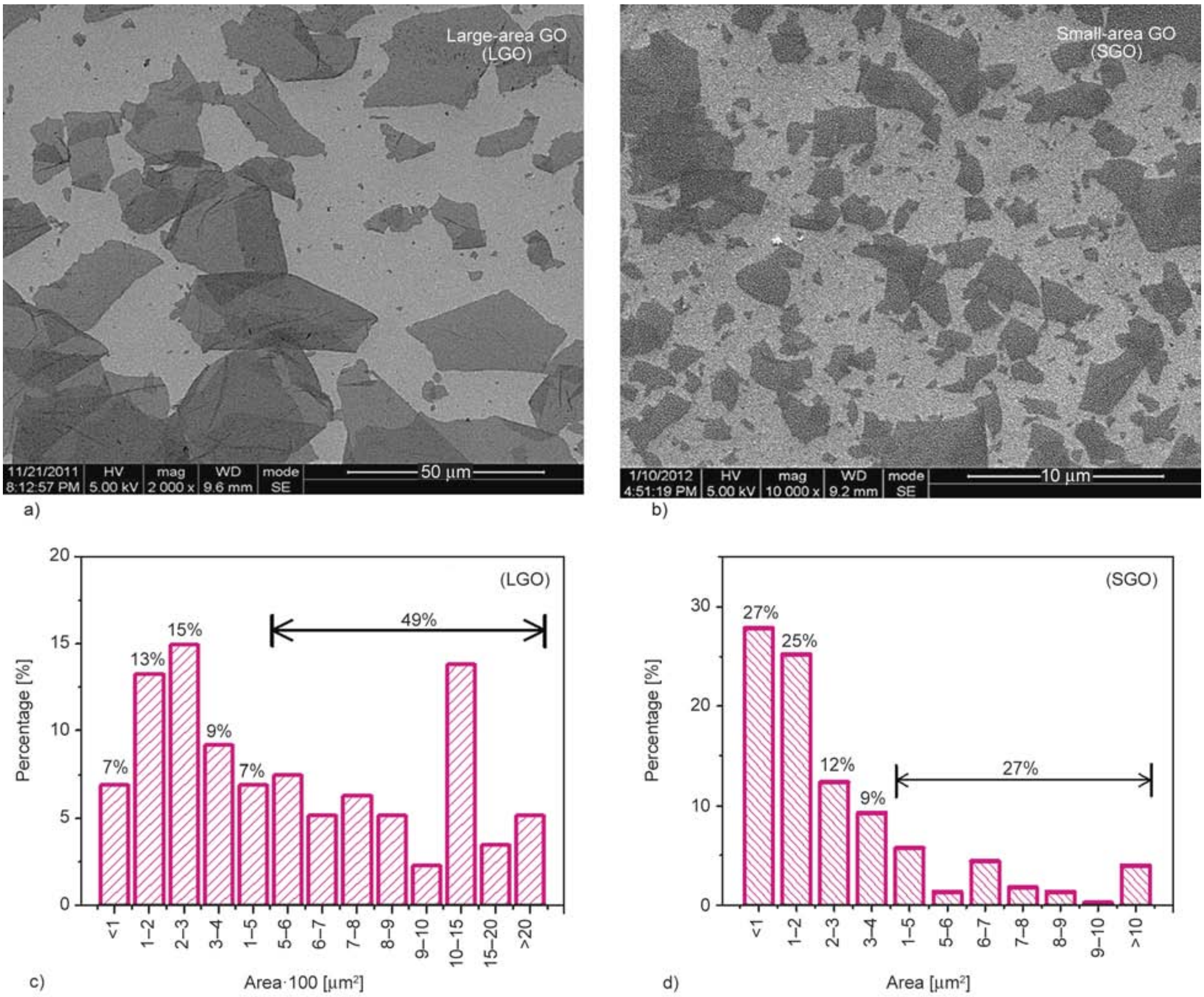

Figure 2. The SEM pictures of LGO (a) sheets and SGO sheets (b), which is used to count the area of LGO sheets (c) and SGO sheets (d)

sheets has an area of ca.100~200 µm^2. Due to the existence of weak C–O–C and stretched C–C bonds on the surface of LGO sheets, the LGO sheets are broken into small ones after ultrasonic treatment, result ~73% of SGO sheets with an area less than 5 µm^2 (Figures 2b and 2d). After reduction, the resistance of LrGO film is 1.55 KΩ/square which is lower than that of SrGO (8.97 KΩ/square), demonstrating that the LrGO sheets have better electrical conductivity and lower resistance than SrGO sheets [9].

3.3. The electrical conductivity of the nanocomposites

In our work, the electrical conductivity of the PVA/LrGO nanocomposites is already $2.5\cdot10^{-6}$ S/m at the LrGO content of 0.3 wt%, which is higher than that of PVA/SrGO at the same filler content. Furthermore, the electrical conductivity of PVA/LrGO nanocomposites increases to $2.09\cdot10^{-4}$ S/m with the addition of 1 wt% LrGO (Figure 3a). It indicates that the LrGO sheets could more efficiently improve the electrical conductivity of nanocomposites than SrGO sheets. The power law (see Equation (2)) is used to analyze electrical conductivity in order to reveal that the LrGO could decrease the percolation threshold of nanocomposites [18]:

$$\sigma \propto \sigma_0(\varphi - \varphi_c)^{\upsilon} \qquad (2)$$

where σ_0 is the bulk electrical conductivity of the fillers, φ is the filler volume fraction, and υ is the universal critical exponent which depends on the dimensionality of the conductive network. The percolation threshold (φ_c) is the critical content above which a continuous connected network is formed for the transport of electrons throughout the matrix. Hence, it can be calculated that the φ_c value is 0.198 and 0.27 wt% for the sample of PVA/LrGO-150°C-15 min and PVA/SrGO-150°C-15 min respectively (Figures 3b and 3c). Comparing with the percolation threshold reported in others' works (between 0.5~1 wt%) [19, 20], the percolation threshold of PVA/LrGO nanocomposites is only 0.198 wt%. Besides that, the electrical conductivity of PVA/LrGO-0.3 wt%-150°C-15 min is $2.5\cdot10^{-6}$ S/m, better than that of PVA/rGO nanocomposites reported in refs. [19] and [20], in which the electrical conductivity of nanocomposites was below 10^{-12} S/m at the 0.3 wt% rGO contents. In summary, the LrGO sheets not only decrease the percolation threshold, but also could improve the electrical conductivity of nanocomposites especially at a low content of LrGO.

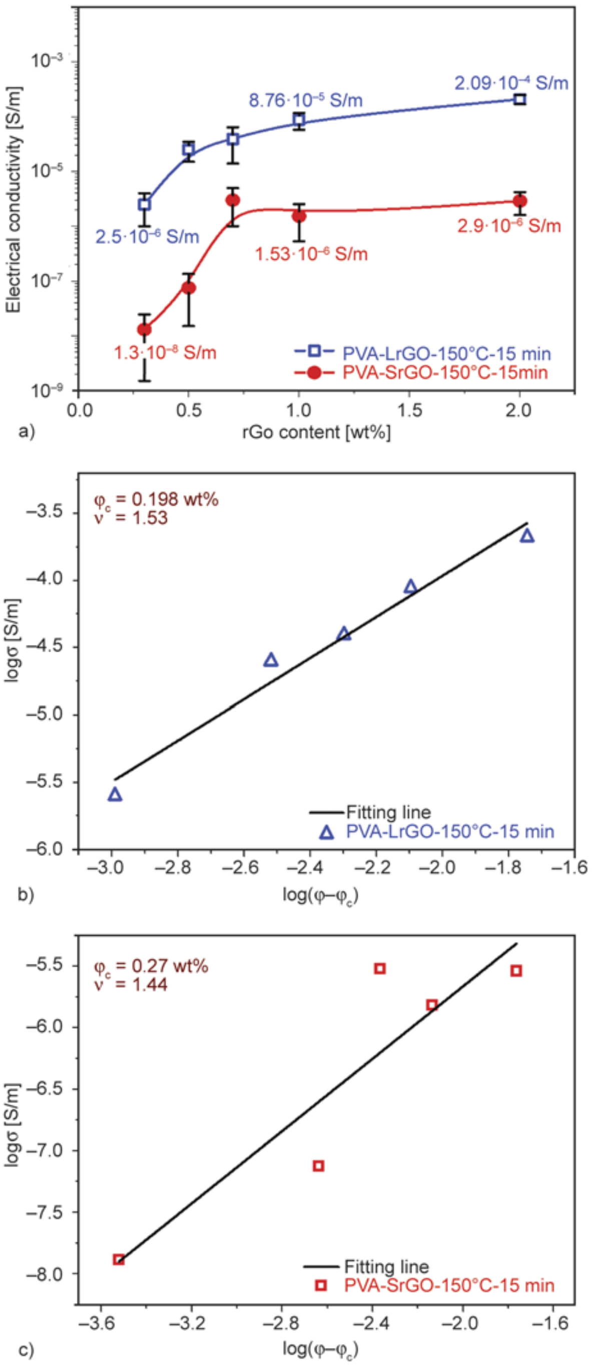

Figure 3. a) The electrical conductivity of PVA-LrGO-150°C-15 min and PVA-SrGO-150°C-15 min as a function of the rGO content. b) and c) are the double-logarithmic plot of electrical conductivity versus ($\varphi - \varphi_c$) for the samples of PVA-LrGO-150°C-15 min and PVA-SrGO-150°C-15 min

Moreover, the high reduction temperature could make the nanocomposites films having high electrical conductivity. The electrical conductivity of PVA/LrGO nanocomposites increases more remarkably than those of PVA/SrGO nanocomposites. As shown in Figure 4a, the electrical conductivity of PVA/LrGO greatly increased from $9.8\cdot10^{-8}$ to $6.3\cdot10^{-3}$ S/m with increasing the reduction temperature. The electrical conductivity increased to the highest value at the reduction temperature of 200°C, indicating that the critical temperature for the thermal reduction in PVA/GO system is 200°C. According to results of derivative weight, it can be known that the critical temperature is the reduction temperature of GO. So when the thermal reduction temperature exceeds the critical temperature, the electrical conductivity of nanocomposites can be improved remarkably, otherwise, it should be not.

The Figures 4b and 4c show the change of electrical conductivity as increasing the reduction time at low temperature and high temperature respectively. Under the same reduction time, the electrical conductivity of the sample reduced at high reduction temperature is always higher than that reduced at low reduction temperature (Figures 4a and 4c), indicating the high temperature is more efficient for reducing the GO sheets than low temperature. The long reduction time also could improve the electrical conductivity of nanocomposites (Figures 4b and 4c). For example (Table 1), the final electrical conductivities of the PVA/LrGO-0.7 wt%-200°C-0 min and PVA/LrGO-0.7 wt%-150°C-30 min are much closer; but the total time (including the heating time and reduction time) of former is 17 min shorter than that of latter (42 min). Therefore from the perspective of reduction efficiency, the high reduction temperature is a more efficient way to improve electrical conductivity of nanocomposites in comparison with extending the reduction time.

Table 2 is listed for comparing the final electrical conductivity of nanocomposites prepared by our method with that reported by others, in which the rGO sheets were re-dispersed by surfactant agents. The results show that the electrical conductivity reported by us is $6.3\cdot10^{-3}$ S/m higher than others' at the rGO content of 0.3~0.7 wt% [19, 20], the electrical conductivity of them did not being mentioned or is about 10^{-5} S/cm at 1 wt% rGO content [14, 20]. Due to that the surfactant agents hinder the overlap between rGO sheets [21], increase the contact resistance. So the thermal reduction could get rid of using surfactant and maintain the low contact resistance between the interlayer of rGO sheets. Besides that, this method only takes 15~30 min which is shorter than present chemical reduction process (takes 24 h [15, 20]). In summary, the thermal reduction is an efficient way to prepare the nanocomposites with low percolation threshold and high electrical conductivity, and also is suitable for preparing the ther-

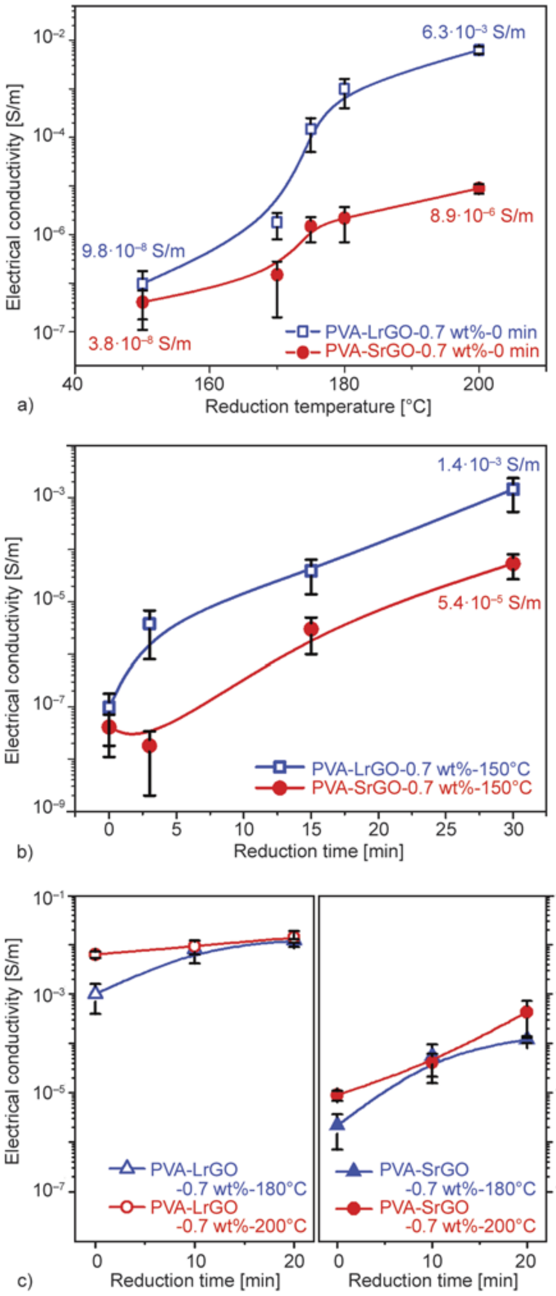

Figure 4. a) The electrical conductivity of PVA-LrGO-0.7 wt%-0 min and PVA-SrGO-0.7 wt%-0 min as a function of the reduction temperature, b) the electrical conductivity of PVA-LrGO-0.7 wt%-150°C and PVA-SrGO-0.7 wt.%-150°C as a function of the reduction time, and c) the electrical conductivity of PVA-LrGO-0.7 wt%-180°C, PVA-LrGO-0.7 wt%-200°C, PVA-SrGO-0.7 wt%-180°C and PVA-SrGO-0.7 wt%-200°C as a function of the reduction time

Table 1. The electrical conductivity of PVA/rGO nanocomposites and the total time for preparing them

Sample	Electrical conductivity [S/m]	Heating time [min]	Reduction time [min]	Total time [min]
PVA/LrGO-0.7 wt%-200°C-0 min	$6.3\cdot10^{-3}$	17	0	17
PVA/LrGO-0.7 wt%-200°C-10 min	$9.2\cdot10^{-3}$	17	10	27
PVA/LrGO-0.7 wt%-150°C-0 min	$9.8\cdot10^{-8}$	12	0	12
PVA/LrGO-0.7 wt%-150°C-30 min	$1.4\cdot10^{-3}$	12	30	42
PVA/SrGO-0.7 wt%-200°C-0 min	$8.9\cdot10^{-6}$	17	0	17
PVA/SrGO-0.7 wt%-200°C-10 min	$1.4\cdot10^{-5}$	17	10	27
PVA/SrGO-0.7 wt%-150°C-0 min	$3.8\cdot10^{-8}$	12	0	12
PVA/SrGO-0.7 wt%-150°C-30 min	$5.4\cdot10^{-5}$	12	30	42

Table 2. The electrical conductivity of PVA/rGO nanocomposites comparing between our results and literature [14, 15, 19, 20]

rGO content	Surfactant	Electrical conductivity	Reduced agents or method	Reduction Time	Reference
3 vol%	SDBS	–	Hydrazine	30 min	14
1.6 wt%	–	10^{-9} S/cm	Hydrazine	24 hour	20
3.5 wt%	–	–	Hydrazine	24 hour	15
1 wt%	2-propanol	10^{-5} S/cm	Hydrazine	Overnight	19
0.7 wt%	–	$6.3\cdot10^{-3}$ S/m	Thermal reduction at 200°C	17 min	Our work

moset or thermoplastic polymer/rGO nanocomposites through reducing the GO sheets at appropriate temperature.

3.4. The structure of the electrical networks

The mechanism of electrical conductivity of the nanocomposites is based on two factors. The first one is the intrinsic electrical conductivity of nanofiller. In this system, the electrical conductivity of LrGO sheets is higher than that of SrGO sheets, it could affect the final electrical conductivity of nanocomposites, but the interesting thing is that the resistance difference between LrGO sheets (1.55 KΩ/square) and SrGO (8.97 KΩ/square) sheets is only one order of magnitude while the electrical conductivity difference between the LrGO/PVA and SrGO/PVA nanocomposites is two or three orders of magnitude under the same reduced condition. This question would be answered through analyzing the structure of electrical conductive network formed by LrGO or SrGO sheets in PVA matrix.

The swelling treatment is used to study the effect of the SrGO and LrGO sheets on the electrical conductive network morphology in nanocomposites. Figure 5 shows that the electrical conductivity of the nanocomposites decreased after swelling. The electrical conductivity of PVA/LrGO-1 wt%-180°C-10 min is decreased from $3.4\cdot10^{-2}$ to $3.6\cdot10^{-4}$ S/m (Figure 5a); and that of PVA/SrGO-1 wt%-180°C-10 min also decrease from $2.1\cdot10^{-4}$ to $1.77\cdot10^{-7}$ S/m

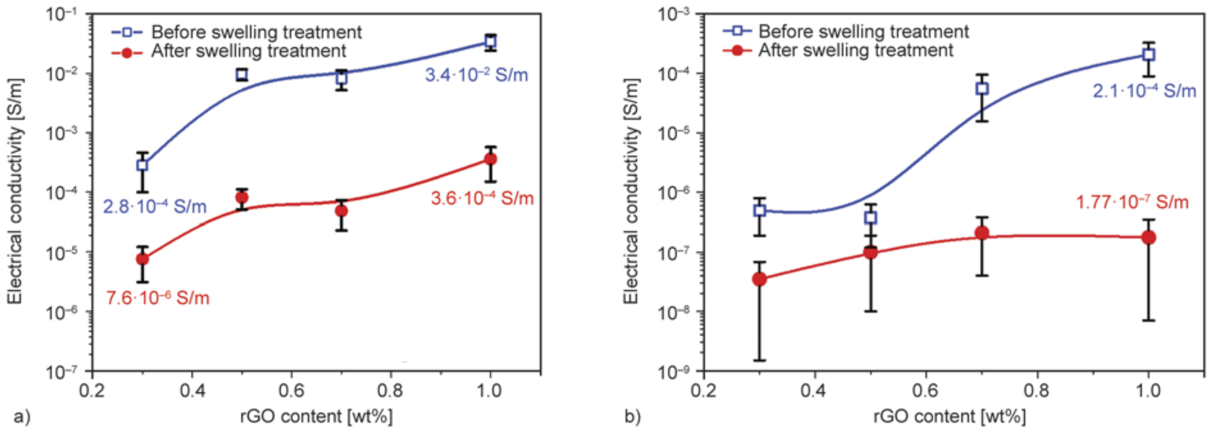

Figure 5. The change of the electrical conductivity of PVA-LrGO-180°C-10 min (a) and PVA-SrGO-180°C-10 min (b) before (blue curve) and after (red curve) swelling treatment

(Figure 5b). Because the electrical conductivity of LrGO or SrGO sheets in nanocomposites doesn't change during the swelling treatment, so the decreased electrical conductivity of nanocomposites may be due to the destroyed conductive networks. During the swelling treatment, water molecules could intercalate between the rGO sheets, open the contact points of rGO sheets, and then destroy the electrically conductive network, causing the decrease of the electrical conductivity of the nanocomposites. Figure 5 shows that the decrease of electrical conductivity of PVA/LrGO nanocomposites is less than that of PVA/SrGO nanocomposites after the swelling treatment, indicating that the network formed by LrGO sheets is firmer than that formed by SrGO sheets, and could not be destroyed easily by swelling treatment. Besides that, the LrGO sheets are prone to overlap with each other due to their large aspect ratio, and form a continuous conductive network at low filler content, causing the PVA/LrGO nanocomposites having low percolation threshold.

4. Conclusions

This is an efficient method to preparing the low percolation threshold and high electrical conductivity PVA/rGO nanocomposites by using large area GO sheets. The LGO sheets would recover their electrical conductivity efficiently after being reduced due to the low degree of oxidation. The LrGO sheets could construct a continuous and firm network in PVA matrix due to their high aspect ratio. The formed continuous electrically conductive network could remarkably improve the electrical conductivity of PVA/LrGO nanocomposites. Besides, the thermal reduction process is a fast method for preparing electrical conductive polymer/LrGO nanocomposites which only takes 15~30 min. This method solves four problems existing in the process of preparing nanocomposites, which are 1) avoiding using the surfactant to redisperse the rGO sheets, 2) shortening the preparation period, 3) simplifying the post-treatment, 4) as well as increasing the electrical conductivity of nanocomposites at low rGO contents.

References

[1] Li N., Cheng W., Ren K., Luo F., Wang K., Fu Q.: Oscillatory shear-accelerated exfoliation of graphite in polypropylene melt during injection molding. Chinese Journal of Polymer Science, **31**, 98–109 (2013).
DOI: 10.1007/s10118-013-1204-0

[2] Lin L., Deng H., Gao X., Zhang S., Bilotti E., Peijs T., Fu Q.: Modified resistivity–strain behavior through the incorporation of metallic particles in conductive polymer composite fibers containing carbon nanotubes. Polymer International, **62**, 134–140 (2013).
DOI: 10.1002/pi.4291

[3] Gao X., Zhang S., Mai F., Lin L., Deng Y., Deng H., Fu Q.: Preparation of high performance conductive polymer fibres from double percolated structure. Journal of Materials Chemistry, **21**, 6401–6408 (2011).
DOI: 10.1039/C0JM04543H

[4] Long G., Tang C., Wong K-W., Man C., Fan M., Lau W-M., Xu T., Wang B.: Resolving the dilemma of gaining conductivity but losing environmental friendliness in producing polystyrene/graphene composites via optimizing the matrix-filler structure. Green Chemistry, **15**, 821–828 (2013).
DOI: 10.1039/c3gc37042a

[5] Kovacs J. Z., Velagala B. V., Schulte K., Bauhofer W.: Two percolation thresholds in carbon nanotube epoxy composites. Composites Science and Technology, **67**, 922–928 (2007).
DOI: 10.1016/j.compscitech.2006.02.037

[6] Zhang S. M., Lin L., Deng H., Gao X., Bilotti E., Peijs T., Zhang Q., Fu Q.: Synergistic effect in conductive networks constructed with carbon nanofillers in different dimensions. Express Polymer Letters, **6**, 159–168 (2012).
DOI: 10.3144/expresspolymlett.2012.17

[7] Novoselov K. S., Geim A. K., Morozov S. V., Jiang D., Zhang Y., Dubonos S. V., Grigorieva I. V., Firsov A. A.: Electric field effect in atomically thin carbon films. Science, **306**, 666–669 (2004).
DOI: 10.1126/science.1102896

[8] Grossiord N., Loos J., Regev O., Koning C. E.: Toolbox for dispersing carbon nanotubes into polymers to get conductive nanocomposites. Chemistry of Materials, **18**, 1089–1099 (2006).
DOI: 10.1021/cm051881h

[9] Zhao J., Pei S., Ren W., Gao L., Cheng H-M.: Efficient preparation of large-area graphene oxide sheets for transparent conductive films. ACS Nano, **4**, 5245–5252 (2010).
DOI: 10.1021/nn1015506

[10] Liao K-H., Mittal A., Bose S., Leighton C., Mkhoyan K. A., Macosko C. W.: Aqueous only route toward graphene from graphite oxide. ACS Nano, **5**, 1253–1258 (2011).
DOI: 10.1021/nn1028967

[11] Nethravathi C., Rajamathi M.: Chemically modified graphene sheets produced by the solvothermal reduction of colloidal dispersions of graphite oxide. Carbon, **46**, 1994–1998 (2008).
DOI: 10.1016/j.carbon.2008.08.013

[12] Glover A. J., Cai M., Overdeep K. R., Kranbuehl D. E., Schniepp H. C.: *In situ* reduction of graphene oxide in polymers. Macromolecules, **44**, 9821–9829 (2011).
DOI: 10.1021/ma2008783

[13] Tang H., Ehlert G. J., Lin Y., Sodano H. A.: Highly efficient synthesis of graphene nanocomposites. Nano Letters, **12**, 84–90 (2011).
DOI: 10.1021/nl203023k

[14] Zhao X., Zhang Q., Chen D., Lu P.: Enhanced mechanical properties of graphene-based poly(vinyl alcohol) composites. Macromolecules, **43**, 2357–2363 (2010).
DOI: 10.1021/ma902862u

[15] Yang X., Li L., Shang S., Tao X-M.: Synthesis and characterization of layer-aligned poly(vinyl alcohol)/graphene nanocomposites. Polymer, **51**, 3431–3435 (2010).
DOI: 10.1016/j.polymer.2010.05.034

[16] Zheng D., Tang G., Zhang H-B., Yu Z-Z., Yavari F., Koratkar N., Lim S-H., Lee M-W.: *In situ* thermal reduction of graphene oxide for high electrical conductivity and low percolation threshold in polyamide 6 nanocomposites. Composites Science and Technology, **72**, 284–289 (2012).
DOI: 10.1016/j.compscitech.2011.11.014

[17] Hummers W. S., Offeman R. E.: Preparation of graphitic oxide. Journal of the American Chemical Society, **80**, 1339 (1958).
DOI: 10.1021/ja01539a017

[18] Kovacs J. Z., Velagala B. S., Schulte K., Bauhofer W.: Two percolation thresholds in carbon nanotube epoxy composites. Composites Science and Technology, **67**, 922–928 (2007).
DOI: 10.1016/j.compscitech.2006.02.037

[19] Salavagione H. J., Martínez G., Gómez M. A.: Synthesis of poly(vinyl alcohol)/reduced graphite oxide nanocomposites with improved thermal and electrical properties. Journal of Materials Chemistry, **19**, 5027–5032 (2009).
DOI: 10.1039/B904232F

[20] Bao C., Guo Y., Song L., Hu Y.: Poly(vinyl alcohol) nanocomposites based on graphene and graphite oxide: A comparative investigation of property and mechanism. Journal of Materials Chemistry, **21**, 13942–13950 (2011).
DOI: 10.1039/C1JM11662B

[21] Wang J., Zhou T., Deng H., Chen F., Wang K., Zhang Q., Fu Q.: An environmentally friendly and fast approach to prepare reduced graphite oxide with water and organic solvents solubility. Colloids and Surfaces B: Biointerfaces, **101**, 171–176 (2013).
DOI: 10.1016/j.colsurfb.2012.06.008

eXPRESS Polymer Letters Vol.7, No.9 (2013) 756–766
Available online at www.expresspolymlett.com
DOI: 10.3144/expresspolymlett.2013.73

Electrically conductive bacterial cellulose composite membranes produced by the incorporation of graphite nanoplatelets in pristine bacterial cellulose membranes

T. Zhou[1*], *D. Chen*[1], *J. Jiu*[2], *T. T. Nge*[2], *T. Sugahara*[2], *S. Nagao*[2], *H. Koga*[2], *M. Nogi*[2], *K. Suganuma*[2], *X. Wang*[3], *X. Liu*[3], *P. Cheng*[4], *T. Wang*[1], *D. Xiong*[1]

[1]School of Materials Science and Engineering, Nanjing University of Science and Technology, 210094 Nanjing, China
[2]Institute of Scientific and Industrial Research, Osaka University, Mihogaoka 8-1, Ibaraki, 567-0047 Osaka , Japan
[3]Key Laboratory for Soft Chemistry and Functional Materials of Ministry Education, Nanjing University of Science and Technology, 210094 Nanjing, China
[4]National Key Laboratory of Science and Technology on Micro/Nano Fabrication, Key Laboratory for Thin Film and Microfabrication of the Ministry of Education, Research Institute of Micro/Nano Science and Technology, Shanghai Jiao Tong University, 200240 Shanghai, China

Received 8 April 2013; accepted in revised form 1 June 2013

Abstract. Graphite nanoplatelets (GNPs) were utilized to improve the electrical conductivity of pristine bacterial cellulose (BC) membranes. By physical and chemical methods, flake-shaped GNPs, weaving through the surface layer of web-like cellulose nanofibrils, were indeed fixed or trapped by the adjacent nanofibrils in the BC surface network, for comparison, rod-shaped multi-walled carbon nanotubes (MWCNTs) were homogeneously inserted into BC membrane through the pore structures and tunnels within the BC membrane. Strong physical and chemical interaction exists between the BC nanofibrils and the particles of GNP or MWCNT even after 15 h sonication. BC membrane with 8.7 wt% incorporated GNPs reached the maximum electrical conductivity of 4.5 S/cm, while 13.9 wt% MWCNT/BC composite membrane achieved the maximum electrical conductivity of 1.2 S/cm. Compared with one dimensional (1-D) MWCNTs, as long as GNPs inserted into BC membranes, the 2-D reinforcement of GNPs was proven to be more effective in improving the electrical conductivity of BC membranes thus not only break the bottleneck of further improvement of the electrical conductivity of BC-based composite membranes but also broaden the applications of BC and GNPs.

Keywords: *polymer composites, nanocomposites, electrical conductivity, graphite nanoplatelets, bacterial cellulose membrane*

1. Introduction

Bacterial cellulose (BC), bacteria-produced natural biopolymer composed of ribbon-shaped nanofibers (<100 nm wide), is distinguished by its extensive hydrogen bonding-stabilized ultrafine porous three-dimensional (3-D) weblike structure [1, 2]. Since each BC nanofiber is a bundle of cellulose nanofibrils which are aggregates of semicrystalline extended cellulose chains, the coefficient of thermal expansion of BC nanofibers in the axial direction is similar to that of glass (as small as 0.1 ppm/K), the Young's modulus (~138 GPa) and tensile strength (estimated to be at least 2 GPa) of BC nanofibers are almost equal to those of aramid fibers (e.g., Kevlar, a well-known high-strength fiber) [3, 4]. As a renewable and natural resources-based biodegradable polymers with great industrial potential (low cost production on a large scale), especially on account of

---

[*]Corresponding author, e-mail: ztltianle999@hotmail.com

its unique structure and notable properties that can be converted into high value products, BC, nowadays, has attracted rapidly growing worldwide scientific interest in which particular attention has been paid to BC-based advanced functional materials, such as electrically conductive BC-based composite membranes [1, 2].

Carbon nanotubes (CNTs), a type of one-dimensional (1-D) carbon nanomaterials with remarkable electrical conductivity, have been utilized in improving the electrical conductivity of insulating BC membranes for use in electronics such as electrodes [5–10]. Yoon and coworkers [5, 6] dipped BC membrane in a surfactant-stabilized 0.05 wt% multi-walled CNT (MWCNT) well-dispersed aqueous solution for 24 h, consequently MWCNTs were found to be inserted in the BC membrane and the electrical conductivity of MWCNT/BC composite membranes with different MWCNTs' surfactants, cationic cetyltrimethylammonium bromide (CTAB) or sodium dodecylbenzenesulfonate (NaDDBS), greatly increased to 1.4×10^{-1} and 4.2×10^{-1} S/cm, respectively. Jung *et al.* [7] also utilized BC membrane as the template to deposit MWCNTs uniformly, then used silk fibroin as coating material for the MWCNT-incorporated BC membrane, the electrical conductivities of the resulting composite membranes consequently achieved respectively 5.3×10^{-3} and 3.6×10^{-3} S/cm from CTAB-stabilized 0.03 or 0.05 wt% MWCNT aqueous dispersion (immersion time was unaccounted). Kim *et al.* [8] fabricated electrically conductive composite membrane with a surface resistance of 2.8 kΩ/sq by immersing BC membrane in a NaDDBS-stabilized 0.01 wt% single-walled CNTs (SWCNTs) aqueous dispersion for 3 h. They also fabricated composite membranes containing similar amount of purified MWCNTs or Ag-doped MWCNTs by immersing BC membranes in CTAB-stabilized 0.03 wt% MWCNTs or Ag-doped MWCNTs aqueous dispersions for 24 h, which resulted in comparable electrical conductivities, 2.5×10^{-3} and 3.1×10^{-3} S/cm, respectively [9]. Yun *et al.* [10] introduced Pt-incorporated MWCNTs into MWCNT/BC composite membrane to improve the performances of electrodes of proton exchange membrane fuel cells and the final electrode had a sheet resistance of 80 Ω/sq.

Furthermore, graphenes, a type of two-dimensional (2-D) carbon nanomaterials with remarkable electrical conductivity, were also used to improve the electrical conductivity of insulated BC membranes for use in biosensor and tissue engineering. Feng *et al.* [11] dissolved BC in NaOH solution, mixed graphene oxide (GO) and BC aqueous suspension together and finally obtained GO/BC composite membrane with a electrical conductivity of 1.1×10^{-4} S/cm by filtering the colloidal aqueous suspension of GO and BC.

CNT has great challenge in composite applications especially due to its expensive production cost, particularly for the purifying process; meanwhile graphene, a single layer of hexagonally arrayed sp^2-bonded carbon, also has great challenge in composite applications since graphenes tend to form irreversible agglomerates or even restack to form graphite through van der Waals interactions during the production of bulk-quantity monolayer graphenes and their dispersion into matrices [12]. Recently, graphite nanoplatelet (GNP), a 2-D layered graphitic nanofiller composed of stacked graphene sheets, is considered as an alternative carbon-based electrically conductive nanofiller because of its comparable electrical conductivity, lower cost than CNT due to the abundance of naturally existing graphite as the source material for GNP, and easier large-scale processes than monolayer graphene since only one dimension, i.e. thickness, of the 2-D GNP falls within the nanoscaled range. However, using GNPs to improve the electrical conductivity of insulating BC membranes has not been considered yet. In this study, a new kind of BC-based composite, i.e. GNP/BC composite membranes with BC acting as a supporting material to deposit the well-dispersed GNPs, was prepared, not only to break the bottleneck of further improving the electrical conductivity of BC-based composite membranes, but also broaden the applications of BC and GNPs.

2. Experimental

2.1. Materials

BC wet membranes (20×20 mm^2, 3 mm thick), the bacterial-cell debris of which had already been removed by purified in sodium hydroxide after produced by *Gluconacetobacter xylinum*, were supplied by Hainan Yida Food Industry Co., Ltd., Hainan, China. The as-received gel-like white purified BC membranes were firstly neutralized by thoroughly washing with absolute ethanol before being stored in absolute ethanol in a sealed container at 4°C. As shown in Figure 1, BC utilized in this work has an

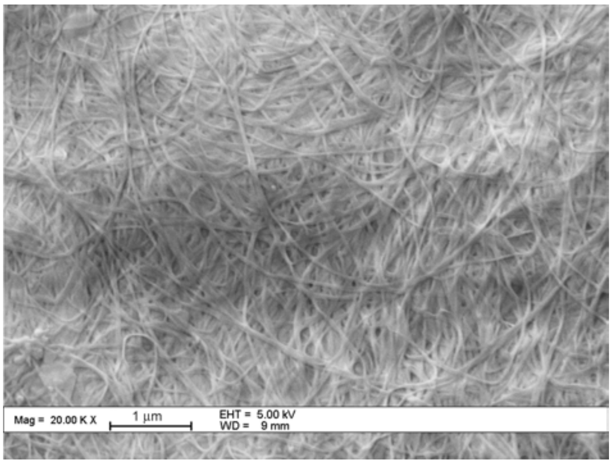

Figure 1. FESEM micrograph of the surface of air-dried BC membrane

ultrafine network structure consisted of a random assembly of nanofibrils with an average width of ~50 nm.

Graphite intercalation compound (GIC) particles (sized at 500 µm), composed of natural graphite particles intercalated by sulfuric acid, were supplied by Xinfangyuan Co. Ltd., Zaozhuang, China. According to the supplier's specification, the content of intercalants was about 15 wt% and the carbon content was higher than 99%.

MWCNTs, rather than SWCNTs or double-walled CNTs, have been predominantly used due to their relatively lower cost, better availability and easier dispersability. Purified MWCNTs utilized in this work were provided by Chengdu Organic Chemicals Co., Ltd., Chengdu, Chinese Academy of Sciences. According to the supplier's specification, the purified MWCNTs with an aspect ratio of 125–400 (50–80 nm in diameter and 10–20 µm in length) were synthesized by catalytic chemical vapor deposition. The purity and the specific surface area of the MWCNTs are greater than 95% and 40 m^2/g, respectively. Micrographs of the rod-shaped MWCNTs can be seen in our previous works [13]. During purification, MWCNTs were refluxed with concentrated nitric acid to remove catalyst particles, which may also increase the amount of oxygen chemisorbed on the surface of MWCNTs and, therefore, cause more oxygenous functional groups formed on the surface of MWCNTs. The Fourier-transform infrared (FTIR) spectrum, as shown in Figure 2, showed that there is a mass of hydroxyl groups (–OH) on the surface of as-received purified MWCNTs. Before stored in desiccators, MWCNTs were dried at 110°C for 24 h in vacuum to eliminate the agglomeration caused by hygroscopic absorption, as well as removing planar water, which would hinder the interaction between MWCNTs and surfactant.

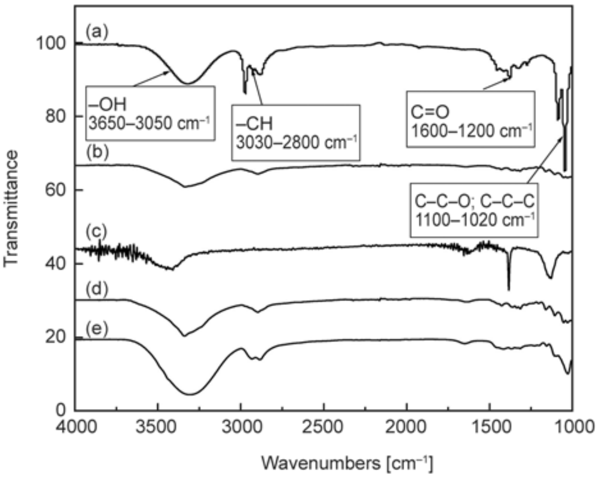

Figure 2. FTIR spectra of (a) GNPs, (b) BC membrane, (c) MWCNTs, (d) GNP-incorporated BC membrane and (e) MWCNT-incorporated BC membrane

Amino silane coupling agent, γ-aminopropyl-triethoxysilane (A1100), was obtained from Shanghai Chemical Reagent Co. Ltd., Shanghai, China. NaDDBS and other agents utilized were analytically pure grade and supplied by Sinopharm Chemical Reagent Co. Ltd., Shanghai, China.

2.2. Preparation of GNPs and GNP membranes

GNPs were prepared according to the method reported in [14]. As-received GIC particles were subjected to a thermal shock on rapid exposure to 1000°C for 20 s in a muffle furnace, causing GIC particles expanded up to ~440 times their initial volume with the separation of graphene sheets along the *c* axis of graphene layers since trapped intercalants within GIC layers decomposed or vapored instantly, and thereby expanded graphite (EG) formed.

EG particles were then dispersed in absolute ethanol and broken down by a 30 min high speed shear mixing (2400 r/min) followed by a 12 h ultrasonic irradiation (100 W, 80 kHz) at room temperature, consequently EG particles were effectively fragmented into GNPs. The GNP dispersion was filtered and the obtained GNPs were dried at 110°C to remove residue solvents, finally as-prepared GNPs were kept in a dry desiccator for testing and further use.

As-prepared GNPs (~6 mg) were compressed into disk-like membranes (ø6 × 0.2 mm^3) for measuring the electrical conductivity of as-prepared GNPs.

2.3. Preparation of BC-based composite membranes

Preparation of BC-based composite membranes involved (a) making GNP- or MWCNT-absolute ethanol solutions at 0.05 wt% concentration, (b) adding no surfactant or surfactant (NaDDBS or A1100, at 0.3 wt% concentration) to the solutions, (c) dispersing nanofillers (GNPs or MWCNTs) uniformly in the solutions by ultrasonic irradiation (100 W, 80 kHz) for 2 h at room temperature, (d) immersing absolute ethanol-swollen BC membranes in the resulting even GNP- or MWCNT-absolute ethanol suspensions (note that one membrane in one suspension), (e) keeping the suspensions still for 6, 12, or 24 h, or sonicating the suspensions for 3, 6, 9, 12 or 15h at room temperature, (f) withdrawing, rinsing each membrane thoroughly in absolute ethanol to remove the residual surfactants and unadsorbed GNPs or MWCNTs, and then (g) air-drying at room temperature.

2.4. Characterization

Morphological study was carried out using scanning electron microscopy (SEM, JSM-6380LV, JEOL Co., Japan) and two types of field emission SEMs (FESEMs), i.e. LEO1550 (LEO Electron Microscopy Ltd., UK) and Quanta 3D FEG (FEI Co., USA), after the samples were pre-coated with a thin platinum layer. The aspect ratio of GNPs was calculated based on the measured dimensions of 100 GNPs from several FESEM images.

FTIR spectrum was recorded by two types of spectrophotometer, i.e. Thermo Nicolet IS-10 Smart ITR spectrophotometer (Thermo Fisher Scientific Co., Ltd, USA) and Perkin-Elmer Frontier (Perkin Elmer Co., Japan).

The electrical conductivity of as-prepared GNP membranes and BC-based composite membranes was measured using a four-probe with a picoammeter containing an internal voltage source (2611A system, Keithley, USA.) and an impedance measuring meter (HP4284A, HP, USA.). The thickness of membranes was precisely measured for calculating the electrical conductivity. For each measurement, three samples were tested three times at different positions on the BC composite membrane or GNP membrane surface, and then the average was reported.

The amount of GNPs or MWCNTs that were introduced into each BC membrane was determined by the difference between original mass and residual mass of GNPs or MWCNTs in each absolute ethanol solution.

3. Results and discussion

EG particle, as shown in Figure 3a, exhibits a worm-like shape with multiple platelet layers held together at the edge (seen in Figure 3b).

As shown in Figure 4, EG worms were completely torn into GNPs of 3–30 µm in diameter and 20–80 nm in thickness. GNPs are flat and smooth flakes with sharp corners. Image analysis calculation based on 100 GNPs resulted in an average diameter of ~21 µm and thickness of ~47 nm, thereby an aspect ratio of ~447.

Figure 2a presents the FTIR spectrum of as-prepared GNPs. Characteristic vibrational bands of the

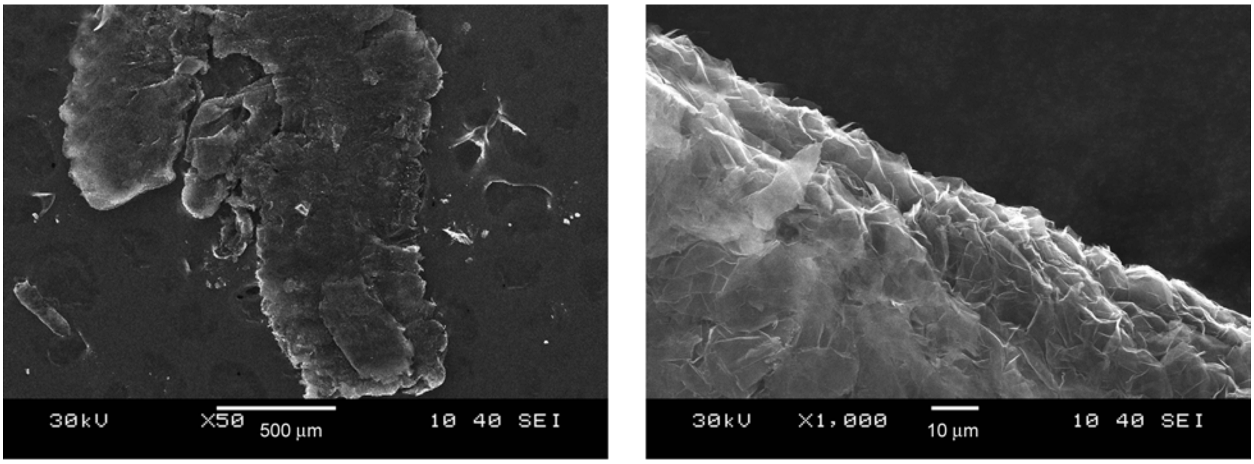

a)

b)

Figure 3. SEM micrographs of an EG particle (a) 50×, (b) 1000×

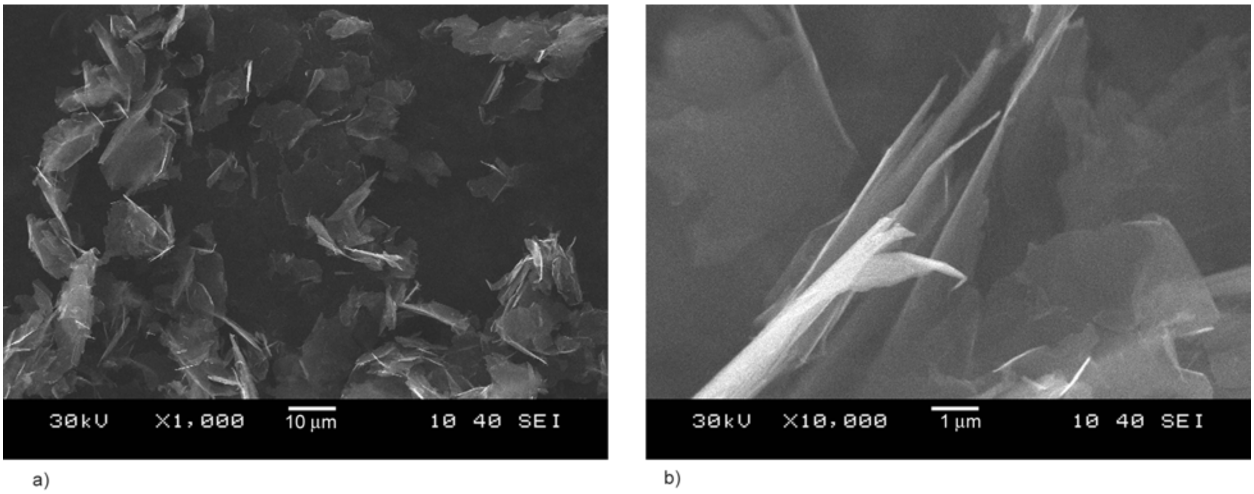

Figure 4. SEM micrographs of GNPs (a) 1000×, (b) 10 000×

functional groups are shown in the spectrum. The most characteristic feature is the broad, intense band at 3650–3050 cm^{-1}, suggesting that many hydroxyl groups (–OH) exist on the surface of as-prepared GNPs. Furthermore, the presence of carboxyl functional groups (C=O) can also be detected. These evidences indicate that during the fabrication of GNPs, treatment of natural graphite with sulfuric acid and thermal shock of GIC particles resulted in some carbon double bonds oxidized, leading to the presence of oxygen-containing functional groups on the GNP flakes, and thereby facilitating the GNP flakes' chemical interactions with surfactant or BC membrane. On the other hand, it is known that oxygen-containing functionalities destroy the aromatic graphene networks and the carbon atom is transformed from a planar sp^2-hybridized geometry to a distorted sp^3-hybridized geometry, which will be deleterious to the electrical properties of graphite. However, in this work the as-prepared GNPs still exhibited an excellent electrical conductivity, 3.3×10^2 S/cm in basal plane at room temperature, even though it is a value decreased by almost two orders of magnitude in comparison to bulk graphite (~10^4 S/cm [15]).

Nanomaterials, including GNPs and MWCNTs, tend to aggregate due to van der Waals attraction and exist in the form of bundles. It is important to separate GNP or MWCNT bundles individually and stabilize them against van der Waals attraction before inserting into BC membranes for employing the inherent properties of individual nanomaterial as well as facilitating their insertion into the porous BC nanofibril network. A well-dispersed MWCNT suspension was previously achieved by using surfactant NaDDBS [6], and NaDDBS is demonstrated to be more desirable than CTAB as the surfactant for MWCNTs based on the fact that under identical preparation conditions, the electrical conductivity of MWCNT/BC composite membranes obtained by dipping BC membranes in the NaDDBS-stabilized MWCNT suspension is higher than that of MWCNT/BC composite membranes obtained from CTAB-stabilized MWCNT suspension [5, 6]. Therefore, in this work NaDDBS was used as a reference surfactant. Furthermore, the fabrication process of BC-based composite membranes, both GNP/BC composite membranes and MWCNT/BC composite membranes, was fundamentally similar to the process used in the previous study [5, 6] except for the used surfactant and solvent, specifically, in this study A1100 was also chosen as a reference surfactant for comparison and the solvent used is volatile absolute ethanol instead of water.

Generally, nanomaterials are sonicated in the solution of surfactant to facilitate their dispersion. As the concentration of surfactant is too low or too high, large and dense nanomaterial clusters form in the solution even after sonication, but at the optimum surfactant concentration, homogeneous dispersion forms a single phase. A favorable concentration of NaDDBS was reported to be ~0.3 wt% in the case of 0.05 wt% MWCNT dispersion [6]. Thus, in this work, 0.3 wt% of surfactant (NaDDBS or A1100) was studied for the 0.05 wt% GNP or MWCNT solution for comparison.

A comparison of photographs in Figure 5 indicates that in the case of 0.05 wt% GNP-absolute ethanol solution, the solution with 0.3 wt% of surfactant NaDDBS, seen in Figure 5b, has the poorest dis-

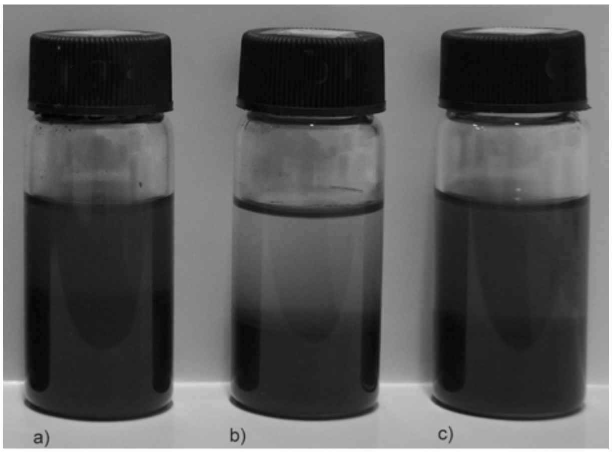

Figure 5. Photographs of 0.05 wt% GNP-absolute ethanol solution with (a) no surfactant, (b) 0.3 wt% of surfactant NaDDBS, and (c) 0.3 wt% of surfactant A1100; 24 h after sonication

persing stability. Interestingly, the solution without surfactant, as is evident in Figure 5a, has the best dispersing stability, performing relatively a little better than that of solution with 0.3 wt% of surfactant A1100 (Figure 5c). Several literatures have stated that homogeneous colloidal graphene suspensions in aqueous and various organic solvents such as ethanol can be created by simple sonication [16–18], and in this work GNP suspension in absolute ethanol solvent with 24 hour stability was indeed achieved only by sonication without the assistance of surfactants, which avoids the negative effects of surfactants since chemical modification are known to be detrimental to the inherent properties, such as electrical conductivity, of conductive fillers [6], and also makes this technique more easy, economical, and thereby particularly appealing for the industrial practices.

At present, the mechanisms that allow the stable dispersion of graphenes in the organic solvents, such as ethanol, are not clear. Notably, a necessary, but not sufficient, condition seems to be that the solvent molecules be considerably polar [18]. As mentioned above, the as-prepared GNPs in this work were heavily decorated with polar oxygen-containing functionalities, i.e. hydroxyl and carboxyl, which is therefore believed to promote the interaction between GNPs and polar organic solvent ethanol and thereby a good dispersion state of GNPs in ethanol solution. Furthermore, it's a similar case for the surfactant A1100 (molecular formula: $H_2N(CH_2)_3Si(OC_2H_5)_3$) which also has polar groups. The agent, ethanol or A1100, adsorbs onto the surface of GNPs through the so-called 'anchoring groups', i.e. hydroxyl groups of ethanol or amine groups of A1100, by van der Waals force or hydrogen bond, while the remainder of the agent (agent chain) extends to the medium to supply steric repulsion for the stabilization of separated GNPs, and it is obvious that when it comes to 0.05 wt% GNP-absolute ethanol solution, the repulsion offered by ethanol is optimum, but the additional adsorbed surfactant A1100 molecules on the GNP flakes' surface will, on the contrary, add the precipitation burden of GNP flakes and thereby be detrimental to the stabilization of separated GNP flakes. The effect of surfactant NaDDBS on the GNP flakes' dispersing stability will be discussed below.

The as-received MWCNTs utilized in this work were also decorated with polar oxygen-containing functionality, i.e. hydroxyl, which was supposed to also promote a good MWCNT-ethanol interaction and thereby a good dispersion state of MWCNTs in ethanol solution. However, as shown in Figure 6, in the case of 0.05 wt % MWCNT solution, the steric repulsion provided by organic solvent ethanol only is not strong enough to prevent the reflocculation due to the stronger intertube van der Waals force of MWCNTs than that of GNPs, and solution without the assistance of surfactant, as shown in Figure 6a, yielded larger amount of precipitate compared with the solution with 0.3 wt% of surfactant A1100. More significantly, surfactant A1100 performed quite well and acted more effectively than surfactant NaDDBS, resulting in a homogeneous black solution with neither sedimentation nor aggregation of MWCNT bundles observed. Consequently, as far as 0.05 wt% MWCNT-absolute ethanol solution is

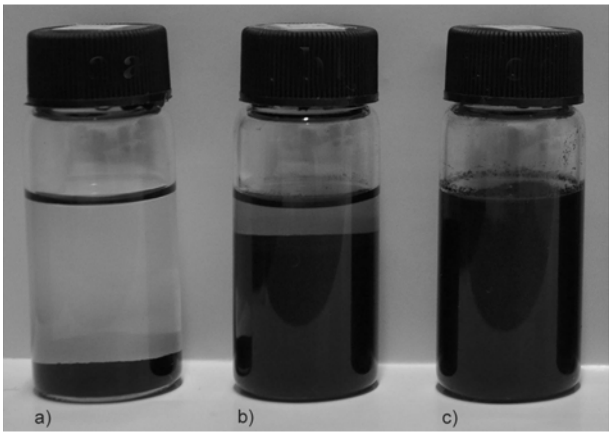

Figure 6. Photographs of 0.05 wt% MWCNT-absolute ethanol solution with (a) no surfactant, (b) 0.3 wt% of surfactant NaDDBS, and (c) 0.3 wt% of surfactant A1100; 24 h after sonication

concerned, its stability follows the sequence: solution without surfactant < solution with 0.3 wt% of surfactant NaDDBS < solution with 0.3 wt% of surfactant A1100.

NaDDBS (molecular formula: $C_{12}H_{25}C_6H_4SO_3Na$), consisting of a benzene ring moiety, an alkyl chain, and a charged group, is a commonly used dispersant for CNTs. Chemical formula of NaDDBS and a suggested schematic of its interaction with a SWCNT can be seen in [19]. It is believed that surfactant NaDDBS form hemimicelles on the CNT surface, and the dispersing capability of NaDDBS to CNT solution can be explained in terms of CNT-NaDDBS interactions, alkyl chain length and headgroup (SO_3^-) size. The benzene rings of NaDDBS molecules provide strong CNT-NaDDBS interactions and the π-like stacking of benzene rings onto the surface of CNTs is believed to increase the binding and surface coverage of surfactant molecules to CNTs significantly. When adsorbing onto the CNT surface, it is probably energetically favorable for the alkyl chains to lie flat along the length of tubes rather than to bend around the circumference. CNT stability depends particularly on those surfactant molecules that lie along the tube surface, parallel to the tube central axis, since the electrostatic repulsion of SO_3^- leads to the charge stabilization of tubes by screened Coulomb interactions [19]. Therefore, we suppose that in this work the different effects, i.e. NaDDBS exhibiting positive effect on the stabilization of MWCNTs whereas little effect on the stabilization of GNPs, arise from different packing density. The larger dimensional size of 2-D GNPs offer more difficulty to achieve high surface packing density of surfactant NaDDBS, resulting in screened Coulomb interactions not enough to stabilize GNPs against van der Waals attraction. However, previous knowledge of the dispersion behavior of CNTs or GNPs in organic solvents or surfactants can not provide much more insight into this question because the solvent or surfactant characteristics required to disperse CNTs or GNPs efficiently have not yet been well established. Clarifying the dispersion behavior of GNPs will necessitate further in-depth investigations.

Thus far, as the result of evaluating the competing stabilization characteristics, a stable 0.05 wt% GNP-absolute ethanol suspension (with no surfactant), as well as a stable 0.05 wt% MWCNT-absolute ethanol suspension with the assistance of 0.3 wt% of surfactant A1100, was chosen as the base suspension for the following study. Then gelatinous absolute ethanol-swollen pristine BC membranes were immersed or sonicated in the base suspensions (note that one membrane in one suspension), consequently, the white pristine membranes (Figure 7a) turned into black composite membranes(Figure 7b) and there are no obvious appearance difference between the obtained GNP/BC composite membranes and MWCNT/BC composite membranes.

Figure 8a presents the surface morphology of GNP-incorporated BC membrane with the surface morphology of MWCNT-incorporated BC membrane also shown in Figure 8b. After air-dried at room

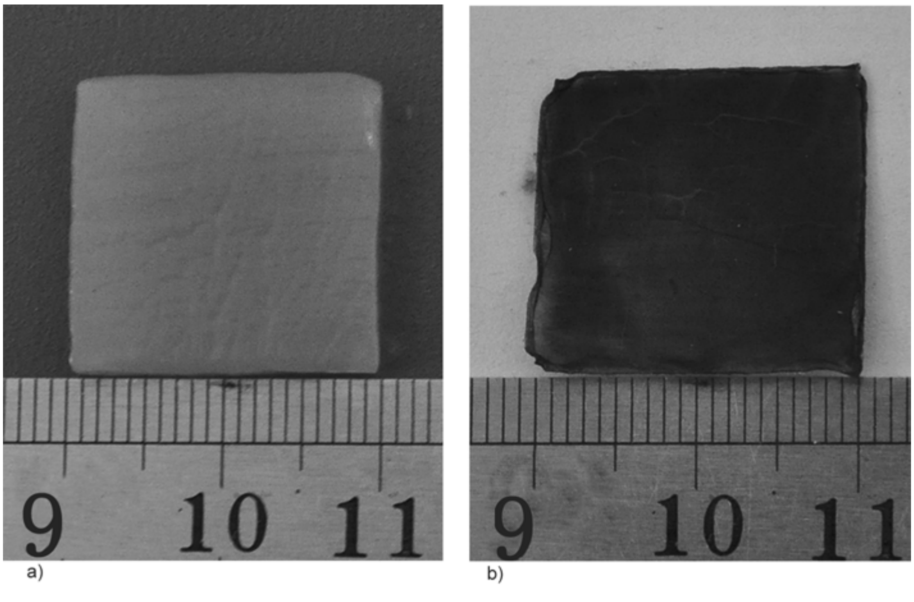

Figure 7. Photographs of (a) absolute ethanol-swollen BC membrane and (b) air-dried GNP/BC composite membrane; sonication for 9 h

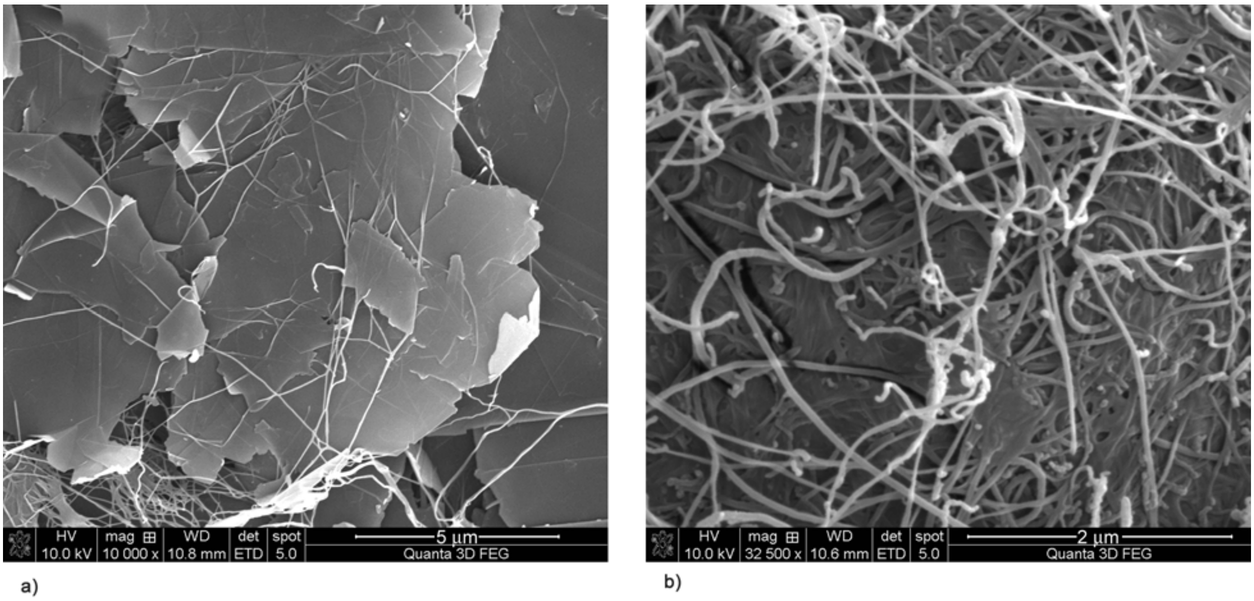

Figure 8. FESEM micrographs of the surface of (a) GNP-incorporated BC membrane and (b) MWCNT-incorporated BC membrane; sonication for 9 h

temperature, the porous structure of BC membranes collapsed into a dense structure with incorporated GNP or MWCNT particles relatively loose-structured over the membrane surface. The diameter of GNPs further decreased to be less than 15 µm after the additional 9 h sonication treatment during the preparation of BC-based composite membranes.

Both flake-shaped GNPs and rod-shaped MWCNTs were seen effectively inserting in the surface layer of BC membranes. Flake-shaped GNPs, weaving through the surface layer of weblike cellulose nanofibrils, were indeed fixed or trapped by adjacent nanofibrils in the BC surface network. Meanwhile, rod-shaped MWCNTs were inserted into BC membranes with each remainder part of MWCNTs spreading on the membrane surface, or entangling with other MWCNTs or cellulose nanofibrils. Furthermore, GNPs exhibited larger surface coverage in the surface layer of BC membrane due to their nearly fully extended 2-D morphology and thereby were supposed to provide more electrical conductivity reinforcement than 1-D MWCNTs.

The cross section of GNP- or MWCNT-incorporated BC membranes were also examined by FESEM after fractured in liquid nitrogen. Figure 9 shows that ultrafine BC ribbons form a dense reticulated ‘layer by layer’ structure, and the thickness of GNPs further decreased to be less than 50 nm after the additional 9 h sonication treatment during the preparation of BC-based composite membranes. Two different domains could be distinguished in Figure 9, a continuous network of cellulose nanofibrils and several inserted GNPs or MWCNTs shown by arrows. More importantly, Figure 9 also gives a direct proof that BC membrane acted as a template or a supporting framework, flake-shaped GNPs weaved through the surface layer of BC membrane and covered over it, while rod-shaped MWCNTs homogeneously inserted into the BC membrane, maintaining their dispersity without aggregation, through the pore structures and tunnels within the cellulose membrane.

Figure 10 presents the time dependence of the electrical conductivity of BC membranes incorporated with GNP or MWCNT particles. The electrical conductivity of these BC composite membranes increases with the increasing immersion or sonication time, indicating that more GNP or MWCNT particles would be incorporated in the membranes after longer immersion or sonication time. Before the capacity limitation of BC membrane is reached, longer immersion time, generally, means more opportunity for the particles to be incorporated. Moreover, the micro-currents of sonication fluid, shear forces and oscillating cavitation bubbles induced by the high acoustic intensity of ultrasound bath may remarkably facilitate GNP flake’s or MWCNT rod’s insertion and entanglement into BC membranes, thus more particles would be incorporated with longer sonication time.

It is well known that BC is stabilized by extensive hydrogen bonding, and there are a mass of hydroxyl

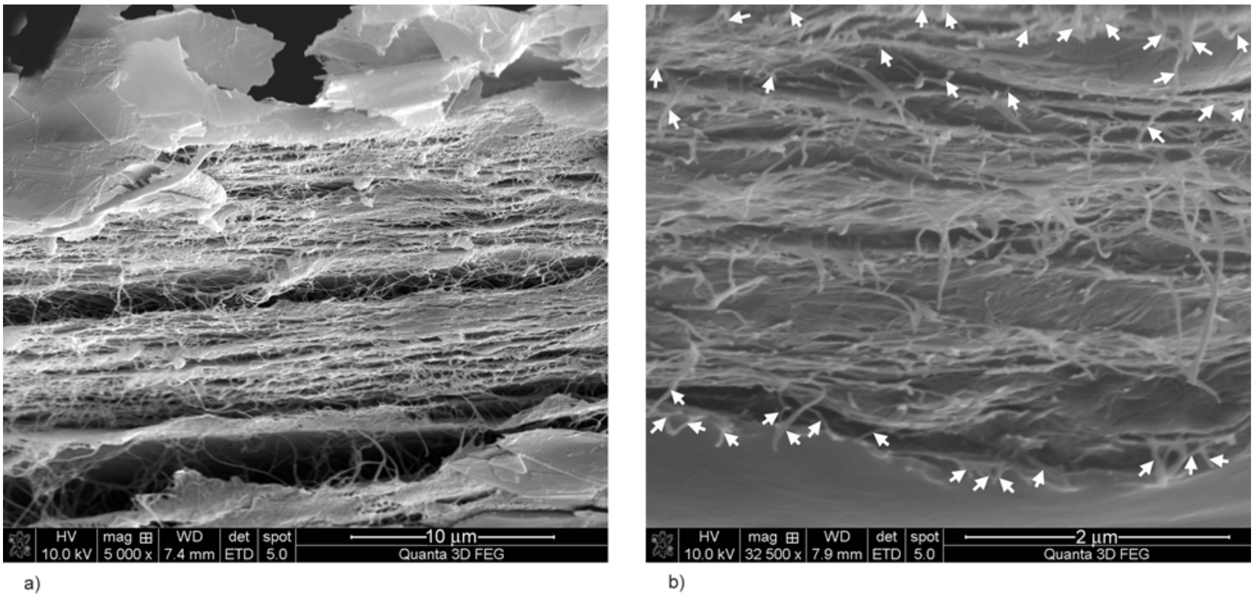

Figure 9. FESEM micrographs of the cross section of (a) GNP-incorporated BC membrane and (b) MWCNT-incorporated BC membrane, arrows show MWCNTs; sonication for 9 h

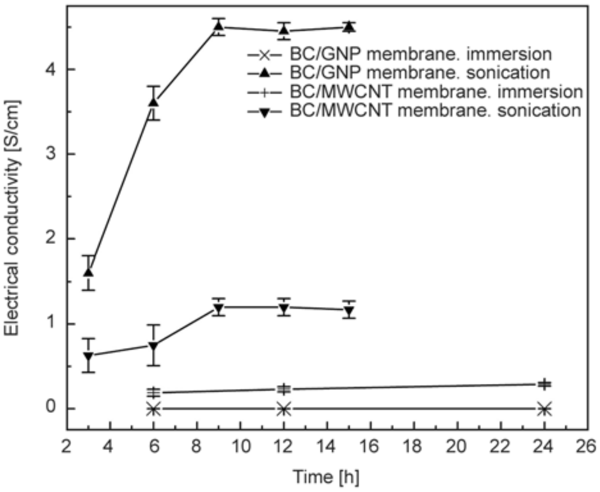

Figure 10. Electrical conductivity of GNP/BC or MWCNT/BC composite membranes at room temperature. Lines are given only for showing the tendency.

groups in the BC membrane (Figure 2b). In this work, as shown in Figure 2, GNP or MWCNT particles, on the surface of which many hydroxyl groups were detected by FTIR, are therefore supposed to be covalently attached by etherification with the cellulose nanofibrils. But it is hard to confirm this strong interaction, i.e. ether linkage, exists between the cellulose nanofibrils and the particles of GNP or MWCNT by FTIR since massive ether linkages already exist among the cellulose nanofibrils. However, in this work, sonication-prepared BC composite membranes were found exhibiting more considerable increase of electrical conductivity than immersion-prepared ones, which not only proved that sonication method is more useful than immersion method in remarkably facilitating GNP flake's or MWCNT rod's insertion and entanglement into BC membranes but also provided a direct evidence that strong physical and chemical interaction, i.e. chemical ether linkage and physical tangling between the BC nanofibrils and the particles of GNP or MWCNT, exists even after 15 h sonication.

As shown in Figure 10, the electrical conductivity of sonication-prepared GNP/BC composite membranes increased from 1.6 to 4.5 S/cm while that of sonication-prepared MWCNT/BC composite membranes increased from 6.3×10^{-1} to 1.2 S/cm, then there is no obvious increase of electrical conductivity of BC composite membranes as the sonication time sequentially increased from 9 to 15 h, which can be attributed to the capacity limitation of BC membranes for the incorporated GNP or MWCNT particles. The deviation of data in Figure 10 is within an acceptable degree considering the small error bar for the maximum data points, demonstrating that GNP or MWCNT particles were really incorporated uniformly and densely in the BC membranes since it is known that homogeneous dispersion and high amount of conductive particles in matrix are the two most important requirements for composites to achieve a uniform and high electrical conductivity.

It is well known that the electrical conductivity of BC composite membranes depends on the amount of electrical pathways formed by conducting GNP or MWCNT particles incorporated in the BC nanofibril network. GNPs have advantage in forming conducting pathways due to their 2-D morphology and thus supposedly allow the electrical conductivity of composite membranes to be enhanced to a greater extent than other spherical or rod-like conducting particles. An attempt was made to determine the amount of GNP or MWCNT particles incorporated in the BC membranes using Thermogravimetric Analysis under a nitrogen atmosphere, but this measurement was unsuccessful and the cause was proved to be in accord with the explanation previously reported [5], i.e. the BC membrane charred after burning up to about 600°C and did not decompose completely. However, in this work the amount of GNP or MWCNT particles that were introduced into each BC membrane was successfully decided by the difference between original mass and residual mass of GNP or MWCNT particles in each absolute ethanol solution. GNP/BC composite membrane with the maximum electrical conductivity 4.5 S/cm was found to contain 8.7 wt% GNPs, while MWCNT/BC composite membrane with the maximum electrical conductivity 1.2 S/cm, which surpasses the maximum electrical conductivity 1.4×10^{-1} S/cm of immersion-prepared BC composite membrane incorporated with 9.6 wt% MWCNTs reported by elemental analysis in Ref. [5], was found to be incorporated by 13.9 wt% MWCNTs. Therefore, compared with 1-D MWCNTs, as long as GNPs inserted into BC membranes, the 2-D reinforcement of GNPs was proven to be more effective in improving the electrical conductivity of BC membranes thus not only break the bottleneck of further improving the electrical conductivity of BC-based composite membranes but also broaden the applications of BC and GNPs.

4. Conclusions

In this study, BC-based composite membranes were prepared by immersing or sonicating gelatinous absolute ethanol-swollen pristine BC membranes in stable 0.05 wt% GNP-absolute ethanol suspensions or 0.05 wt% MWCNT-absolute ethanol suspensions stabilized with the assistance of 0.3 wt% of A1100.

By physical and chemical methods, flake-shaped GNPs, weaving through the surface layer of web-like cellulose nanofibrils, were indeed fixed or trapped by the adjacent nanofibrils in the BC surface network, while rod-shaped MWCNTs were homogeneously inserted into the BC membrane through pore structures and tunnels within the BC membrane.

Sonication-prepared BC composite membranes exhibit more considerable increase of electrical conductivity than immersion-prepared ones, which not only proved that sonication is a more useful method than immersion to remarkably facilitate GNP flake's or MWCNT rod's insertion into BC membranes but also provided a direct evidence that strong interaction, i.e. chemical ether linkage and physical tangling between the BC nanofibrils and the particles of GNP or MWCNT, exists even after 15 h sonication in absolute ethanol.

Furthermore, compared with 1-D MWCNTs, as long as GNPs inserted into BC membranes, the 2-D reinforcement of GNPs was proved more effectively in improving the electrical conductivity of pristine BC membranes. BC membrane with 8.7 wt% incorporated GNPs reached the maximum electrical conductivity of 4.5 S/cm, while MWCNT/BC composite membrane containing 13.9 wt% MWCNTs achieved the maximum electrical conductivity of 1.2 S/cm, thus not only break the bottleneck of further improving the electrical conductivity of BC-based composite membranes but also broaden the applications of BC and GNPs.

Acknowledgements

The authors are grateful for the financial support of National Natural Science Foundation of China (No. 51002077, No. 51203074), Fundamental Research Funds for the Central Universities (No. NUST 2011YBXM163), Jiangsu Overseas Research & Training Program for University Prominent Young & Middle-aged Teachers and Presidents, and Special Foundation for 'first-grade Zijin's Star' of 'Excellence initiative' Project of Nanjing University of Science and Technology (No.AB41339).

References

[1] Chen P., Cho S. Y., Jin H-J.: Modification and applications of bacterial celluloses in polymer science. Macromolecular Research, **18**, 309–320 (2010). DOI: 10.1007/s13233-010-0404-5

[2] Siró I., Plackett D.: Microfibrillated cellulose and new nanocomposite materials: A review. Cellulose, **17**, 459–494 (2010). DOI: 10.1007/s10570-010-9405-y

[3] Ifuku S., Nogi M., Abe K., Handa K., Nakatsubo F., Yano H.: Surface modification of bacterial cellulose nanofibers for property enhancement of optically transparent composites: Dependence on acetyl-group DS. Biomacromolecules, **8**, 1973–1978 (2007). DOI: 10.1021/bm070113b

[4] Yano H., Sugiyama J., Nakagaito A. N., Nogi M., Matsuura T., Hikita M., Handa K.: Optically transparent composites reinforced with networks of bacterial nanofibers. Advanced Materials, **17**, 153–155 (2005).
DOI: 10.1002/adma.200400597

[5] Yoon S. H., Jin H-J., Kook M-C., Pyun Y. R.: Electrically conductive bacterial cellulose by incorporation of carbon nanotubes. Biomacromolecules, **7**, 1280–1284 (2006).
DOI: 10.1021/bm050597g

[6] Yoon S. H., Kang M., Park W-I., Jin H-J.: Electrically conductive polymeric membranes by incorporation of carbon nanotubes. Molecular Crystals and Liquid Crystals, **464**, 685–690 (2007).
DOI: 10.1080/15421400601030449

[7] Jung R., Kim H-S., Kim Y., Kwon S-M., Lee H. S., Jin H-J.: Electrically conductive transparent papers using multiwalled carbon nanotubes. Journal of Polymer Science Part B: Polymer Physics, **46**, 1235–1242 (2008).
DOI: 10.1002/polb.21457

[8] Kim Y., Kim H-S., Bak H., Yun Y. S., Cho S. Y., Jin H-J.: Transparent conducting films based on nanofibrous polymeric membranes and single-walled carbon nanotubes. Journal of Applied Polymer Science, **114**, 2864–2872 (2009).
DOI: 10.1002/app.30829

[9] Kim Y., Kim H-S., Yun Y. S., Bak H., Jin H-J.: Ag-doped multiwalled carbon nanotube/polymer composite electrodes. Journal of Nanoscience and Nanotechnology, **10**, 3571–3575 (2010).
DOI: 10.1166/jnn.2010.2232

[10] Yun Y. S., Bak H., Jin H-J.: Porous carbon nanotube electrodes supported by natural polymeric membranes for PEMFC. Synthetic Metals, **160**, 561–565 (2010).
DOI: 10.1016/j.synthmet.2009.12.003

[11] Feng Y., Zhang X., Shen Y., Yoshino K., Feng W.: A mechanically strong, flexible and conductive film based on bacterial cellulose/graphene nanocomposite. Carbohydrate Polymers, **87**, 644–649 (2011).
DOI: 10.1016/j.carbpol.2011.08.039

[12] Yan J., Wei T., Shao B., Ma F., Fan Z., Zhang M., Zheng C., Shang Y., Qian W., Wei F.: Electrochemical properties of graphene nanosheet/carbon black composites as electrodes for supercapacitors. Carbon, **48**, 1731–1737 (2010).
DOI: 10.1016/j.carbon.2010.01.014

[13] Zhou T., Wang X., Liu X., Xiong D.: Influence of multi-walled carbon nanotubes on the cure behavior of epoxy-imidazole system. Carbon, **47**, 1112–1118 (2009).
DOI: 10.1016/j.carbon.2008.12.039

[14] Chen G., Weng W., Wu D., Wu C., Lu J., Wang P., Chen X.: Preparation and characterization of graphite nanosheets from ultrasonic powdering technique. Carbon, **42**, 753–759 (2004).
DOI: 10.1016/j.carbon.2003.12.074

[15] Li J., Sham M. L., Kim J-K., Marom G.: Morphology and properties of UV/ozone treated graphite nanoplatelet/epoxy nanocomposites. Composites Science and Technology, **67**, 296–305 (2007).
DOI: 10.1016/j.compscitech.2006.08.009

[16] Potts J. R., Dreyer D. R., Bielawski C. W., Ruoff R. S.: Graphene-based polymer nanocomposites. Polymer, **52**, 5–25 (2011).
DOI: 10.1016/j.polymer.2010.11.042

[17] Park S., Ruoff R. S.: Chemical methods for the production of graphenes. Nature Nanotechnology, **4**, 217–224 (2009).
DOI: 10.1038/nnano.2009.58

[18] Paredes J. I., Villar-Rodil S., Martínez-Alonso A., Tascón J. M. D.: Graphene oxide dispersions in organic solvents. Langmuir, **24**, 10560–10564 (2008).
DOI: 10.1021/la801744a

[19] Islam M. F., Rojas E., Bergey D. M., Johnson A. T., Yodh A. G.: High weight fraction surfactant solubilization of single-wall carbon nanotubes in water. Nano Letters, **3**, 269–273 (2003).
DOI: 10.1021/nl025924u

eXPRESS Polymer Letters Vol.7, No.7 (2013) 767–777
Available online at www.expresspolymlett.com
DOI: 10.3144/expresspolymlett.2013.74

Processing and characterization of poly(lactic acid) based bioactive composites for biomedical scaffold application

J. Goswami[1*], *N. Bhatnagar*[2], *S. Mohanty*[3], *A. K. Ghosh*[1]

[1]Centre for Polymer Science & Engineering, Indian Institute of Technology Delhi 110016 New Delhi, India
[2]Mechanical Engineering Department, Indian Institute of Technology Delhi 110016 New Delhi, India
[3]Stem Cell Facility, All India Institute of Medical Sciences 110029 New Delhi, India

Received 8 April 2013; accepted in revised form 1 June 2013

Abstract. The current study focuses on three-components material systems (poly(lactic acid) (PLA), poly(ε-caprolactone) (PCL) and wollastonite (W)) in view of possible application a biomedical scaffold constructs. Melt extruded PLA/PCL/W composites (PLCL15, PLCLW1, PLCLW4, PLCLW8 containing 0, 1, 4, 8 phr filler respectively) are batch foamed using compressed CO_2 and the porous foams are studied for *in vitro* biocompatibility by seeding osteoblast cells. SEM images of the unfoamed polymers show immiscibility in all compositions. Materials have been tested under compressive load using dry and wet conditions (using phosphate buffered saline at pH 7.4) for *in vitro* study. Contact angle measurement shows enhanced hydrophilicity in the composites changing from 80° in PLCL15 to 72° in PLCLW8. The foams are found to be microcellular (5–8 µm) in morphology showing quite uniform pore distribution in the composites. The prepared foams, when studied as scaffold constructs, show osteoblast cell attachment and proliferation over the incubation period of 7 days. As expected, PLCLW8 containing highest amount of $CaSiO_3$ supported maximum cell growth on its surface as visible from MTT assay data and SEM scans.

Keywords: *biopolymers, composites, hydrophilicity, foams, cell viability*

1. Introduction

The use of polymers for biomedical applications is an emerging field gaining maximum attention from researchers across the world due to their advantages as given below;

- Mitigating the need for second surgery for want of autogeneous bone grafts,
- Formation of load bearing bones without any stress shielding effect and
- Degradation of the scaffold with time into non-toxic byproducts as the osteoblasts grow into bone tissues.

These are some of the deciding factors for polymeric clinical devices as against allografting, autografting and xenografting. The selection of the polymers to be used as biomedical implant needs to be done carefully, based on the following criteria [1, 2]:

- The compositional resemblance and comparable mechanical properties of the polymer with the host tissue,
- Processability and fabricability with defined reproducibility along with sterilizability and
- Modulation of degradation profile of the polymer as per the requirement of the intended application.

The design of the biomaterial with requisite characteristics depends exclusively on the properties of the host tissue. The soft and hard tissues vary extensively in their intrinsic material properties and the mechanical properties of these tissues are listed in Table 1.

---

[*]Corresponding author, e-mail: jutikagoswami@gmail.com

Table 1. Biomechanical properties of human body tissues [1, 2]

Type of tissue	Young's modulus [MPa]	Tensile strength [MPa]	Strain at break [%]	Density [g/cc]	Composition
Soft tissue (articular cartilage)	10.5	27.5	–	–	–
Hard tissue (cortical bone)	$(14–20)\cdot10^3$	50–150	1–3	$1.8–2.2^*$	Collagen (20%), hydroxyapatite (calcium phosphate) (60%), others (20%)
Hard tissue (cancellous bone)	$(0.05–0.5)\cdot10^3$	10–20	5–7	0.1–1.0	Same as hard tissue with higher porosity

*apparent density. True density of cortical bone is 18–20 g/cc

Poly(lactic acid) (PLA), termed as 'green biopolymer', is gaining priority over other biopolymers for biomedical applications due to its property relevance to the biological tissues in terms of biodegradability, biocompatibility and its availability from natural resources. PLA has been the first biodegradable polymer to obtain Food and Drug Administration (FDA), USA approval for clinical applications. It has been used as sutures for long, recently as cardio vascular stents and bone graft scaffolds that degrade by both enzymatic and non-enzymatic way into lactic acid under physiological environment [3–9]. But the disadvantage of PLA is its brittleness and lower thermal stability due to which its melt processability has been a great concern [10–12]. Studies have been done to get away with these difficulties by methods like copolymerization, blending with other polymers, and plasticization. Poly(ε-caprolactone) (PCL) is another FDA approved synthetic biodegradable aliphatic polyester that is produced via petrochemical route. It is a lower modulus thermoplastic elastomer with higher toughness at room temperature (glass transition temperature, T_g: (–)60°C) as compared to PLA (T_g: 60°C) [13]. Melt blending of PLA with PCL is expected to improve the processability of PLA as it is thermally more stable.

However, there are limitations of the organic polymeric scaffolds originating with the release of acidic by-products that causes inflammation inside the human body and the lack of adhesion with the bone cells due to differences in their compositional properties [14]. The addition of a bioactive material either osteoinductive or osteoconductive to the polymeric system gives an added advantage of tissue adhesion with the organic phase. Different biomaterials like hydroxyapatite, bioactive glasses, and glass-ceramics having bonelike mineral compositions are being added to the polymers so as to make the tissue regeneration process faster by improving bone bonding *in vivo* [15–17]. It is reported that CaO and SiO_2 are two main bone bonding components for formation of apatite layer at the damaged tissue site [2, 18]. Wollastonite (W), containing CaO–SiO_2, is a highly potential bioactive filler to prepare biodegradable composites for tissue engineering applications, and its potentiality for use in medical devices can be well understood from the overwhelming response of the researchers in recent years [19–21]. This high aspect ratio acicular material can help the implanted organic scaffold to bond with the bone because of the chemical similarity with the bone minerals while maintaining mechanical integrity under physiological environment. Another advantage of using this filler is that the alkaline degradation products of the mineral help in neutralizing acidic by-products of the biopolymers thereby reducing inflammation. Thus polymeric scaffold prepared from composites based on PLA, PCL and W is expected to provide improved mechanical as well as physiological activity by way of initially reinforcing the polymer blend matrix and later as a bioinitiator.

A polymeric scaffold needs to be a porous network structure with well-defined porosity and morphology. Scaffolds are prepared by different processes such as electrospinning, porogen leaching, solvent casting, foaming using chemical blowing agent (CBA) and physical blowing agents (PBA), rapid prototyping etc. [22–24]. But use of any solvent or CBA may be detrimental for a scaffold to be used *in vivo* due to traces of contamination. Supercritical carbon-di-oxide ($ScCO_2$) as PBA has been used extensively for this purpose due to its inertness, environmental friendly nature and easy availability [25–27]. The current study involves solid state batch foaming of the PLA/PCL/W composites so as to develop porous scaffolds using compressed CO_2. Compressed CO_2 acts as plasticizer or solvent to a polymer system that reduces glass transition temperature (T_g) causing enhanced self-diffusion of the solvent increasing its solubility further [28]. Interaction of CO_2 and PLA has been established by Fourier transform infrared (FTIR) studies indicating better solubility into this polymer as compared with other physical blowing agents such as N_2 and this improved solubility implies better foamability of the concerned polymer [29, 30].

Diffusion driven nucleation in a heterogeneous system such as PLA/PCL/W is favored as compared to that of a homogeneous one (neat PLA) because the activation energy needed for solvent dissolution is lowered at the interphases. The effect of wetting angle at the interface has been explained in heterogeneous nucleation theory [31]. PCL as immiscible domains and W as inorganic filler, both contribute towards inhomogeneity in the PLA matrix, thereby, enhancing the effect of wetting angle for CO_2 diffusion. *In vitro* bioactivity of wollastonite has already been reported as PLA/W and PCL/W composite systems showing mineralization when studied using simulated body fluid (SBF) [14, 23]. Thus, the presence of wollastonite helps in osteoblast cell growth in similar way like that of hydroxyapatite (HA), the main mineral component in bone tissues [32].

The focus of the present study is to develop PLA/PCL/wollastonite composites as porous constructs and to analyze the scaffolds for bio-suitability by seeding osteoblast cells onto them in an *in vitro* study. The suitability of the material system developed for this purpose depends exclusively on the cell adhesion response and improvement in mechanical properties could be an added advantage.

2. Experimental

2.1. Raw materials

Poly(lactic acid) (ESUN™ A-1001) and Poly(ε-caprolactone) (CAPA-6800) were supplied by Shenzhen BrightChina Industrial Co. Ltd, China and Perstorp Chemicals, UK respectively. The density and melt index (MFI) of PLA were specified as 1.25 (g/cc, 21.5°C) and 10–15 (g/10 min, 190°C, 2.16 kg, ASTM D1238) respectively. The molecular weight and MFI for PCL were 80 000 g/mol and 3 (g/10 min at 160°C, 2.16 kg, ASTM D1238) respectively. Wollastonite (Kemolit K-1010, Wolkem India Limited, Udaipur, India) in the powder form was used as filler in this study.

2.2. Material preparation

The blend composition with PLA/PCL ratio of 85/15, designated as PLCL15, was selected as matrix material for the preparation of the composites based on its optimized property of modulus and toughness (PLCL15 was selected from a series of blend prepared from the same PLA and PCL in a separate preliminary study by the present group). The blend (PLCL15) and composites, PLA/PCL/W (phr) in the ratio of 85/15/01, 85/15/04 and 85/15/08 designated as PLCLW1, PLCLW4 and PLCLW8 respectively, were prepared by melt blending technique using a co-rotating twin-screw extruder (Model: Haake Thermofischer Prism Eurolab 16; *L*/*D*: 40, die diameter: 2.5 mm, screw diameter: 16 mm). All compositions were processed maintaining 160–190°C temperature profile in the extruder and 190°C at the die with a screw speed of 200 rpm. The raw materials were pre-dried at 45°C under vacuum for 12 hours. The strands were granulated and subsequently injection moulded at 190°C (model: L & T, Demag, PFY40-LNC 4P) to prepare 0.75 mm thick sheets for foaming purposes in a in house fabricated injection mold.

2.3. Development of composites as porous scaffold

Solid state batch foaming process was adopted to prepare microporous scaffolds from the injection moulded composite sheets. Cut samples of $4\times4\times0.75\ mm^3$ sizes were used for batch foaming by using compressed CO_2 as the physical blowing agent. A high pressure vessel was used as batch foaming apparatus for saturating the samples with CO_2. This solid state foaming process involved basically three stages – saturation of the samples with a blowing agent to produce a polymer-solvent system, depressurization controlling phase separation developing nucleation sites and bubble growth causing expansion of the nucleated micro-bubbles in the polymer giving a foamed product. Foams in four different batches were produced using saturation pressure of 1, 3, 5 and 8 MPa for seven days. Foaming of the samples was done at 160°C temperature using hot glycerine bath immediately after depressurizing the pressure vessel at the rate of 1.6 MPa/min. The higher foaming temperature favored uninhibited bubble expansion producing cells of desired sizes. Based on the morphological evaluation of the foams of different batches, the foams obtained from 3 MPa pressure batch were optimized for further studying as scaffold by seeding osteoblast cells.

2.4. Scanning electron microscopy (SEM)

Cryofractured (under liquid nitrogen) surfaces of all the compositions in both foamed and unfoamed state were scanned to study phase morphology using a scanning electron microscope (Model: Carl Zeiss EVO 5O SEM, Germany) with accelerating voltage of 20 kV. Samples were gold-sputtered before scanning to dissipate the charges produced in the non-conducting polymers. SEM scans of the porous scaffolds were analyzed for cell size and immiscible PCL domain sizes in the unfoamed polymers were calculated by ImageJ software.

2.5. Transmission electron microscopy (TEM)

The composites were viewed in transmission mode using JEOL JEM-2100F field emission microscope. Samples, which were prepared by microtoming process as 100 nm thick slices from injection moulded composite specimens, were scanned using 200 kV accelerating voltage.

2.6. Compressive test

Mechanical testing under compressive mode was performed in a universal testing machine (INSTRON 5582) using a static load of 100 kN at crosshead speed of 1 mm/min at room temperature. The test was performed transversely with respect to tensile test direction. The rectangular shaped specimens were prepared by machining injection moulded samples ($20\times20\times3$ mm^3). The dimensions of each sample were fed into the Merlin software during the test and compressive modulus and strength were measured for five samples of each composition. Wet compressive test was performed as *in vitro* study, after keeping the samples in phosphate buffered saline (PBS) solution at pH 7.4 under enzymatic condition (enzyme used- lysozyme) for 7 (seven) days in a shaking water bath (Julabo SW23). The samples were then taken out and wiped to remove the excess media before testing. The same testing procedure was followed with the wet samples as well.

2.7. Contact angle measurement

Dynamic contact angle of the polymers were measured in a KRUSS Processor Tensiometer K100 attached with KRUSS Laboratory Desktop K100 Contact Angle software, using injection moulded sheet specimen of size $20\times10\times0.75$ mm^3. Three specimens were tested for advancing and receding dynamic angles which have been averaged and reported in the present work.

2.8. *In vitro* bioactivity study on the prepared scaffolds

2.8.1. Isolation of osteoblast cells

Goat tibia bone was collected from the slaughter house and transported to the laboratory in phosphate buffered saline after getting due permission from the competent authority. Bone was cut into pieces of approximately 2–3 mm and washed with PBS containing antibiotics, 100 U/mL PenSrep (Lonza, Cat no.17-602E), 50 mg/ml Getamicin sulfate (Himedia, Cat No.A010) and 100 mg/ml Amphotericin B (Himedia Cat No.A011). The pieces were incubated for 7 days in Dulbecco's Modified Eagle Medium (DMEM, Cat no. CC3004.05L) on the bottom of a T25 tissue culture dish to let them adhere to the dish surface and the cells to come out of the tissue. These were cultured until sub confluence in a controlled atmosphere of 5% CO_2 and 37°C temperature.

2.8.2. Culture and seeding of the cells on scaffolds

Goat osteoblast cells were then expanded in DMEM media with 10% fetal bovine serum (Biological Industries Cat no.04-121-1A), HEPES (4-(2-hydroxyethyl)-1-piperazineethanesulfonic acid) buffer IM (Lonza, Cat no.BEA-17-737E), 100 U/mL PenSrep, 50 mg/mL Getamicin sulfate and 100 mg/mL Amphotericin B. Cells were trypsinized (Lonza, CC-5012) under sub confluent state and then used for seeding. All the polymer scaffolds were sterilized by autoclaving and pre-wet in complete medium (DMEM) for overnight prior to cell seeding. Each scaffold was seeded with $5\cdot10^4$ counts of cell and MTT assay was done after 3 and 7 days.

2.8.3. MTT assay

MTT assay was used to assess metabolic activity of the osteoblasts on day 3 and day 7. Samples were dipped in 9:1 ratio of DMEM media and MTT ((3-(4, 5-Dimethylthiazol-2-yl)-2, 5-diphenyltetrazolium bromide, Millipore CT0-A, USA) and incubated for 6 hours at 37°C. The media-MTT mixture was then spun to collect insoluble formazan crystals. 1 mL DMSO (dimethyl sulfoxide) was used to dissolve the crystals and absorbance was checked using microplate reader (BIORAD iMark Microplate reader, USA) at 560 nm for 5 replicates. In addition, standard calibration curve was made by MTT assay on directly counted cells and the absorbance values were plotted against the counted cell numbers. Metabolically active cell numbers were then determined using this standard curve based on their MTT absorbance.

2.8.4. Cell-morphology observations

After incubating for 7 days, cell seeded scaffolds were harvested and fixed with 2.5% glutaraldehyde for 4 hours. These were then dehydrated in gradient alcohol before sputter coated with gold for SEM scan.

3. Results and discussion

3.1. Compressive test

Wet compressive test was performed with an aim to mimic the materials' performance under physiological environment. The implant is expected to sustain under this harsh condition while maintaining bonhomie with the host tissue. The compressive strength of the composites could not be measured as per the ASTM D695 standard, because there was no shattering fracture and the samples were just flattened into thinner plate under applied load. The nominal stress changed steadily in two stages during the test as can be seen from Figure 1 and its inset images. Modulus of elasticity was calculated by drawing tangent at the initial linear portion of the plots and extending it to set the zero point on the strain axis, but this modulus value is indicative only, as actual values could not be determined. The results are listed in Table 2. The behavioral difference of the polymers under dry and wet test conditions is not very sig-

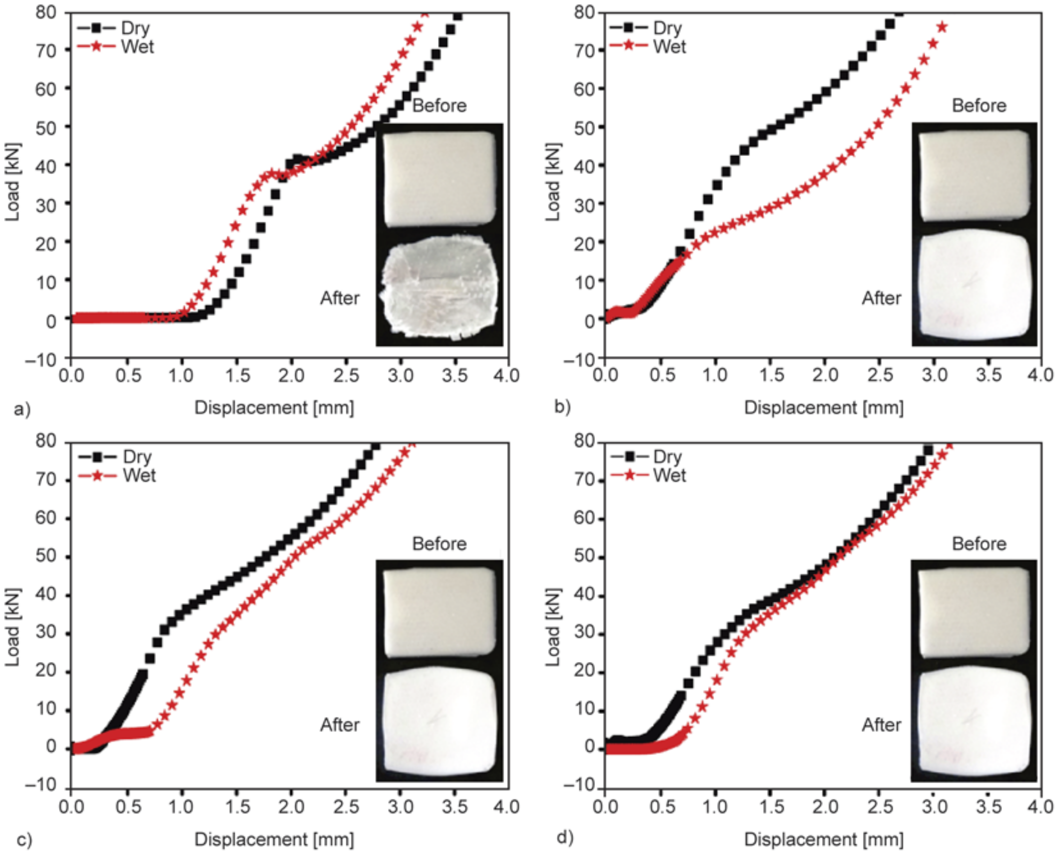

Figure 1. Plots of displacement of polymers under compressive load in both dry and wet conditions for a) PLCL15, b) PLCLW1, c) PLCLW4, and d) PLCLW8. Inset images are those of samples before and after the experiment.

Table 2. Compressive test data under dry and wet conditions

Composition	Dry		Wet	
	Compressive strength [MPa] at ultimate load	Elasticity modulus [MPa]	Compressive strength [MPa] at ultimate load	Elasticity Modulus [MPa]
PLCL15	85.7±1.15 (at yield)	3.298±0.21 (at yield)	81.6±3.22 (at yield)	2.500±0.04 (at yield)
PLCLW1	192.2±0.16	2.755±0.18	191.9±0.17	2.044±0.09
PLCLW4	185.4±0.01	3.141±0.19	185.2±0.01	2.449±0.06
PLCLW8	190.7±0.88	2.397±0.13	189.9±0.25	2.674±0.21

nificant. The blend, PLCL15 got crushed at 100 kN load and produced visible cracks. The blend shows a longer rubbery plateau at constant load value prior to the first linear rise in the plots as compared to those in the composites. It was difficult to ascertain whether the toe region of the plots was due to material property. Microacicular wollastonite helped in improvement of compressive strength of the composites on application of compressive load. Wollastonite got aligned in the flow direction during injection moulding and the machined samples were tested at the lying position. Thus this high modulus inorganic filler resisted breakage by arresting the crack propagation from filler to polymer, thereby increasing compressive strength of the polymeric composites. This reinforcing effect is more visible in PLCLW1 than the other composites (PLCLW4 and PLCLW8) that might be due to filler agglomeration in these. Similar kind of result was reported by Javni *et al*. [33] where micro silica filler improved compressive strength of the polymer at lower loading whereas, reverse occurred at higher loading.

The composites' compressive strength at ultimate load is calculated and as can be seen from Table 2, the property of the composites did not deteriorate much under wet conditions as compared to the blend thereby proving better resistance of the composites towards the surrounding environment.

3.2. Scanning electron microscopy (SEM) of unfoamed composites

Immiscible phase morphology is clearly visible in all compositions in SEM scans of the polymers (Figure 2). The minor phase, PCL remains as globules with distinct phase boundary within the PLA matrix. The immiscible PCL domain sizes in the polymers are calculated by image processing software and this domain size in the blend is bigger than that in the composites as seen from Table 3. Thus, presence of the filler causes reduction in the

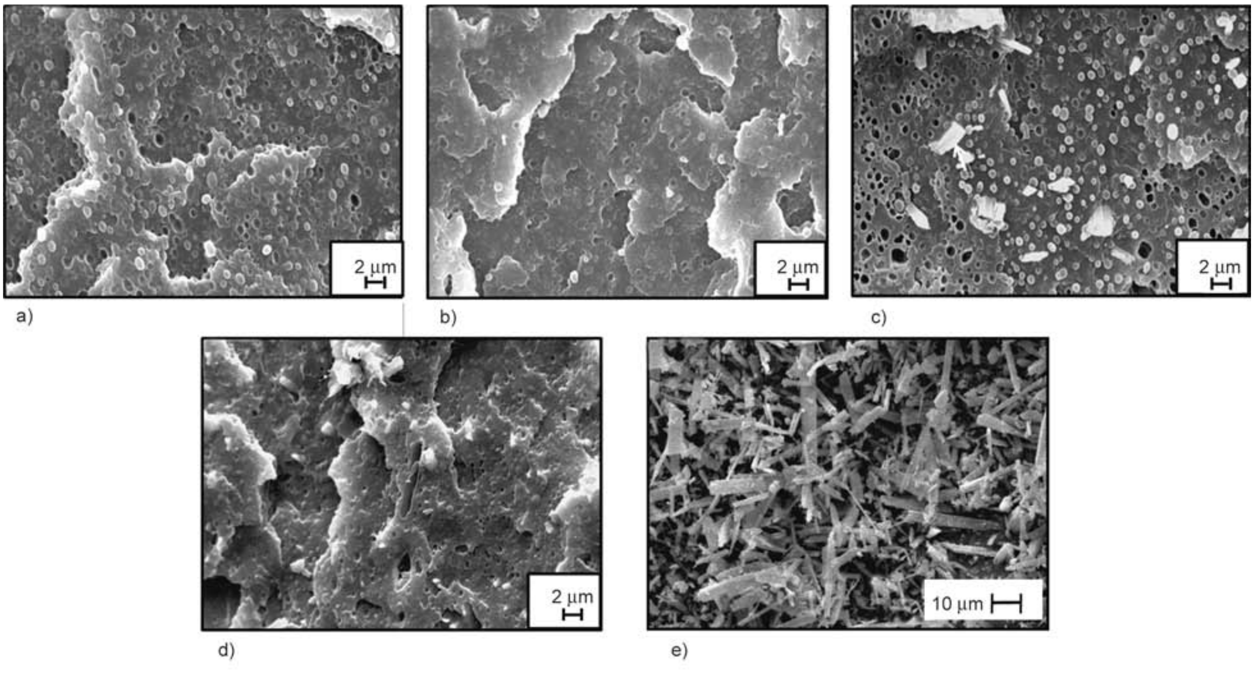

Figure 2. SEM images of cryofractured surfaces of a) PLCL15, b) PLCLW1, c) PLCLW4, d) PLCLW8 and e) acicular W-powder

PCL globule sizes. The PCL domain size reduction in the composites due to the rigid inorganic filler addition may be attributed to changed rheological properties in the polymers as compared to that of the blend. The shearing force experienced by PCL during extrusion process is different in the presence of the filler. It has been reported that the immiscible phase morphology changes in the presence of a filler and it varies with mixing time as well which has been said to be ‘kinetic controlled’ [34].

Wollastonite, the third component of the composites, is partially visible showing mostly its tip with distinct boundaries. Increasing presence of the filler in the polymer can be seen with increasing wollastonite content in Figure 2b, 2c and 2d containing 1, 4 and 8 phr of wollastonite respectively. Dispersion of the filler in the composites is quite uniform, and these are oriented mostly in the flow direction due to which only the tip of the fillers could be seen. Figure 2e shows the needle shaped fillers’ morphology with average length of 14.9 micron and diameter of 3.33 micron as measured using SMART SEM software attached with the SEM microscope.

3.3. Transmission electron microscopy (TEM)

The microtomed slices of the composites were scanned in transmission mode and the images are shown in Figure 3. The individual spherical entities confirm circular cross-section of the filler, and the distribution of the filler in the PLA/PCL matrix system is quite uniform in PLCLW1 and PLCLW4 compositions. But incorporation of higher amount of wollastonite causes agglomeration indicating better prevalence of filler-filler interaction than the polymer-filler system. The visible morphology of the wollastonite in the images re-establishes the fact that these are oriented in the flow direction and the findings of the mechanical tests can be justified.

3.4. Contact angle measurement

Wettability of a material is one of the crucial factors for determining the suitability of its use as biomedical implant. Increasing hydrophilicity of an implant improves polymer-bone adhesion that helps in faster regeneration of damaged tissues *in vivo*. Being hydrophobic, organic polymers usually lack this adhesion that slows down the tissue regeneration process. Wollastonite reduced the contact angle in the composites, thereby indicating enhanced wettability and improved scaffold-body cell attachment. The hydrophilicity is said to be the deciding factor in scaffold degradation and the surface morphology of the scaffold plays a significant role in degradation. The contact angle of wollastonite is reported as 0° and it is established already in other polymers as improving hydrophilicity [35].

Dynamic contact angle measurement shows that PLCLW8, with maximum filler content, has lowest advancing contact angle as shown in Table 3. Similar trend can also been seen in receding contact

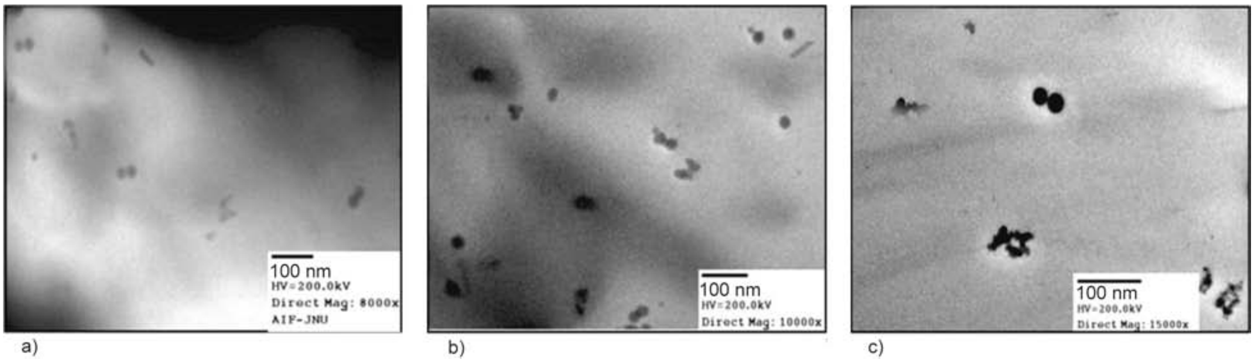

Figure 3. TEM images of the microtomed samples of composites a) PLCLW1, b) PLCLW4 and c) PLCLW8

Table 3. PCL domain size, dynamic contact angle parameters, foam morphological parameters and MTT assay data

Sample	PCL domain size (unfoamed) [µm]	ACA* [deg]	RCA* [deg]	Hysteresis [deg]	Cell diameter [µm]	Cell density [cell/cc]	Number of cell (counts)	
							Day 3	Day 7
PLCL15	1.1±0.30	80.0	57.2	22.8	6.1±1.70	$9.4\cdot10^{12}$	20 000	52 600
PLCLW1	0.8±0.05	77.0	51.7	25.3	5.4±0.82	$11.7\cdot10^{12}$	35 080	76 000
PLCLW4	0.6±0.08	75.2	47.1	28.2	5.5±0.79	$10.9\cdot10^{12}$	33 025	252 634
PLCLW8	0.7±0.09	72.1	44.3	27.7	8.3±0.52	$3.5\cdot10^{12}$	62 000	356 900

*ACA: advancing contact angle, RCA: receding contact angle

angle values that indicate de-wettability of the materials. The hysteresis indicates the surface roughness or chemical inhomogeinity in the samples. Increasing hysteresis value with increased filler content (Table 3), refers to increased variation of surface property along the contact line. The contact line of the polymer during advancement and receding decides the kind of interaction between the liquid and polymer. Decreasing contact angle value indicates increasing contact area thereby enhancing polymer-tissue adhesion.

3.5. Characterization of the foams (SEM)

Nucleation and cell expansion in a polymer with higher T_g value takes place not during depressurization, but in the high temperature foaming stage [36]. PLA has T_g much above the room temperature (around 60°C) indicating that diffusion out of the solvent causing nucleation and expansion in the current system occurred at the foaming temperature. Microcells are produced throughout the compositions as found from cell size and cell density calculation (Table 3) and these cellular structures are supposed to be supportive towards cell growth in biomedical scaffolding applications. The microcellular morphology of the composites is visibly different from the blend foam in terms of cell size distribution (Figure 4). With increasing filler content, cell diameter increased which correspondingly reduced cell density and PLCLW8 composition produced microcells larger than the blend itself giving minimum cell density value. This might be due to filler agglomeration at higher loading that reduces the bubble nucleation capability of the polymer. The inhomogeneity in the polymers is created by introducing immiscible domains of PCL and acicular inorganic filler. The blend also produces microcellular foams, but the presence of the filler adds uniformity in cell distribution because of lowered activation energy required for bubble nucleation at the interphases.

3.6. Cellular adhesion studies on the scaffold constructs

The present study compares the suitability of the polymeric scaffold constructs for cell culture with osteoblast cells. Cell proliferation and morphology of the cells were studied by doing MTT assay and SEM scan. Standard plot for MTT assay (inset plot of Figure 5) was prepared by running a blank experiment where cells were seeded in the media without the scaffold. The growing number of cells was counted for two different incubation periods i.e. 3 and 7 days by correlating absorbance by the scaffold with that in the standard plot and the result is shown in Figure 5. MTT assay result of the scaffolds shows that after 3 and 7 days of culture, the number of metabolically active cell is highest in PLCLW8 followed by PLCLW4 and PLCLW1 while remaining minimum in PLCL15 blend scaffold (Table 3). These results indicate that composites with $CaSiO_3$ filler are able to support the growth and

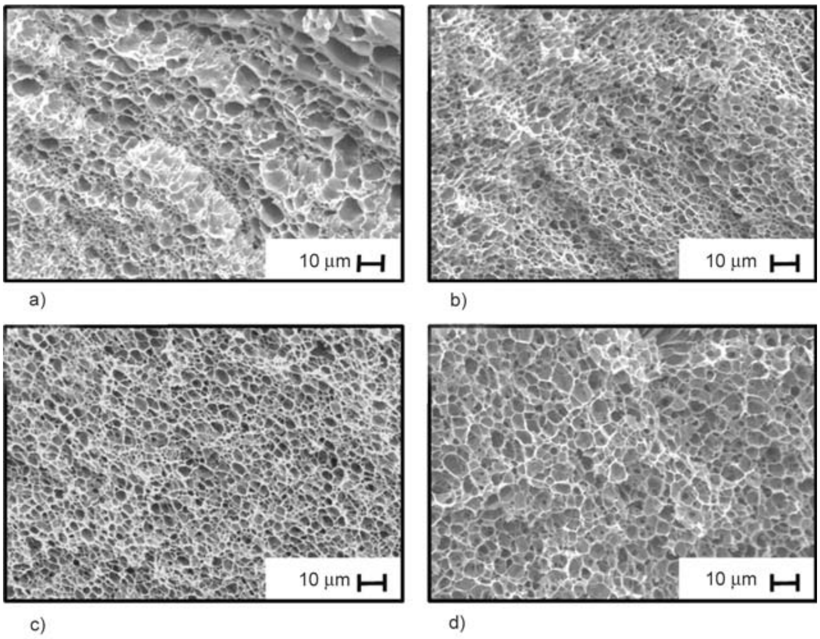

Figure 4. SEM images of cryofractured surfaces of the foams a) PLCL15, b) PLCLW1, c) PLCLW4 and d) PLCLW8

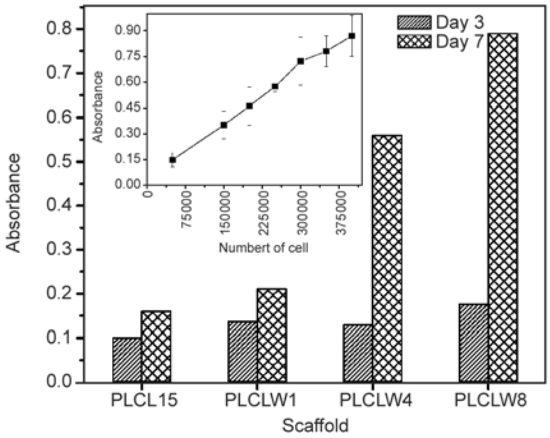

Figure 5. MTT assay absorbance data of the cell seeded scaffolds. The inset plot shows standard MTT curve for osteoblast cells.

proliferation of osteoblast cells more than the unfilled polymer (PLCL15). The enhanced proliferation in the composites as compared with the blend sample may be attributed to the alkaline ions released by the filler in contact with the culture media. It is reported that calcium silicate filler releases calcium and silicon ions in such media that maintains the media pH while improving cell adhesion to the scaffolds [37]. In SEM images (Figure 6) of the cell cultured scaffolds, the cells are characterized by a typical fibroblast-like morphology. *In vivo*, such morphology for osteoblastic-lineage cells is found only if osteoblasts are resting and covering inactive bone surfaces and bone lining cells. In the controlled blend composition, irregularly-shaped osteoblast with less cell count is seen. The MTT assay finding is further supported by the SEM scans showing more cell counts on the surfaces with increasing filler content. PLCLW8 scaffold construct having maximum filler content is fully layered by the osteoblast cells which are interconnected with each other as compared with PLCLW1 composition showing cell lining in a group manner and thus, enhanced bioactivity of the calcium silicate filler can be found in PLCLW8.

4. Conclusions

The current report is a comprehensive one starting from selecting the raw materials to the cell viability study on the prepared foams. The enhancement in mechanical properties of the composites along with favored cell growth on the scaffold constructs is evident from the experimental work. Wollastonite is a highly potential bioactive filler to induce cell attachment, differentiation and proliferation by inhibiting the deteriorating effects of acidic by-

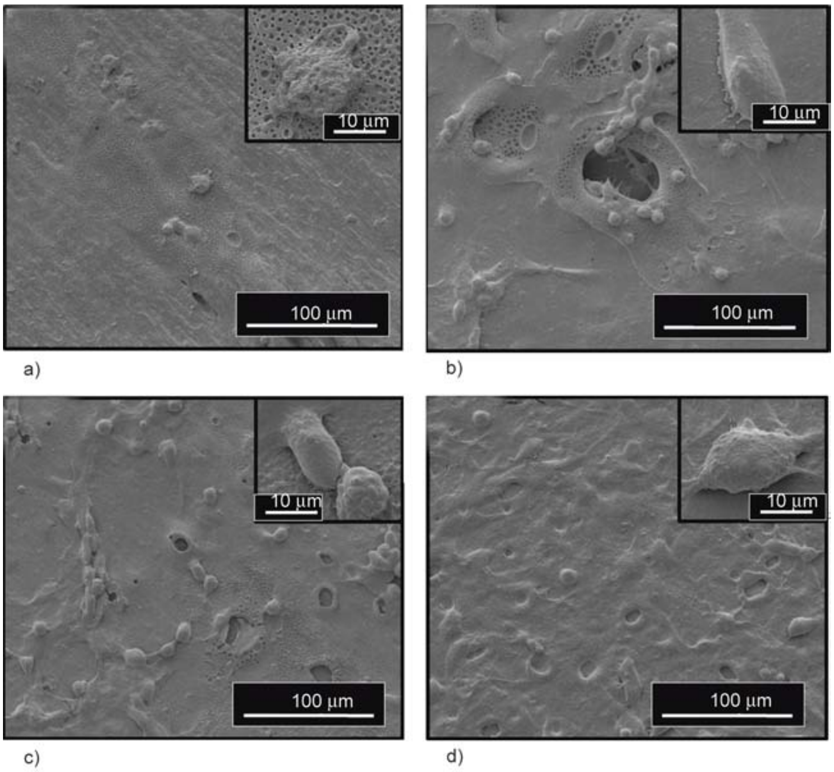

Figure 6. SEM scans of the osteoblast grown scaffolds after 7 days incubation period, a) PLCL15, b) PLCLW1, c) PLCLW4 and d) PLCLW8. The inset images show the fibroblast like morphology of individual cell at higher magnification.

products of biopolymers and releasing alkaline ions, thereby maintaining the pH of the surrounding environment of the damaged tissues at an optimum level for faster regeneration of the cells. The outcome of the present study is summarized below,

– Surface morphology of the unfoamed polymers established immiscible behavior of the three components in the composites.
– Compressive test reaffirmed the usability of the prepared polymers for *in vivo* application.
– Addition of wollastonite improved hydrophilicity of the polymers that helped in better implant-tissue adhesion.
– Presence of the filler improved foamability of the matrix by introducing heterogeneous nucleation sites in the polymers and producing uniform microcells.
– The biocompatibility study of the foamed constructs as scaffold proved that the $CaSiO_3$ filler helped in osteoblast cell lining throughout the scaffold surface that increased with increasing filler content in comparison to the controlled blend scaffold.

References

[1] Murugan R., Ramakrishna S.: Development of nanocomposites for bone grafting. Composites Science and Technology, **65**, 2385–2406 (2005).
DOI: 10.1016/j.compscitech.2005.07.022

[2] Ramakrishna S., Mayer J., Wintermantel E., Leong K. W.: Biomedical applications of polymer-composite materials: A review. Composites Science and Technology, **61**, 1189–1224 (2001).
DOI: 10.1016/S0266-3538(00)00241-4

[3] Broz M. E., VanderHart D. L., Washburn N. R.: Structure and mechanical properties of poly(D,L-lactic acid)/poly(ε-caprolactone) blends. Biomaterials, **24**, 4181–4190 (2003).
DOI: 10.1016/S0142-9612(03)00314-4

[4] Sarazin P., Li G., Orts W. J., Favis B. D.: Binary and ternary blends of polylactide, polycaprolactone and thermoplastic starch. Polymer, **49**, 599–609 (2008).
DOI: 10.1016/j.polymer.2007.11.029

[5] Weir N. A., Buchanan F. J., Orr J. F., Farrar D. F., Boyd A.: Processing, annealing and sterilisation of poly-L-lactide. Biomaterials, **25**, 3939–3949 (2004).
DOI: 10.1016/j.biomaterials.2003.10.076

[6] Di Lorenzo M. L.: Crystallization behavior of poly(L-lactic acid). European Polymer Journal, **41**, 569–575 (2005).
DOI: 10.1016/j.eurpolymj.2004.10.020

[7] Rezgui F., Swistek M., Hiver J. M., G'Sell C., Sadoun T.: Deformation and damage upon stretching of degradable polymers (PLA and PCL). Polymer, **46**, 7370–7385 (2005).
DOI: 10.1016/j.polymer.2005.03.116

[8] Chen C-C., Chueh J-Y., Tseng H., Huang H-M., Lee S-Y.: Preparation and characterization of biodegradable PLA polymeric blends. Biomaterials, **24**, 1167–1173 (2003).
DOI: 10.1016/S0142-9612(02)00466-0

[9] Liao H-T., Wu C-S.: Preparation and characterization of ternary blends composed of polylactide, poly(ε-caprolactone) and starch. Materials Science and Engineering: A, **515**, 207–214 (2009).
DOI: 10.1016/j.msea.2009.03.003

[10] López-Rodríguez N., López-Arraiza A., Meaurio E., Sarasua J. R.: Crystallization, morphology, and mechanical behavior of polylactide/poly(ε-caprolactone) blends. Polymer Engineering and Science, **46**, 1299–1308 (2006).
DOI: 10.1002/pen.20609

[11] Rasal R. M., Janorkar A. V., Hirt D. E.: Poly(lactic acid) modifications. Progress in Polymer Science, **35**, 338–356 (2010).
DOI: 10.1016/j.progpolymsci.2009.12.003

[12] Carrasco F., Pagès P., Gámez-Pérez J., Santana O. O., Maspoch M. L.: Processing of poly(lactic acid): Characterization of chemical structure, thermal stability and mechanical properties. Polymer Degradation and Stability, **95**, 116–125 (2010).
DOI: 10.1016/j.polymdegradstab.2009.11.045

[13] Todo M., Park S-D., Takayama T., Arakawa K.: Fracture micromechanisms of bioabsorbable PLLA/PCL polymer blends. Engineering Fracture Mechanics, **74**, 1872–1883 (2007).
DOI: 10.1016/j.engfracmech.2006.05.021

[14] Li H., Chang J.: Preparation and characterization of bioactive and biodegradable Wollastonite/poly(D,L-lactic acid) composite scaffolds. Journal of Materials Science: Materials in Medicine, **15**, 1089–1095 (2004).
DOI: 10.1023/B:JMSM.0000046390.09540.c2

[15] Kokubo T.: Apatite formation on surfaces of ceramics, metals and polymers in body environment. Acta Materialia, **46**, 2519–2527 (1998).
DOI: 10.1016/S1359-6454(98)80036-0

[16] Wang M.: Developing bioactive composite materials for tissue replacement. Biomaterials, **24**, 2133–2151 (2003).
DOI: 10.1016/S0142-9612(03)00037-1

[17] Kothapalli C. R., Shaw M. T., Wei M.: Biodegradable HA-PLA 3-D porous scaffolds: Effect of nano-sized filler content on scaffold properties. Acta Biomaterialia, **1**, 653–662 (2005).
DOI: 10.1016/j.actbio.2005.06.005

[18] Wan X., Chang C., Mao D., Jiang L., Li M.: Preparation and *in vitro* bioactivities of calcium silicate nanophase materials. Materials Science and Engineering: C, **25**, 455–461 (2005).
DOI: 10.1016/j.msec.2004.12.003

[19] Zhang N., Molenda J. A., Fournelle J. H., Murphy W. L., Sahai N.: Effects of pseudowollastonite ($CaSiO_3$) bioceramic on *in vitro* activity of human mesenchymal stem cells. Biomaterials, **31**, 7653–7665 (2010).
DOI: 10.1016/j.biomaterials.2010.06.043

[20] Wu C., Zhang Y., Fan W., Ke X., Hu X., Zhou Y., Xiao Y.: $CaSiO_3$ microstructure modulating the *in vitro* and *in vivo* bioactivity of poly(lactide-*co*-glycolide) microspheres. Journal of Biomedical Materials Research Part A, **98**, 122–131 (2011).
DOI: 10.1002/jbm.a.33092

[21] Li X., Shi J., Zhu Y., Shen W., Li H., Liang J., Gao J.: A template route to the preparation of mesoporous amorphous calcium silicate with high *in vitro* bone-forming bioactivity. Journal of Biomedical Materials Research Part B: Applied Biomaterials, **83**, 431–439 (2007).
DOI: 10.1002/jbm.b.30813

[22] Lim Y-M., Gwon H-J., Shin J., Jeun J. P., Nho Y. C.: Preparation of porous poly(ε-caprolactone) scaffolds by gas foaming process and *in vitro/in vivo* degradation behavior using γ-ray irradiation. Journal of Industrial and Engineering Chemistry, **14**, 436–441 (2008).
DOI: 10.1016/j.jiec.2008.01.019

[23] Wei J., Chen F., Shin J-W., Hong H., Dai C., Su J., Liu C.: Preparation and characterization of bioactive mesoporous wollastonite – polycaprolactone composite scaffold. Biomaterials, **30**, 1080–1088 (2009).
DOI: 10.1016/j.biomaterials.2008.10.046

[24] Sung H-J., Meredith C., Johnson C., Galis Z. S.: The effect of scaffold degradation rate on three-dimensional cell growth and angiogenesis. Biomaterials, **25**, 5735–5742 (2004).
DOI: 10.1016/j.biomaterials.2004.01.066

[25] Sauceau M., Fages J., Common A., Nikitine C., Rodier E.: New challenges in polymer foaming: A review of extrusion processes assisted by supercritical carbon dioxide. Progress in Polymer Science, **36**, 749–766 (2011).
DOI: 10.1016/j.progpolymsci.2010.12.004

[26] Fujimoto Y., Ray S. S., Okamoto M., Ogami A., Yamada K., Ueda K.: Well-controlled biodegradable nanocomposite foams: From microcellular to nanocellular. Macromolecular Rapid Communications, **24**, 457–461 (2003).
DOI: 10.1002/marc.200390068

[27] Matuana L. M., Faruk O., Diaz C. A.: Cell morphology of extrusion foamed poly(lactic acid) using endothermic chemical foaming agent. Bioresource Technology, **100**, 5947–5954 (2009).
DOI: 10.1016/j.biortech.2009.06.063

[28] Yu L., Liu H., Dean K., Chen L.: Cold crystallization and postmelting crystallization of PLA plasticized by compressed carbon dioxide. Journal of Polymer Science Part B: Polymer Physics, **46**, 2630–2636 (2008).
DOI: 10.1002/polb.21599

[29] Kazarian S. G., Vincent M. F., Bright F. V., Liotta C. L., Eckert C. A.: Specific intermolecular interaction of carbon dioxide with polymers. Journal of the American Chemical Society, **118**, 1729–1736 (1996).
DOI: 10.1021/ja950416q

[30] Nalawade S. P., Picchioni F., Marsman J. H., Janssen L. P. B. M.: The FT-IR studies of the interactions of CO_2 and polymers having different chain groups. The Journal of Supercritical Fluids, **36**, 236–244 (2006).
DOI: 10.1016/j.supflu.2005.06.005

[31] Lee S. T., Ramesh N. S.: Polymeric foams: Mechanisms and materials. CRC Press, Boca Raton (2004).

[32] Zhao S., Zhou Z., Wu J., Wang S., Guo X., Zhang Q.: Preparation and characterization of a novel hydroxyapatite-wollastonite/silk fibroin composite. Journal of Composite Materials, **46**, 1571–1581 (2012).
DOI: 10.1177/0021998311421040

[33] Javni I., Zhang W., Karajkov V., Petrovic Z. S., Divjakovic V.: Effect of nano- and micro-silica fillers on polyurethane foam properties. Journal of Cellular Plastics, **38**, 229–239 (2002).
DOI: 10.1177/0021955x02038003139

[34] Zhang Q., Yang H., Fu Q.: Kinetics-controlled compatibilization of immiscible polypropylene/polystyrene blends using nano-SiO_2 particles. Polymer, **45**, 1913–1922 (2004).
DOI: 10.1016/j.polymer.2004.01.037

[35] Li H., Chang J.: Fabrication and characterization of bioactive wollastonite/PHBV composite scaffolds. Biomaterials, **25**, 5473–5480 (2004).
DOI: 10.1016/j.biomaterials.2003.12.052

[36] Matuana L. M., Faruk O.: Effect of gas saturation conditions on the expansion ratio of microcellular poly (lactic acid)/wood-flour composites. Express Polymer Letters, **4**, 621–631 (2010).
DOI: 10.3144/expresspolymlett.2010.77

[37] Xu L., Xiong Z. C., Yang D., Zhang L. F., Chang J., Xiong C. D.: Preparation and *in vitro* degradation of novel bioactive polylactide/wollastonite scaffolds. Journal of Applied Polymer Science, **114**, 3396–3406 (2009).
DOI: 10.1002/app.28475

eXPRESS Polymer Letters Vol.7, No.9 (2013) 778–786
Available online at www.expresspolymlett.com
DOI: 10.3144/expresspolymlett.2013.75

Structural characteristics and enhanced mechanical and thermal properties of full biodegradable tea polyphenol/poly(3-hydroxybutyrate-*co*-3-hydroxyvalerate) composite films

H. X. Xiang, S. H. Chen, Y. H. Cheng, Z. Zhou, M. F. Zhu[*]

State Key Laboratory for Modification of Chemical Fibers and Polymer Materials, and College of Materials Science and Engineering, Donghua University, 201620 Shanghai, P.R.China

Received 20 April 2013; accepted in revised form 2 June 2013

Abstract. Full biodegradable poly(3-hydroxybutyrate-*co*-3-hydroxyvalerate) (PHBV) composite films were prepared with 5~40 wt% green tea polyphenol (TP) as toughener. The effects of mixing TP on mechanical properties, thermal properties and hydrophilic-hydrophobic properties of composite films were investigated. Tension test results show that the incorporation of TP in the PHBV matrix can enhance the toughness of the composite films. Differential scanning calorimetric (DSC) studies show that there is a single glass transition temperature and the lower melting point temperature. Fourier transform infrared (FT-IR) results confirm that the intermolecular hydrogen bonding interactions in composite films. Contact angle measurements show that the hydrophilicity of TP/PHBV composite films can be controlled through adjusting the composition of TP.

Keywords: *biodegradable polymers, poly(hydroxybutyrate-co-hydroxyvalerate), tea polyphenol, mechanical properties, thermal properties*

1. Introduction

Recently, bacterial polyester poly(hydroxybutyrate-*co*-hydroxyvalerate) (PHBV) has been arising much attention in the field of biomedical and environmental friendly materials because of its good biocompatibility, biodegradability as well as thermoplastic properties. However, the wide application has been restricted by the poor mechanical properties and narrow processing window [1]. Therefore, a significant amount of work has been devoted to improving mechanical and thermal properties of PHBV via PHBV-based polymer blends and composites [2]. This work mainly covers four aspects: nanoparticles/PHBV composites, traditional petrochemical-based materials/PHBV composites, biodegradable petrochemical-based polymer/PHBV composites, and bio-based materials/PHBV composites.

In nanoparticles/PHBV composites, inorganic nanoparticles mainly include oxide [3], nitride [4], mineralization materials [5, 6], carbon materials or minerals [7], and layered double hydroxides [8, 9]. Organic nanoparticles mainly include cellulose nanocrystal [10], chitosan nanocrystal and starch nanocrystal [11]. The introduction of nanoparticles is helpful for improving the physical properties and processing properties of PHBV through increasing the nucleation density and decreasing the spherulite size. In petrochemical-based materials/PHBV composites, the additive components consist mainly of non-biodegradable polyolefin [12], polyurethane

---

[*]Corresponding author, e-mail: zhumf@dhu.edu.cn

elastomer [13] polyaniline [14]. These blending composites can improve physical properties by some extent and reduce the cost, but also there are some problems in compatibility. So Sadik improved the interfacial and mechanical properties of the immiscible PP/PHBV and PE/PHBV blends by preformed copolymer EVOH-g-PHBV [12]. In biobased materials/PHBV composites, thermoplastic starch, cellulose, polycaprolactone [15], xylogen [16], polylactic acid [17], PBAT [18] and poly (butylenes succinate) [19] are widely applied to fully biodegradable products [20, 21].

In the method of toughening PHBV, bisphenol A (BPA) as one prominent modifiers, it deters the biodegradability and biocompatibility of PHBV. In order to solve the environmental pollution fundamentally, bio-based materials/PHBV composites are the main direction. As a bio-based material, tea polyphenol (TP) deriving from natural tea leaves is a kind of phenolic compound which contains multiple hydroxyl groups [22]. So fully biodegradable TP was chosen to replace BPA. The major component of TP is catechin, and its chemical structure is shown in Figure 1. This structure provides a large amount of phenolic hydroxyl groups in proton-donating TP and allows it to take advantages of inhibiting bacterium, cancer, tumors.

Herein, fully biodegradable TP/PHBV composite films were prepared via solution blending and spin coating method with hydrogen bonding interaction with 5~40 wt% green TP as proton donor and biopolyester PHBV as proton acceptor. The tensile properties of composite films were studied to investigate the toughening effect of TP on PHBV matrix. The physical properties, thermal properties, crystalline structure and morphology were characterized by Fourier transform infrared spectroscopy (FTIR), differential scanning calorimetry (DSC), polarization optical microscopy (POM) and wide angle X-ray diffraction (WXRD).

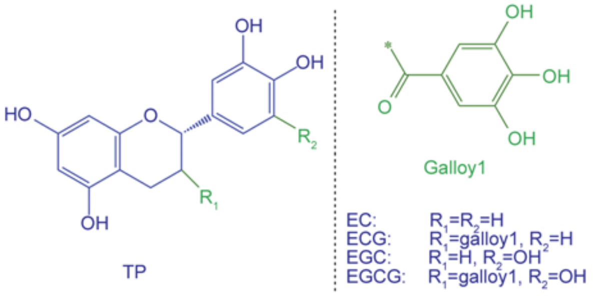

Figure 1. Chemical structure of TP

2. Experimental

2.1. Materials

PHBV with 1.09 mol% 3-hydroxyvalerate (HV) [$M_\text{n} = 1.16\cdot10^4$ g·mol^{-1}, M_w/M_n =2.30] was obtained from Tianan Biologic Material Co., Ltd. (Ningbo, China). Tea polyphenol (TP) (polyphenols≥98%, catechin≥80%, EGCG≥60%, caffeinne≤1.0%) was purchased from Xuancheng Baicao Plant Industry and Trade Co., Ltd (Xuancheng, China). Chloroform and dioxane were obtained from Sinopharm Chemical Reagent Co., Ltd. (Shanghai, China) and used as received.

2.2. Preparation of TP/PHBV composite films

First, PHBV was completely dissolved in chloroform at 60°C in a three-necked flask with a magnetic stirrer. Then, the TP dioxane solutions with different mass fractions (5, 10, 20, 30 and 40 wt%) were mixed and stirred with the PHBV solution at room temperature for 6 h, respectively. Finally, these solutions were cast into films by an applicator. The solvent was allowed to evaporate slowly at room temperature for 48 h, and the resulting films were further dried under vacuum drying oven at 25°C for another 48 h.

2.3. Characterization

The tensile properties of TP/PHBV composite films were measured by an INSTRON 5969 electronic universal material testing machine (Instron Corporation, USA). Tensile specimens with 10 mm in width and 10 μm in thickness were drawn at a strain rate of 1 mm/min. The gauge length was 50 mm, and five replicates were run for each sample.

The hydrogen bond interactions between TP and PHBV were characterized by FT-IR spectrometer (Thermo Nicolet 8700, USA). These tests were carried out by the DTGS-MCT-A double-detector.

The crystalline structures of TP/PHBV composites were obtained with a D/Max-2550 PC diffractometer (Japan). All the samples were allowed to set aside for two weeks at room temperature to reach equilibrium crystallization. CuK$_\alpha$ X-ray source was used with a wavelength (λ) of 0.154 nm. The angle of incidence varies from 5 to 60° by steps of 0.02°.

In order to directly understand the mobility of molecular chain of TP/PHBV composites, the crystal growth behaviors and crystalline morphologies of different composites were observed by DM2500P polarizing optical microscope with LINKAM

LTSE350 hot stage (Leica, Germany), and the radial growth rate of spherulites was calculated by data processing software. The samples were sandwiched between two cover slides and kept at 200°C for 2 min and then cooled down to a desired isothermal crystallization temperature with a cooling rate of 30°C/min. The growth rate of spherulite was calculated by the recorded photographs which are taken at constant time intervals.

The melting and crystallization behaviors of TP/PHBV composites were carried out by DSC (Q20, USA) with nitrogen as purging gas. Samples were firstly put on the 200°C hot stage for 4 min, waited until it was fully molten and put it into liquid nitrogen. Then the thermal properties of these samples were tested. The samples were heated from –50 to 200°C at a rate of 10°C/min.

The contact angles of the PHBV film and TP/PHBV composite films were measured via 322 W contact angle analyzer (Thermo Cahn, USA) at room temperature. About 2 µL deionized water was dropped on the film surface for the tests at a contact time of 5 s. Five independent determinations at different sites of the film were averaged.

3. Results and discussion

3.1. Mechanical properties of TP/PHBV composite films

The stress-strain curves, tensile strength, and elongation at break of TP/PHBV composite films with various TP contents are shown in Figure 2. The toughness of TP/PHBV composite films increases sharply with an increase content of plant polyphenol TP. When the TP content increases from 0 to 20 wt%, the elongation at break of TP/PHBV composite films improved from 1.5 to 36.5%, with an increasing ratio of 2430%. This occurs because of the hydrogen bonding interaction between phenolic hydroxyl groups in TP and carbonyl ester groups in PHBV, which may delay the failure of PHBV under the tensile stress. TP also acts as a low molecular weight plasticizer, when the TP content is lower than 5 wt%, the tensile strength of composites tends to increase from 14.0 to 14.6 MPa. Meanwhile, the strain and elongation at break both increases by 5%. However, when the TP content exceeded 10 wt%, the tensile strength of the composite films decreased rapidly. This type of variation trend also appeared in the results of fracture work for TP/PHBV composite films. When TP content increased up to 20 wt%, the elongation at break of composite films reached the maximum value of 36.5%, while the tensile strength decreased to 6.6 MPa. These results show that the incorporation of TP in the PHBV matrix can enhance the toughness of the composite films. When TP content exceeded 30 wt%, the tensile strength and elongation at break of TP/PHBV composite films fell notably.

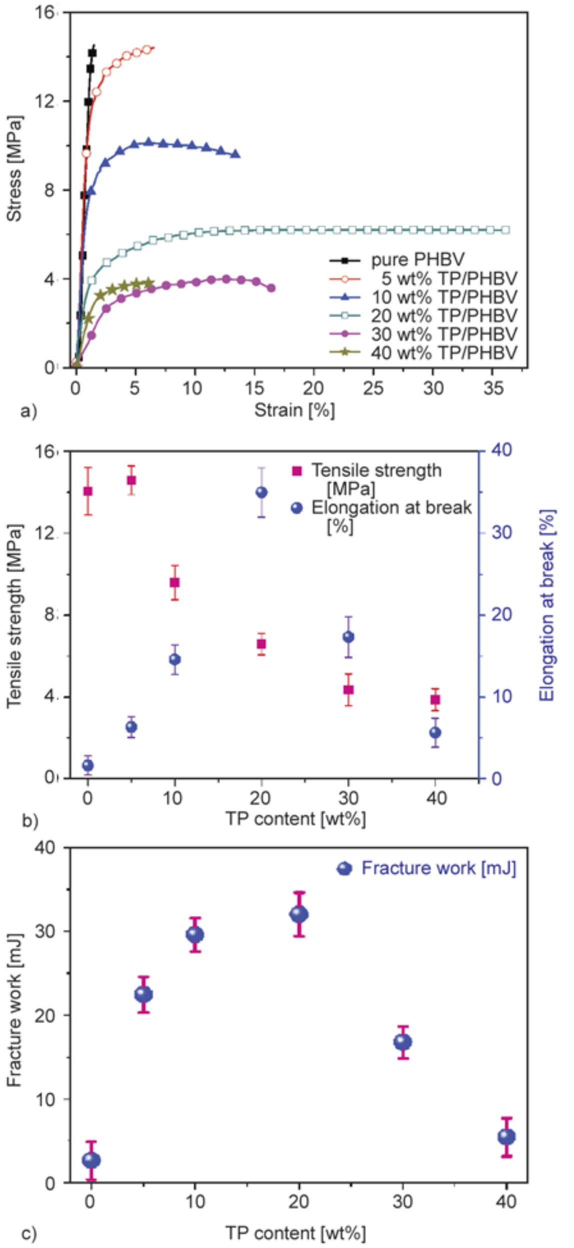

Figure 2. Stress-strain curves (a), tensile properties (b) and fracture work (c) of TP/PHBV composite films with various TP contents

3.2. Thermal properties of TP/PHBV composites

The mechanical properties of polymer materials are significantly dependent on the glass transition temperature (T_g). Because the T_g of PHBV is lower than room temperature, so secondary crystallization of its products often occur easily during storage, and resulting in the decrease of its mechanical properties. So green TP is used to improve its T_g.

DSC melting curves of PHBV and TP/PHBV composites is shown in Figure 3. The thermal parameters, such as T_g, cold crystallization temperature (T_{cc}), melting temperature (T_m), cold crystallization enthalpies (ΔH_{cc}), melting enthalpy (ΔH_m), is shown in Table 1. The degree of crystallinity (X_{DSC}) is also calculated by Equation (1) [23] to examine the changes caused by TP additives:

$$X_{DSC} = \frac{\Delta H_f}{(1-\varphi_{TP})\Delta H_f^0} \cdot 100\% \qquad (1)$$

where X_{DSC} is the degree of crystallinity of PHBV and its composites, φ_{TP} is the weight fraction of TP, ΔH_f is the measured melting enthalpies and ΔH_f^0 is the enthalpies of 100% crystalline PHBV, which is chosen as 146.6 J g^{-1} for PHB.

In Figure 3 and Table 1, with the TP content increasing from 0 to 40 wt%, the T_g improved from 1.8 to 56.4°C, increasing by 54.6°C. The cold crystallization temperature increased from 43.4 to 109.5°C, and the melting temperature decreased from 174.6 to 157.7°C. These maybe occurred by the formation of the intermolecular hydrogen bonding interaction. As an effect of adding TP component on PHBV, its composites showed a single glass transition temperature and the lower melting point temperature. Moreover, the T_g was increased accordingly.

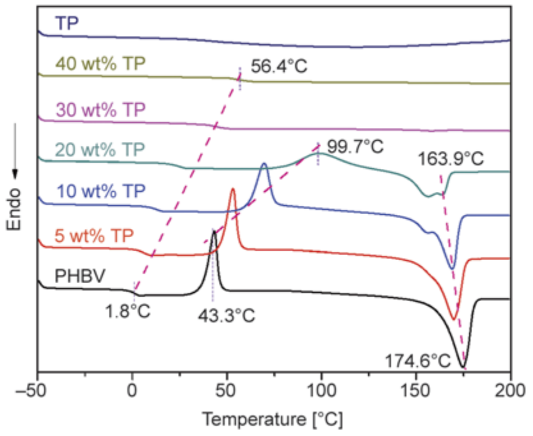

Figure 3. DSC melting curves of PHBV and TP/PHBV composites

The crystallinity of TP/PHBV composites also calculated by the change of enthalpies and are also shown in Table 1. The crystallinity of composites decreases with the increase of TP content. The decrease of crystallinity maybe influenced by hydrogen bonding interaction between PHBV and TP, which restricts the motion ability of molecular chain.

Figure 4 shows the crystallize patterns of PHBV and TP/PHBV composites at 40°C, respectively. In Figure 4a, the pure PHBV spherulites display the well-known Maltese cross extinction pattern and the concentric extinction rings with the radial growth rate of 1.08 μm/s. When the TP contents was 5 wt%, 'Maltese cross' extinction pattern also appeared in composite, however the banded pattern changed to radial pattern. Moreover, the spherulite radius and the radial growth rate decreased with an increase of TP content. When the TP content reached 20 wt%, spherulite formation can't be observed resulting from the arrangement and the growth modes of spherulites lamellar layers, which are depending on polymer aggregate structure at the same isothermal crystallization temperature and degree of supercooling. The banded spherulites for PHBV generate band pattern of dark and light, which can be related to twisting period of the spherulites radial growth corresponding to extinction spacing, and the adjacent lamellar layers keep

Table 1. Thermal parameters of PHBV and TP/PHBV composites

Sample	T_g [°C]	T_{cc}^{a} [°C]	ΔH_{cc} [J·g^{-1}]	T_m [°C]	ΔH_m [J·g^{-1}]	X_{DSC}^{b} [%]	X_{WXRD}^{c} [%]
Pure PHBV	1.81	43.28	36.13	174.61	89.12	61.04	53.03
5 wt% TP/PHBV	6.36	53.08	37.83	169.89	80.34	57.92	48.83
10 wt% TP/PHBV	12.81	69.64	39.16	169.01	73.88	56.23	41.32
20 wt% TP/PHBV	24.80	99.74	37.76	163.88	50.43	43.18	40.72
30 wt% TP/PHBV	45.67	109.45	–	157.69	1.05	1.03	38.05
40 wt% TP/PHBV	56.35	–	–	–	–	–	31.64
Pure TP	–	–	–	–	–	–	8.19

[a] T_{cc} is the cold crystallization temperature.
[b] Determined from DSC enthalpy parameters.
[c] Determined from WXRD spectra

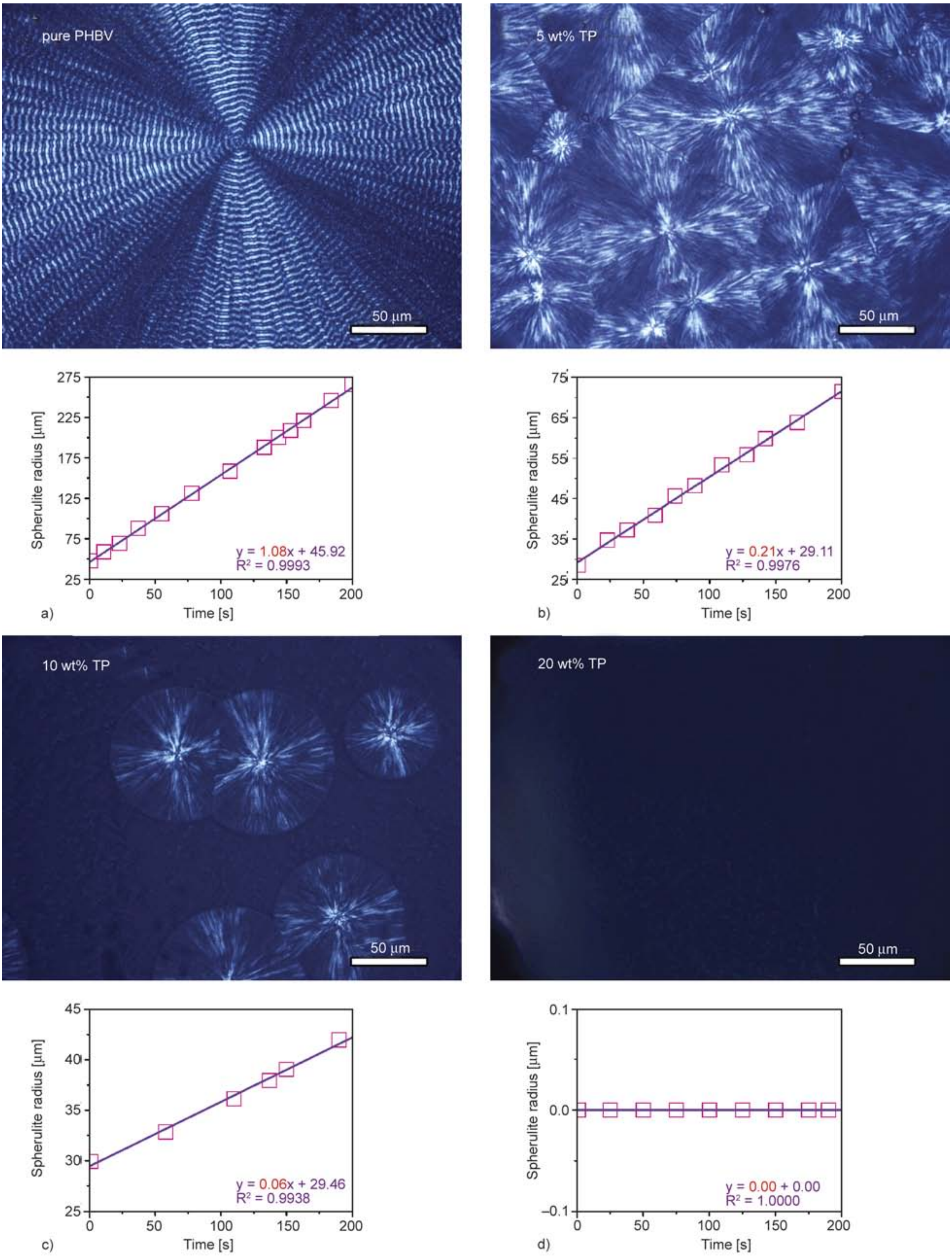

Figure 4. Crystalline morphology and radial growth rate of the spherulites of PHBV (a) and TP/PHBV composites (b) 5 wt% TP/PHBV, (c) 10 wt% TP/PHBV and (d) 20 wt% TP/PHBV at a constant temperature of 40°C

the same period and phase to twist. In the TP/PHBV composites, TP component as organic rigid toughening material plays the role of the proton-donating material. The intermolecular hydrogen bonding interaction restricts molecular chain motion on PHBV component, and break coordination effect of lamellae layers of the PHBV spherulites radial growth. As a result, banded spherulite patterns were replaced by radial patterns.

3.3. Hydrophilic-hydrophobic properties of TP/PHBV composites

In order to preliminary study on the application of TP/PHBV composite films, contact angle with water of pure PHBV film and TP/PHBV composite film with various TP contents are shown in Figure 5. The contact angle of TP/PHBV composite films showed a decreasing trend with the increase of TP content, from 97.3 to 54.2°. It can be explained by the hydrophilic interaction for phenolic hydroxyl groups in natural polyphenol TP. In the TP/PHBV composite films, some phenolic hydroxyl groups were exposed on the film surface and changed the surface tension of composite film, which accounted for the improvement of its hydrophilicity. On the other side, biocompatible TP has strong sterilizing function, which should be attributed to the α-phenylbenzopyran structure in TP. With the combination of above advantages, it is expected that the TP/PHBV composites possess some promising applications in biomedical fields.

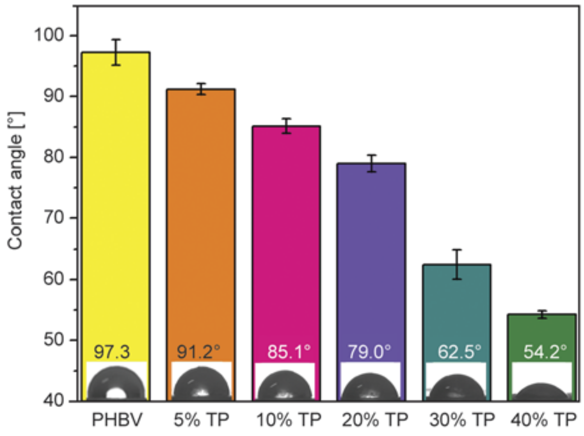

Figure 5. Contact angle of pure PHBV film and TP/PHBV composite films with various TP contents

3.4. Intermolecular interactions of TP/PHBV composites

For a better understanding of the hydrogen bonding interaction between TP and PHBV, the FT-IR was used to observe the change of absorption peaks of characteristic groups. Figure 6 shows the FT-IR spectra of TP/PHBV composites, with the stretching vibrations of hydroxyl (υ_{O-H}) and carbonyl ($\upsilon_{C=O}$) groups. All the characteristic absorption peaks of PHBV and TP appear in TP/PHBV composites, while the positions of hydroxyl and carbonyl stretching vibration peaks have changed. TP shows one broad band, centered at 3380 cm^{-1}, which attributed to the phenolic hydroxyl stretching vibration. For pure PHBV, only a weak peak band centered at 3440 cm^{-1} is observed in this region, which should be attributed to the stretching of the chain-end hydroxyl groups [24]. In Figure 6b, a new band appears at about 3250 cm^{-1} which presumably was induced by the formation of inter-molecular hydrogen bonding between TP and PHBV.

To illustrate hydrogen bonding interaction, the carbonyl ($\upsilon_{C=O}$) stretching vibration band in the range from 1660 to 1800 cm^{-1} was analyzed. As is shown in Figure 6b, the peak band around 1722 cm^{-1} should be attributed to the crystalline region of the car bonyl group of PHBV, which is very clear for neat PHBV, and the peak at around 1746 cm^{-1} to the amorphous region of the carbonyl group [22, 25,

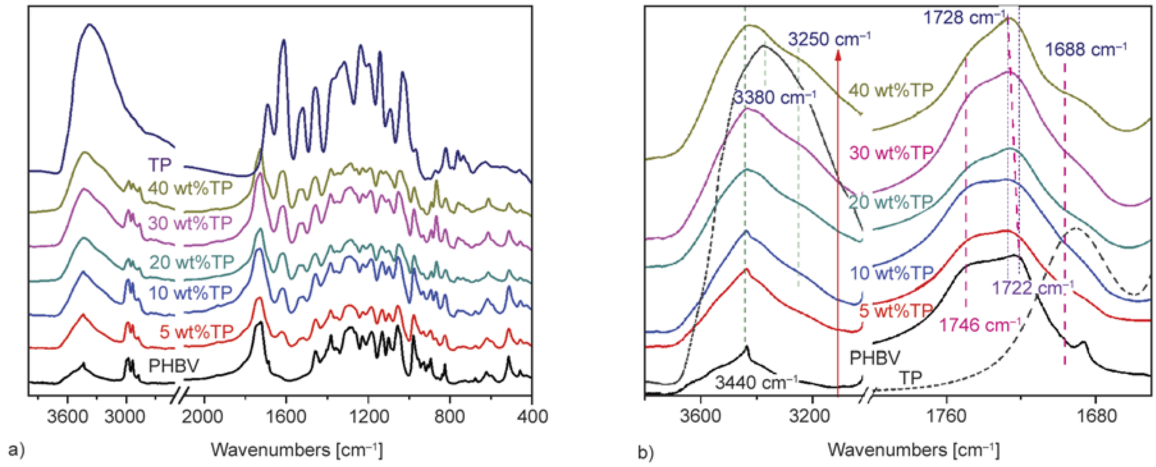

Figure 6. FT-IR spectra of TP/PHBV composites (a), hydroxyl stretching region and carbonyl stretching region in the range of 3800~3000 and 1800~1650 cm^{-1} (b)

26]. When the PHBV is blended with TP, a new band appears at lower wave-number about 1688 cm^{-1}. This new band is assigned to the hydrogen-bonded carbonyl groups. With the increase of the TP content, the carbonyl peak position for parts of crystalline region of the carbonyl group is shifting from 1722 to 1728 cm^{-1}, whereas that parts of the free C=O group is almost invariable. This suggested that the hydrogen bonding interaction is formed between the phenolic hydroxyl and carboxyl groups, which is consistent with the results of hydroxyl ($\upsilon_{O\text{–}H}$) stretching vibration band.

3.5. Crystalline structure of TP/PHBV composites

The physical properties of polymer composite films not only depend on the intermolecular force but also on the degree of crystallinity. The effect of addition TP component on PHBV crystal structure was characterized by WAXD, and the patterns of PHBV and TP/PHBV composites are shown in Figure 7. The diffraction peaks of (020), (110), (021), (101), (111), (121), (040) and (002) for PHBV crystal face appeared in WXRD patterns. And the TP did not significantly affect the diffraction peak position of TP/PHBV composites. This indicates that the introduction of the TP component in composites doesn't change the crystal structure of PHBV. From Figure 7 and Table 1, the crystallinity of PHBV component decreases with an increase in TP content, reducing from 53 to 32%. The decrease of crystallinity maybe influenced by hydrogen bonding interaction between PHBV and TP, which is consistent with the results discussed in DSC.

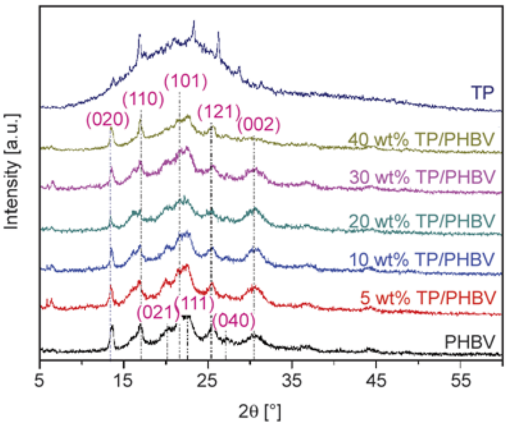

Figure 7. XRD patterns of PHBV and TP/PHBV composites

4. Conclusions

Biodegradable TP/PHBV composites were prepared with green TP and bacterial polyester PHBV. The intermolecular hydrogen bonding interactions in composites were confirmed through the shift of hydroxyl ($\upsilon_{O\text{–}H}$) and carbonyl ($\upsilon_{C=O}$) stretching vibration peaks. By adding TP components to PHBV matrix, the mechanical and thermal properties of TP/PHBV composite films were improved. Compared with pure PHBV, the elongation at break increased 24 times, meanwhile, the glass transition temperature and cold crystallization peak temperature increased by almost 45 and 45°C, respectively. The hydrophilicity of TP/PHBV composites can be controlled through adjusting the dosage of TP. Therefore, the result of this composite system will have an important effect on broadening the green plant polyphenol application and expanding the modification methods for preparing fully biodegradable environmental-friendly bacterial polyester materials.

Acknowledgements

This research is financially supported by the National Natural Science Foundation for Distinguished Young Scholar of China (50925312), The Program for Changjiang Scholars and Innovative Research Team in University (T2011079, IRT1221), the National Natural Science Foundation of China (50873022), the Program of Talents of Discipline to University (111-2-04), the Specialized Research Fund for the Doctoral Program of Higher Education (20100075110007) and the Chinese Universities Scientific Fund (CUSF-DH-D-2013007).

References

[1] Adamus G., Sikorska W., Kowalczuk M., Montaudo M., Scandola M.: Sequence distribution and fragmentation studies of bacterial copolyester macromolecules: Characterization of PHBV macroinitiator by electrospray ion-trap multistage mass spectrometry. Macromolecules, **33**, 5797–5802 (2000).
DOI: 10.1021/ma000005g

[2] Zhu B., Li J., He Y., Yoshie N., Inoue Y.: Hydrogen-bonding interaction and crystalline morphology in the binary blends of poly(ε-caprolactone) and polyphenol catechin. Macromolecular Bioscience, **3**, 684–693 (2003).
DOI: 10.1002/mabi.200350034

[3] Serpell C. J., Cookson J., Ozkaya D., Beer P. D.: Core@shell bimetallic nanoparticle synthesis via anion coordination. Nature Chemistry, **3**, 478–483 (2011).
DOI: 10.1038/nchem.1030

[4] Wang L., Wang X. J., Zhu W. F., Chen Z. F., Pan J. Y., Xu K. T.: Effect of nucleation agents on the crystallization of poly(3-hydroxybutyrate-*co*-4-hydroxybutyrate) (P3/4HB). Journal of Applied Polymer Science, **116**, 1116–1123 (2010).
DOI: 10.1002/app.31588

[5] Carli L. N., Crespo J. S., Mauler R. S.: PHBV nanocomposites based on organomodified montmorillonite and halloysite: The effect of clay type on the morphology and thermal and mechanical properties. Composites Part A: Applied Science and Manufacturing, **42**, 1601–1608 (2011).
DOI: 10.1016/j.compositesa.2011.07.007

[6] Kaur J., Lee J. H., Shofner M. L.: Influence of polymer matrix crystallinity on nanocomposite morphology and properties. Polymer, **52**, 4337–4344 (2011).
DOI: 10.1016/j.polymer.2011.07.020

[7] Sridhar V., Lee I., Chun H. H., Park H.: Graphene reinforced biodegradable poly(3-hydroxybutyrate-*co*-4-hydroxybutyrate) nano-composites. Express Polymer Letters, **7**, 320–328 (2013).
DOI: 10.3144/expresspolymlett.2013.29

[8] Zhang R., Huang H., Yang W., Xiao X., Hu Y.: Preparation and characterization of bio-nanocomposites based on poly(3-hydroxybutyrate-*co*-4-hydroxybutyrate) and CoAl layered double hydroxide using melt intercalation. Composites Part A: Applied Science and Manufacturing, **43**, 547–552 (2012).
DOI: 10.1016/j.compositesa.2012.01.005

[9] Dagnon K. L., Robinson C., Chen H. H., Garrett D. C., Innocentini-Mei L. H., D'Souza N. A.: Layer double hydroxides for enhanced poly(3-hydroxybutyrate-*co*-3-hydroxyvalerate) crystallization. Journal of Applied Polymer Science, **127**, 3395–3406 (2013).
DOI: 10.1002/app.37646

[10] Schacher F. H., Rupar P. A., Manners I.: Functional block copolymers: Nanostructured materials with emerging applications. Angewandte Chemie International Edition, **51**, 7898–7921 (2012).
DOI: 10.1002/anie.201200310

[11] Patrício P., Pereira F. V., dos Santos M. C., de Souza P. P., Roa J. P. B., Orefice R. L.: Increasing the elongation at break of polyhydroxybutyrate biopolymer: Effect of cellulose nanowhiskers on mechanical and thermal properties. Journal of Applied Polymer Science, **127**, 3613–3621 (2013).
DOI: 10.1002/app.37811

[12] Sadik T., Massardier V., Becquart F., Taha M.: Polyolefins/poly(3-hydroxybutyrate-*co*-hydroxyvalerate) blends compatibilization: Morphology, rheological, and mechanical properties. Journal of Applied Polymer Science, **127**, 1148–1156 (2013).
DOI: 10.1002/app.37957

[13] Naguib H. F., Aziz M. S. A., Saad G. R.: Synthesis, morphology and thermal properties of polyurethanes nanocomposites based on poly(3-hydroxybutyrate) and organoclay. Journal of Industrial and Engineering Chemistry, **19**, 56–62 (2013).
DOI: 10.1016/j.jiec.2012.06.023

[14] Araujo P. L. B., Ferreira C. R. P. C., Araujo E. S.: Biodegradable conductive composites of poly(3-hydroxybutyrate) and polyaniline nanofibers: Preparation, characterization and radiolytic effects. Express Polymer Letters, **5**, 12–22 (2011).
DOI: 10.3144/expresspolymlett.2011.3

[15] Hinüber C., Häussler L., Vogel R., Brünig H., Heinrich G., Werner C.: Hollow fibers made from a poly(3-hydroxybutyrate)/poly-ε-caprolactone blend. Express Polymer Letters, **5**, 643–652 (2011).
DOI: 10.3144/expresspolymlett.2011.62

[16] Mousavioun P., George G. A., Doherty W. O. S.: Environmental degradation of lignin/poly(hydroxybutyrate) blends. Polymer Degradation and Stability, **97**, 1114–1122 (2012).
DOI: 10.1016/j.polymdegradstab.2012.04.004

[17] Zhao Q., Wang S., Kong M., Geng W., Li R. K. Y., Song C., Kong D.: Phase morphology, physical properties, and biodegradation behavior of novel PLA/PHBHHx blends. Journal of Biomedical Materials Research Part B: Applied Biomaterials, **100**, 23–31 (2012).
DOI: 10.1002/jbm.b.31915

[18] Nagarajan V., Misra M., Mohanty A. K.: New engineered biocomposites from poly(3-hydroxybutyrate-*co*-3-hydroxyvalerate) (PHBV)/poly(butylene adipate-*co*-terephthalate) (PBAT) blends and switchgrass: Fabrication and performance evaluation. Industrial Crops and Products, **42**, 461–468 (2013).
DOI: 10.1016/j.indcrop.2012.05.042

[19] Ma P., Hristova-Bogaerds D. G., Lemstra P. J., Zhang Y., Wang S.: Toughening of PHBV/PBS and PHB/PBS blends via *in situ* compatibilization using dicumyl peroxide as a free-radical grafting initiator. Macromolecular Materials and Engineering, **297**, 402–410 (2012).
DOI: 10.1002/mame.201100224

[20] Miller S. A., Billington S. L., Lepech M. D.: Improvement in environmental performance of poly(β-hydroxybutyrate)-*co*-(β-hydroxyvalerate) composites through process modifications. Journal of Cleaner Production, **40**, 190–198 (2013).
DOI: 10.1016/j.jclepro.2012.08.033

[21] Hsieh Y. T., Woo E. M.: Phase diagrams in blends of poly(3-hydroxybutyric acid) with various aliphatic polyesters. Express Polymer Letters, **5**, 570–580 (2011).
DOI: 10.3144/expresspolymlett.2011.56

[22] Zhu B., Li J., He Y., Inoue Y.: Studies on binary blends of poly(3-hydroxybutyrate-*co*-3-hydroxyhexanoate) and natural polyphenol catechin: Specific interactions and thermal properties. Macromolecular Bioscience, **3**, 258–267 (2003).
DOI: 10.1002/mabi.200390036

[23] Shan G-F., Gong X., Chen W-P., Chen L., Zhu M-F.: Effect of multi-walled carbon nanotubes on crystallization behavior of poly(3-hydroxybutyrate-*co*-3-hydroxyvalerate). Colloid and Polymer Science, **289**, 1005–1014 (2011).
DOI: 10.1007/s00396-011-2412-1

[24] Xiang H., Wang S., Wang R., Zhou Z., Peng C., Zhu M.: Synthesis and characterization of an environmentally friendly PHBV/PEG copolymer network as a phase change material. Science China Chemistry, **56**, 716–723 (2013).
DOI: 10.1007/s11426-013-4837-5

[25] Yu H-Y., Qin Z-Y., Liu Y-N., Chen L., Liu N., Zhou Z.: Simultaneous improvement of mechanical properties and thermal stability of bacterial polyester by cellulose nanocrystals. Carbohydrate Polymers, **89**, 971–978 (2012).
DOI: 10.1016/j.carbpol.2012.04.053

[26] Fei B., Chen C., Wu H., Peng S., Wang X., Dong L.: Quantitative FTIR study of PHBV/bisphenol A blends. European Polymer Journal, **39**, 1939–1946 (2003).
DOI: 10.1016/s0014-3057(03)00114-9

eXPRESS Polymer Letters Vol.7, No.9 (2013) 787–804
Available online at www.expresspolymlett.com
DOI: 10.3144/expresspolymlett.2013.76

Characterisation of low-odour emissive polylactide/cellulose fibre biocomposites for car interior

C. Courgneau[1], *D. Rusu*[1*], *C. Henneuse*[2], *V. Ducruet*[3], *M-F. Lacrampe*[1], *P. Krawczak*[1]

[1]Ecole Nationale Supérieure des Mines de Douai (Mines Douai), Department of Polymers and Composites Technology & Mechanical Engineering, 941 rue Charles Bourseul, F-59508 Douai, France
[2]CERTECH (CEntre de Ressources TEchnologique en CHimie) ZI C, rue Jules Bordet, B-7180 Seneffe, Belgium
[3]INRA, UMR 1145 Food Process Engineering, 1 avenue des Olympiades, F-91300 Massy, France

Received 10 April 2013; accepted in revised form 9 June 2013

Abstract. Low odour-emissive polylactide/cellulose fibre biocomposites, intended for car interior, were prepared and characterised. The impact of the different stages of processing (drying cycles, compounding, injection moulding) on the extent of polylactide degradation and on biocomposites properties was investigated by size exclusion chromatography, thermogravimetry, differential scanning calorimetry. In parallel, the odour emission of these materials was quantified via dynamic dilution olfactometry and Field of odours® method. The changes in molecular weight and global odour emission indicated that compounding had a strong impact on polylactide degradation and odour emission, while injection moulding had no significant impact. Adding 0.5 wt% of an absorbent agent based on poly(1-methylpyrrol-2-ylsquaraine could) divide the global odour concentration by a factor 2. The morphology, mechanical and thermal properties of injection moulded PLA-biocomposites were not affected by the presence of the absorbent agent.

Keywords: *biocomposites, polylactide, cellulose fibres, odour emission, absorbent particles*

1. Introduction

These last two decades, eco-friendly composites based on natural fibres and bio-based polymers have been considered as very attractive materials for automotive parts. Indeed, subjected to regulations which impose that by 2015, 85% of vehicle components must be reused or recycled [1], Original Equipment Manufacturers (OEMs) have to provide sustainability efforts, while meeting very demanding requirements, such as high thermomechanical performance at both very short and very long terms [2, 3].

A wide range of environmentally friendly compostable polymers is actually available for automotive parts manufacturers, such as PLA, polybutylene succinate or thermoplastic starch. Among them, the thermoplastic polyester PLA has a great potential to substitute petroleum-based polymers because of its high mechanical strength and modulus, its availability in large volume and suitability as matrix for the embedding of fibres in composites. This polymer is semi-crystalline, depending on its stereochemistry and processing conditions [4–7], and suitable for a wide range of industrial processing technologies, as injection moulding, blow-moulding, thermoforming, cast film and others [8]. However, in spite of promising properties, the bio-based plastics rarely meet the very demanding requirements of automotive industry [9]. Consequently, solutions are investigated, such as fibre reinforcement, to improve their mechanical performance.

---

[*]Corresponding author, e-mail: daniela.rusu@mines-douai.fr

Many types of fibres, natural (wood, flax, hemp, kenaf…) or synthetic (glass, carbon, aramide), were associated to petroleum-based polymers and more recently to bio-based plastics [10–16].

The vegetal fibres are an interesting eco-friendly reinforcement system, as they are annually renewable, lighter, cheaper and less reliant on foreign oil sources than synthetic fibres [17]. In addition, their specific mechanical properties are close to those of glass fibres, widely used in automotive industry [2, 17, 18]. Moreover, using natural fibres to reinforce polymers matrix instead of glass fibres would make it possible to reduce the weight of composite structures, and finally the overall weight of the car. The vegetal fibres also demonstrate environmental benefits compared to glass fibres, such as ecological sustainability, low energy requirements for production, and carbon dioxide neutrality [19]. However, they have also some drawbacks such as moisture uptake, quality variation, low thermal stability, emission of volatile organic compounds (VOCs) and fogging generation [20, 21]. These sensorial defects are often assigned to the degradation of lignin, one of the major components of natural fibres among cellulose, hemicellulose, waxes and other water-soluble compounds. Actually, contrary to cellulose, which degrades above 300°C, lignin and hemicellulose are less thermo-resistant and start to degrade from 200°C [22], and even from 170°C [23] as demonstrated for flax and jute fibres. This is an issue to be considered for melt processing, as these onset decomposition temperatures fall within the typical range of processing temperatures of numerous thermoplastic polymers.

Each type of natural fibres has a specific chemical composition and so, distinct mechanical and physical properties that tune differently the biocomposites properties in which they are incorporated. Yet, almost all automotive manufacturers are already using natural fibres-reinforced petro-polymers for different car parts, i.e. seat backs, side and back door-panels, boot liners [17, 19, 24]. In the case of PLA, a wide range of vegetal fibres (flax [25, 26], kenaf [27], hemp [28], wood flour or pulp [29, 30]) was used in order to adapt the properties of PLA-biocomposites to the technical specifications for automotive applications. Generally, the mechanical properties of the matrix are greatly improved by incorporating natural fibres, whatever their type [29, 31–34]. Nevertheless, the reinforcement efficiency depends on the processing technique used to incorporate the fibres, on fibre content, as well as on the fibre orientation and aspect ratio.

Usually, the choice of the fibres for a specific automotive application depends on the balance between the cost and (local) availability, weight, mechanical features and possible issues related to the odour emission [35, 36]. This last aspect is particularly important for confined-space applications, such as cars interior, where the VOCs and odour emitted by a large variety of chemicals form the 'New Smell' of car cabins, which can lead in some cases to the 'Sick Car Syndrome'.

However, to our best knowledge, few reports are available on the reduction of the odour and VOC concentrations in small confined-spaces, despite the increasing use of biocomposites in car interior parts. Two different approaches were used by Kim and coworkers [37–39], i.e., devolatilization of VOCs by baking-out process or adding inorganic fillers. In such works, PLA degradation and mechanical performance of PLA parts were not considered.

In this context, the present study aims to prepare low odour-emissive PLA-biocomposites with interesting thermal and mechanical properties intended for car interior parts. To limit the odour emission of biocomposites, cellulose-based fibres (99.5% cellulose) were chosen to reinforce the PLA, and a recent commercially available porous system, based on poly(1-methylpyrrol-2-ylsquaraine) (PMPS), was used as potential absorbent agent.

The odour emission was examined after each processing stage of the biocomposite parts (with and without absorbent agent) and compared to neat PLA parts manufactured in similar conditions (drying, compounding and injection moulding). In addition, a comparative study of the morphology, mechanical and thermal properties of PLA and PLA-biocomposites with and without absorbent agent was also carried out.

2. Experimental

2.1. Materials

PLA pellets (PLA 4032D, NatureWorks®, Minnetonka, USA) contain about 2% of D-PLA. Highly pure cellulose fibres (ca. 99.5% cellulose) were used as reinforcing fillers (BC200, Arbocel®, J. Rettenmaier & Söhne GMBH & Co, Rosenberg, Germany). These ribbon-like fibres have an average length and thickness of 300 and 20 μm respectively. The absorbent agent for VOCs (µ-Sq beads, Exilica Limited, Coventry, United Kingdom) is based on poly(1-methylpyrrol-2-ylsquaraine (PMPS). These particles (average diameter $\overline{\phi}$ = 1.92 µm) are expected to absorb chemical entities due to their internal amorphous porous network.

2.2. Preparation of biocomposites samples: Compounding and injection moulding

Figure 1 presents schematically the entire processing cycle. Prior to processing, the PLA pellets and the absorbent agent powder were dried at 80°C for 22 h in a vacuum oven (Vacucell VU111, Avantec, Illkirch, France), to remove the moisture. The cellulose fibres were dried at 115°C for 24 h, in a standard oven (SR2000, Thermosi, France). PLA-biocomposites with 10 wt% of cellulose fibres were prepared using a twin-screw extruder (BC45, Clextral, Firminy, France), equipped with screws having *L*/*D* ratio of 25 and diameter of 50 mm. In the case of PLA-biocomposites with 10 wt% cellulose fibres (8.4 vol%) and 0.5 wt% absorbent agent, a dry blending of the cellulose and absorbent powder was first performed, and then the blend was incorporated into the PLA by melt processing, as described above. In all cases, the temperature profile (6 zones) along the extruder, from hopper to die end, was maintained as 170–170–170–170–180–180°C, for a screws speed of 110 rpm. The residence time in extruder was of about 6–7 min. Neat PLA samples were extruded in the same conditions, for comparison purpose. The extrudates were cooled through a 0.8 m long water-bath, then granulated and submitted to a second drying cycle under vacuum at 45°C for the first 15 h, and then at 80°C for 72 h. Once dried, the pellets of compounded neat PLA and PLA-biocomposites were injection moulded in bars and dumbbell-shaped specimens by using an injection moulding machine (KM80-160E, Krauss-Maffei, Munich, Germany). The injection moulding temperature was kept constant at 180°C and the injection moulding flow rate was set at 63 cm^3/s. The holding stage was carried out in three steps of 15 s, at 950, 750 and 500 bars. The mould temperature was kept at 30°C.

The samples are denoted as PLA for neat PLA, PLA10F for PLA-biocomposite with 10 wt% of cellulose fibre, and PLA10F05Ex for biocomposite with 0.5 wt% of absorbent agent. The codes –C and –CI added to the sample names stand for compounded samples and compounded/injection moulded samples, respectively. The codes d and nd indicate whatever the sample under study is dried or not.

2.3. Characterization methods

2.3.1. Moisture analysis

Moisture content of raw materials and intermediary products was determined by Karl-Fisher method, with a Karl-Fisher volumetric titrator (V30, Mettler Toledo, France). The samples were heated to 150°C for 30 min under dried nitrogen gas flow of 40 mL/min within the drying oven. The concentration of the reagent was determined with sodium tartrate dihydrate. Three replicates were analyzed for raw materials and intermediate products.

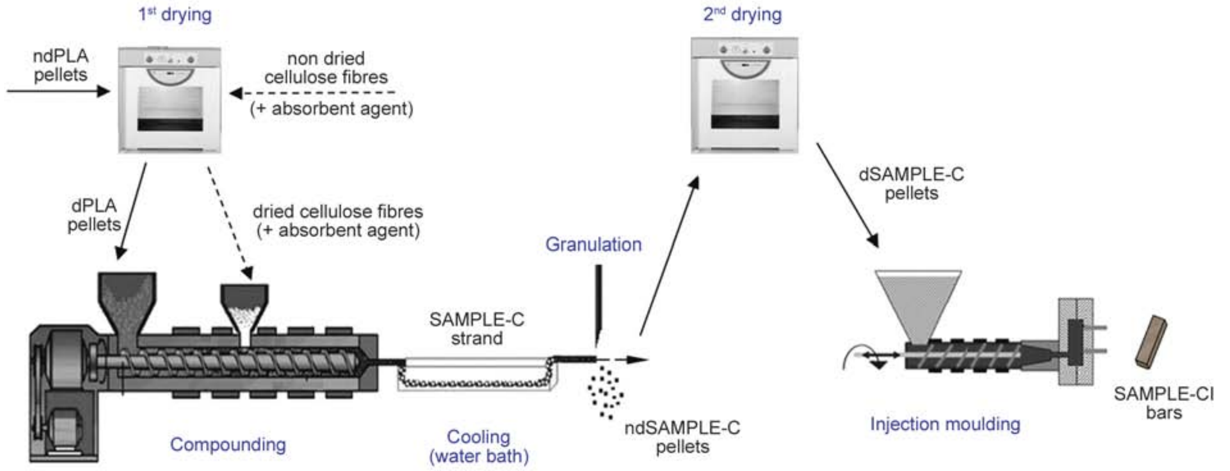

Figure 1. Schematic representation of different processing steps to obtain injection moulded parts. In this work, SAMPLE means either neat PLA or PLA-biocomposites without or with absorbent agent (PLA10F and PLA10F05Ex, respectively)

2.3.2. Fibre content of PLA-biocomposites

PLA-biocomposite pellets were dissolved in chloroform (5 g in 200 mL) for 90 min. The suspension was then filtered over a Büchner funnel equipped with a paper filter (Macherey-Nagel GmbH & Co. KG, Düren, Germany) with pore size 4–12 µm, to remove the cellulose fibres and, respectively, the cellulose fibres/absorbent agent particles and to collect them. Once washed with chloroform, the residue was dried in oven (BM 40, Memmert, Germany) at 70°C for 24 h, until constant weight. The solid residue was weighted to calculate the fibre and fibre/absorbent agent content in PLA-biocomposites. Three replicate tests were done for PLA and PLA-biocomposite pellets.

2.3.3. Scanning electron microscopy (SEM)

SEM micrographs were made from cryo-fractured surfaces of injection moulded bars from PLA-biocomposites and neat PLA samples. The biocomposites morphology, the dispersion effectiveness and the adhesion quality between cellulose fibres and respectively absorbent agent and the PLA matrix were investigated using a scanning electron microscope (S-4300SE/N, Hitachi, Tokyo, Japan) with field emission gun and accelerating voltage of 15 kV. Prior to observation, the fracture surfaces were coated with a thin gold layer, using a sputter coater (SEM Coating System, Polaron, Watford, United Kingdom).

2.3.4. Melt flow index (MFI)

PLA and biocomposite pellets were dried at 80°C for 22 h, in a vacuum oven (Vacucell 111VU111, Avantec, Illkirch, France), prior to melt flow index measurements. The MFI experiments were performed on a MFI apparatus (NG-M, Göttfert, Buren, Germany) at 190°C and 2.16 kg mass, according to NF T 51-016 standard. After a pre-heating period of 240 s, samples were collected every 30 s. The MFI was calculated as an average of 20 values and expressed in g/10 min.

2.3.5. Size exclusion chromatography (SEC)

The average molecular weights ($\bar{M}_n$, $\bar{M}_w$) and polydispersity index ($Đ = \bar{M}_w/\bar{M}_n$) of PLA were determined at room temperature by size exclusion chromatography in chloroform. In the case of biocomposites, the cellulose fibres were first extracted and the SEC measurements were performed on diluted PLA solutions obtained from filtrates. The SEC system consisted of a HPLC pump (Waters Alliance 2690 Separation Module, Waters Corp., Milford, Massachusetts, USA) and a differential refractometer (Waters 2414 Refractive Index Detector, Waters Corp., Milford, Massachusetts, USA). The flow rate was 1 mL/min. A set of columns (Waters Styragel HR4E and HR5E, Waters Corp., Milford, Massachusetts, USA) covering the molecular weight range between 100 and 4 000 000 g/mol was used. Calibration was performed using narrow distributed polystyrene standards and the sample chromatograms were processed with SEC-Waters software.

2.3.6. Thermo-gravimetric analysis (TGA)

The thermal stability of samples was determined with a thermogravimetric analyzer (Q500 TGA, TA Instruments, New Castle, USA). The tests were performed on 5–10 mg samples from 30 to 580°C with Hi-Res dynamic mode at 10°C/min (sensitivity 1.0, resolution 4.0) under a nitrogen purge. The percent weight loss and derivative weight loss were plotted against temperature in order to evaluate $T_{5\%}$, $T_{50\%}$, $T_{95\%}$ and $T_{\max}$, defined as temperatures at which 5, 50 and 95% of the total mass is volatilized, and respectively the temperature of the maximum rate of weight loss of the PLA samples. Three replicates were scanned for the PLA pellets as received and after drying, as well as for each neat PLA and biocomposite sample.

2.3.7. Differential scanning calorimetry (DSC)

The thermal behaviour of the PLA raw material, processed neat PLA and PLA-biocomposites were examined with a differential scanning calorimeter (DSC 8500, Perkin-Elmer, Waltham, USA) equipped with a Dewar tank (CryoFill, Perkin-Elmer, Waltham, USA). Indium was used as standard calibration material. The samples (ca. 8 mg) were heated from 0 to 190°C, with a heating rate of 10°C/min, under nitrogen flow. The glass transition temperature was taken as the midpoint of the heat capacity change. The cold crystallization and melting temperatures and heats were determined from the maxima and areas of the crystallization and melting peaks, respectively. The crystallinity degree (χ_c) was calculated according to Equation (1):

$$\chi_c = \frac{\Delta H_m - \Delta H_{cc}}{\Delta H_m^{100\%}} \cdot \frac{100}{1 - \omega_f} \tag{1}$$

where ΔH_m and ΔH_cc are the heat of melting and cold crystallization of the PLA and biocomposites, $\Delta H_\mathrm{m}^{100\%}$ is the heat of melting for 100% crystalline PLA (93 J/g) [40] and ωf is the content of fibre and absorbent agent in PLA-biocomposites.

2.3.8. Mechanical properties

The uniaxial tensile tests were performed on dumbbell-shaped specimens according to ISO 527-2, at room temperature, using a standard testing machine (LR 50K, Lloyd, Bognor Regis, United Kingdom) with a load cell of 5 kN. A crosshead speed of 10 mm/min was used for measuring the strength and elongation at break, and the tensile strength at yield. The Young moduli were measured with an extensometer (Model 2620-602, Instron, USA), at 1 mm/min. The Charpy unnotched impact strengths were measured on injection moulded bar specimens with dimensions 80×10×4 mm^3, using a impact tester (D7900, Zwick GmbH & Co. KG, Ulm, Germany) equipped with an impact hammer of 7.5 J. At least 10 specimens were tested for each injection moulded biocomposite and neat PLA, after conditioning at 23°C (50% RH) for one week at least.

2.3.9. Global odour analysis

In order to analyze the impact of each processing stage on the global odour of neat PLA and PLA-biocomposites, samples were collected in glass bottles as following:

- before compounding:dried raw materials (dPLA pellets and cellulose fibres);
- after compounding/granulation/2$^\mathrm{nd}$ drying: dried pellets of compounded PLA and PLA-biocomposites (dPLA, dPLA10F-C and dPLA10F05Ex-C, respectively);
- after compounding/granulation/2$^\mathrm{nd}$ drying and injection moulding: bars of PLA-CI, PLA10F-CI and PLA10F05Ex-CI.

Two types of sensory analyses were performed: odour description by means of the 'Champ des Odeurs®' method, and odour measurements by dynamic dilution olfactometry.

The 'Champ des Odeurs®' (Field of odours) method [41] was applied by six trained experts, who described qualitatively and quantitatively the global odour emitted by PLA, cellulose fibres and PLA-biocomposites. The analyses were performed according to ISO5496, on a series of samples of about 100 g placed in 10 L sampling bags (Tedlar® polyvinyl fluoride bags, DuPont™, Chapel Hill, USA) with pure air, and preconditioned for 2 hours at 90°C. More than 45 descriptors (reference molecules diluted in alcohol) are used to characterise the odours and can be seen as the alphabet used to analyse and describe odours. These analyses involve basically experts, also named panellists (10 people). They gather together at least once a week for one or two hours training and working session. During each session, their individual recognition scores are tested and monitored in order to obtain individual and panel recognition scores.

The second approach consists on measuring the odour concentration emitted by materials, by means of dynamic dilution olfactometry, which is a standardized method (EN13725) commonly used for quantifying odours. The analyses were performed on a set of samples of about 400 g placed in 40 L Tedlar® sampling bags with pure air, with the same loading factor (10 g/L) and preconditioning (90°C for 2 hours) as for the Field of odours® method. A dilution olfactometer presented then a series of odour samples diluted with pure air at precise ratios, to a panel of six panellists, representative of the population. The dilution factor necessary to reach the odour threshold for a given sample (i.e., the minimum concentration perceived by 50% of panellists) represents the odour concentration of that sample and is expressed as $\mathrm{ou_E.m^{-3}}$. The reference gas used for evaluating the sensory perception threshold is n-butanol.

3. Results and discussion

3.1. Moisture content

The moisture content of PLA materials was measured before/after each processing stage. The results are presented in Table 1. The drying protocol appeared to be effective on PLA and PLA-biocomposites. For instance, the residual water content of neat dPLA and dPLA-C approached the recommended value from the PLA producer (i.e. 250 ppm), while in presence of 10 wt% of dried cellulose fibre, the moisture content was reduced to 480–640 ppm.

3.2. Cellulose fibre content

The extraction of cellulose fibres by dissolution in chloroform indicates the cellulose fibres content in PLA based biocomposite: ca. 9.7% in PLA-biocomposite and 10.9% in PLA/fibre/absorbent agent bio-

Table 1. Moisture and solid content, number (M_n) and weight (M_w) average molecular weight, polydispersity index (*Đ*) and melt flow index (MFI) of PLA and PLA-biocomposites, at different moments of the processing cycle

Sample codes	Moisture content [ppm]	Solid content* [%]	M_n [g/mol]	M_w [g/mol]	Đ	MFI [g/10 min]
Samples based on neat PLA						
ndPLA pellets	3600	ND.	108 500	236 000	2.2	8.2±1.5
dPLA pellets	270	ND.	112 500	234 000	2.1	3.8±0.3
ndPLA-C pellets	2110	ND.	105 000	219 500	2.1	ND.
dPLA-C pellets	260	0.1±0.1	94 000	205 500	2.2	5.8±0.3
PLA-CI bars	ND.	ND.	90 000	203 000	2.3	ND.
Samples based on PLA-biocomposites (PLA + 10 wt% cellulose fibres)						
ndPLA10F-C pellets	5720	ND.	93 500	192 500	2.1	ND.
dPLA10F-C pellets	640	9.7±0.5	87 000	176 500	2.0	6.2±0.3
PLA10F-CI bars	ND.	ND.	81 000	171 500	2.1	ND.
Samples based on PLA-biocomposites with an odour remediation agent (PLA + 10 wt% cellulose fibres + 0.5 wt% absorbent agent)						
ndPLA10F05Ex-C pellets	3240	ND.	96 000	188 000	2.0	ND.
dPLA10F05Ex-C pellets	480	10.9±0.2	81 500	174 500	2.1	5.8±0.2
PLA10F05Ex-CI bars	ND.	ND.	75 500	165 000	2.2	ND.

*cellulose fibres or cellulose fibres + absorbent agent
nd = non dried (sample); d = dried (sample)
–C = after compounding; –CI = after compounding/injection moulding cycle
ND. = non determined

composites containing 0.5% absorbent particles. These observations confirm that the feeding system worked properly with low-density materials. Secondly, the good repeatability over three replicates taken at different compounding times suggests that the cellulose fibres and absorbent particles were macroscopically homogeneously dispersed in the PLA matrix.

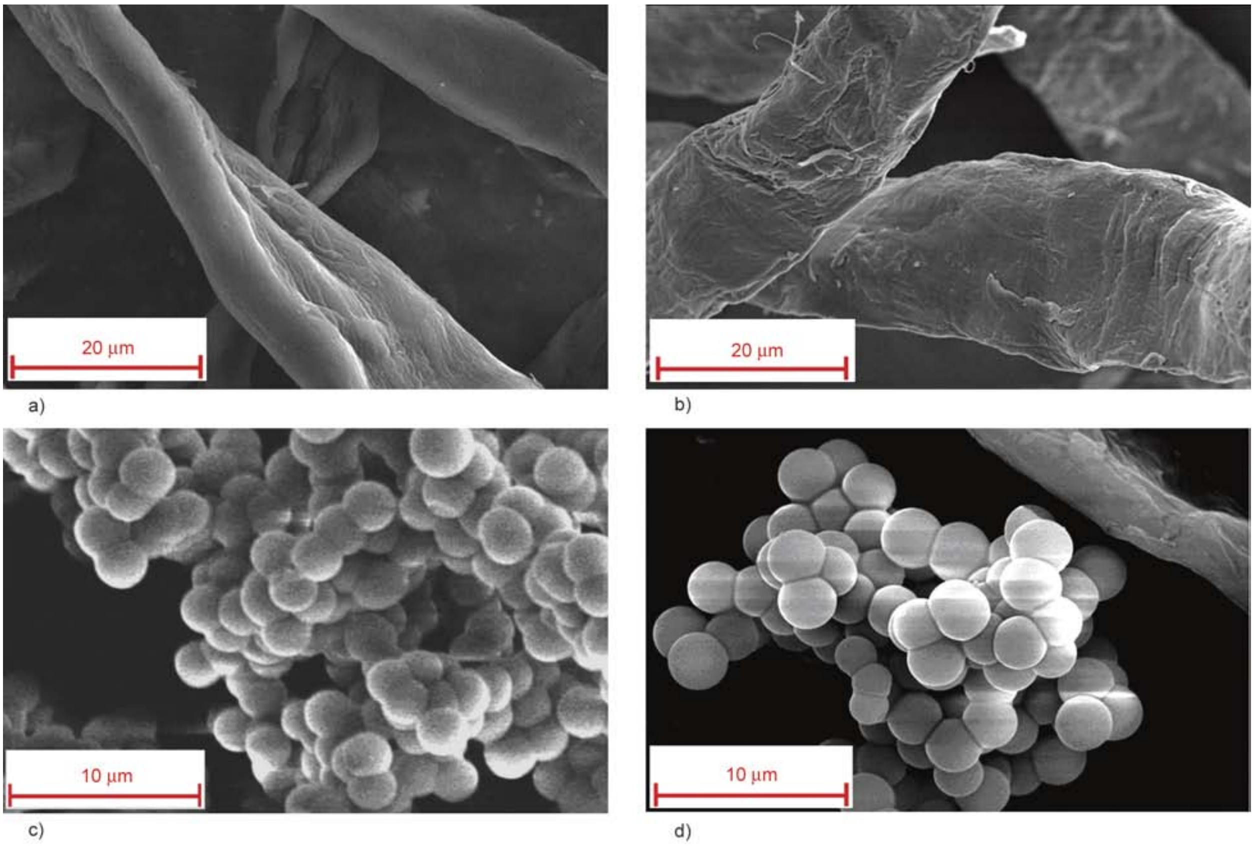

Figure 2. SEM micrographs of cellulose fibres (a, b) and particles of absorbent agent (c, d) before and after drying

3.3. Morphology of PLA-biocomposites

Figure 2 displays the SEM micrographs of cellulose fibres and absorbent particles, before and after drying stage. The cellulose fibres present a rather smooth surface (Figure 2a, 2b). The absorbent spherical particles, which form large agglomerates up to 40–50 μm, keep the same organization and their structure appears unaffected by the drying process (Figure 2c and 2d).

Analysis of the micrographs of cryo-fractured surfaces of injection moulded neat PLA shows neither crazes nor fibrils, confirming the brittle fracture of the well-frozen structures (Figure 3a and 3b).

Figure 3c and 3d reveal a good dispersion of individual cellulose fibres in PLA matrix and confirm the effectiveness of the compounding stage.

The cryo-fractured surfaces of biocomposites display voids and interfacial debonding between cellulose fibres and PLA matrix, as well as fibre pull-out effects (Figures 3d, 3e, 3f, 3g). These observations indicate a poor adhesion between most of the fibres and the PLA matrix, despite the possible hydrogen bonds that might be formed between the slightly polar oxygen of PLA and the hydroxyl groups of cellulose [32, 42]. Similar behaviour had been reported by Huda *et al.* [43] for PLA-biocomposites at 30 wt% of vegetable fibres with a minimum of 75% of cellulose.

In the case of PLA-biocomposites with 0.5 wt% absorbent particles, SEM micrographs obtained at 500× to 2000× magnification (examples in Figure 3f and 3g) indicate the absence of large agglomerates of absorbent agent inside the polymer matrix. At higher magnifications (i.e., 5000× – Figure 3h), micro-agglomerates of absorbent agent (with less than ten particles) can be seen homogeneously distributed inside the matrix. This means that the compounding step is effective in breaking the initial large agglomerates of absorbent agent into smaller micro-agglomerates, and well dispersing them in the PLA matrix. On the other hand, voids are visible around absorbent particles, which indicate a rather poor adhesion to the PLA matrix.

3.4. MFI

Table 1 lists the MFI values for virgin PLA pellets before and after drying, and for dried pellets of neat PLA and PLA-biocomposites after compounding.

The MFI of the non dried (as received) PLA pellets (8.2 g/10 min) is much higher as compared with the dried pellets (3.8 g/10 min), because of the hydrolysis of polyester chains during the pre-heating stage at high temperature (190°C for 240 s), in presence of moisture (0.36%). The MFI of dried PLA pellets obtained by compounding at 190°C for 6 min, and granulation ($\mathrm{MFI}_{\mathrm{dPLA\text{-}C}}$) is higher than for initial dried pellets ($\mathrm{MFI}_{\mathrm{dPLA}}$), which corresponds to a decrease in the melt viscosity of compounded PLA, indicating a decrease in its molecular weight. This suggests that the compounding stage induced some random chain scission in PLA, most probably by a thermo-mechanical mechanism, since no water molecules were present to favour polyester hydrolysis. Van den Oever *et al*. [44] found similar tendency for dried PLA with 4–8% of D-lactide compounded at 175°C for 15 min in a batch kneader. Unexpectedly, the MFI of dried pellets of PLA-biocomposites obtained after compounding/granulation ($\mathrm{MFI}_{\mathrm{dPLA10F\text{-}C}}$) is close to $\mathrm{MFI}_{\mathrm{dPLA\text{-}C}}$. Indeed, adding 10 wt% of dried cellulose fibres in PLA was expected to increase the material viscosity, and so, to decrease the MFI value as shown for ramie, flax or cotton fibres in PLA [44]. It seems that in the present case, the increase in viscosity due to the presence of short cellulose fibres is compensated by the decrease due to the reduction in molecular weight of PLA, because of degradation.

The addition of fine powder (0.5 wt%) of absorbent agent does not change the MFI value of the dried PLA-biocomposites after compounding ($\mathrm{MFI}_{\mathrm{dPLA10F05Ex\text{-}C}} \approx \mathrm{MFI}_{\mathrm{dPLA10F\text{-}C}}$), which means that this absorbent agent plays no particular role in the degradation mechanism of PLA, neither to prevent nor to enhance the chain scission.

3.5. Molecular weight

The SEC results are presented in Table 1. The molecular weight variations of 5–10% were in our range of experimental error of SEC, however, some tendencies can be identified.

First, one can see that the *drying stage* of (as received) PLA pellets does not change the average molecular weight of the polymer.

Secondly, *compounding* dried neat PLA results in a decrease in both M_n and M_w values, without affecting the polydispersity index $Đ$ or the molecular weight distribution (not shown here). The decreasing tendency of PLA molecular weight after compounding/granulation/drying stages is confirmed by the MFI evolution between dPLA (3.8 g/10 min)

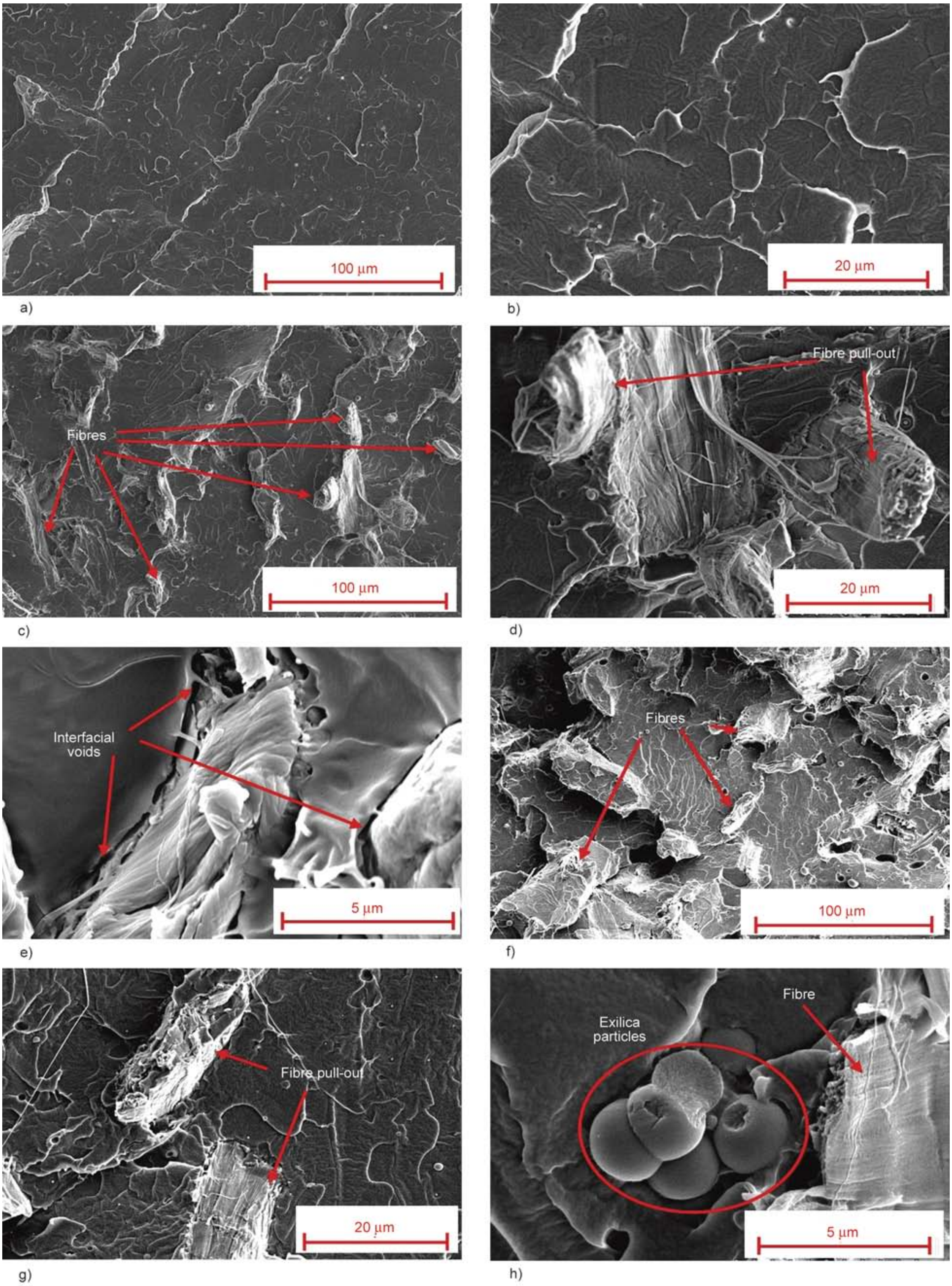

Figure 3. SEM micrographs of the cryo-fractured surfaces of injection moulded neat PLA-CI (a, b), and PLA-biocomposites, without (PLA10F-CI, c, d, e) or with absorbent agent (PLA10F05Ex-CI, f, g, h)

and dPLA-C (5.8 g/10 min). These observations are in agreement with the results of Wang *et al*. [45], who found a decrease in the M_n of dried PLA, more or less important depending on the applied compounding temperature (–4% at 180°C and –35% at 200°C), for a same low screw speed (100 rpm).

A more careful investigation of the molecular weight evolution before and after *the passage through the twin-screw extruder*, followed by *cooling in a water bath* and *granulation*, showed that these processing stages are responsible only for a part of PLA degradation (M_n: –7%, M_w: –6%). In fact, an additional molecular weight loss (M_n: –10%, M_w: –6%) occurs during the *post-compounding drying step* (15 h at 45°C, followed by 72 h at 80°C, under vacuum), most probably caused by hydrolysis due to the high moisture contents (up to 0.6%) acquired by the compounded materials during the cooling step in a water bath, at the exit of the extruder. It appears that this inevitable drying stage should be optimised, to limit the risk of further PLA hydrolysis at 80°C.

The *incorporation of 10 wt% of dried cellulose fibres* into PLA causes a further decrease in M_n (–7%) and M_w (–14%) values with respect to neat PLA after compounding, meaning that the PLA degradation is enhanced in presence of fibres. This further degradation of PLA when adding the filler is also confirmed by MFI (from 5.8 to 6.2 g/10 min), even if the expected increase in MFI due to PLA degradation is largely hidden by the presence of 10 wt% of cellulose fibres.

This evolution may be explained, on one hand, by the PLA hydrolysis in the presence of water molecules brought by the cellulose fibres. Indeed, the dried cellulose fibres, with 0.6 wt% residual water after the drying process, exhibit quite fast water uptake kinetics (about 2 wt% in 15–30 min), which implies that even short-time manipulations of cellulose fibres during processing result in some water uptake. To limit the effect of this extra-water content brought into PLA matrix, the twin-screw extruder has a degassing zone placed after the mixing zone, and a vacuum pump is connected to extract water vapours. Nevertheless, the remaining humidity, once released inside the co-extruder, can generate some hydrolysis of PLA chains and so, a decrease in molecular weight. On the other hand, adding 10 wt% of cellulose fibres also induces an increase in melt viscosity, and so it generates higher shear stresses during the compounding process, which can result in thermo-mechanical degradation of PLA.

Finally, the *injection moulding* did not induce further significant degradation, as shown by the minor decrease in M_n and M_w values (less than 5%, as compared to the compounded pellets). Same tendency is observed for the neat compounded PLA and the cellulose fibre/PLA biocomposites, with and without absorbent agent. These observations confirm the necessity to apply an effective post-compounding drying stage, for limiting the degradation during injection moulding process. This statement is also supported by comparing the results reported in this study with those of Carrasco *et al*. [46] and Pillin *et al*. [47], for injection moulding of virgin PLA pellets. In the first case, an important decrease of molecular weight (M_n: –30%, M_w: –19%) was reported after the injection moulding of well-dried PLA2002D (ca. 4% D-lactide, moisture close to zero), at a temperature profile of 180–200–210°C. An injection moulding temperature higher than that used in the present study (170–180°C) can justify more important polymer degradation. In the second case, Pillin *et al*. [47] reported a decrease in M_w of about –17% during the injection moulding of PLA L9000 (ca. 8% D-lactide, and 0.5% residual moisture), at a temperature profile of 175–180–185–190°C close to the one used in the present study (170–180°C). The important moisture content of PLA pellets used by Pillin *et al*. [47] would have favoured noticeable hydrolysis of polyester chains during injection moulding. These two comparisons confirm the important role of processing conditions, as well as residual moisture content and PLA stereochemistry, in the extent of polyester degradation during melt processing.

The presence of a low content of absorbent fine powder in PLA-biocomposite did not influence the molecular weight of PLA, which proves that, at least for low contents (≤0.5 wt%), this absorbent agent neither prevents nor enhances the PLA degradation mechanism by chain scission.

3.6. Thermal stability

Figure 4a shows the influence of the different processing steps on the thermal stability of the neat PLA. The TGA/DTG thermograms are almost identical, for dried initial PLA pellets, compounded PLA pellets and injected PLA bars, and indicate a one-step decomposition process occurring within a narrow temperature range, 320–340°C. The characteristic degradation temperatures at which 5, 50 and 95% of the total mass is volatilized ($T_{5\%}$, $T_{50\%}$, and $T_{95\%}$) and the temperature of the maximum rate of weight loss (T_{max}) are listed in Table 2.

Table 2. Characteristic temperatures of thermal degradation of cellulose fibres, PLA and PLA-biocomposites

Samples	$T_{5\%}$ [°C]	$T_{50\%}$ [°C]	$T_{95\%}$ [°C]	T_{max} [°C]
dried Cellulose fibres	264±2	322±1	–	323±1
ndPLA	319±2	323±1	327±1	323±1
dPLA	321±2	328±1	337±3	327±1
dPLA-C	323±1	327±1	336±1	327±1
PLA-CI	321±1	327±1	333±1	327±1
dPLA10F-C	316±1	320±1	351±4	319±1
PLA10F-CI	314±1	321±1	349±2	320±1
dPLA10F05Ex-C	313±3	318±3	359±4	317±3
PLA10F05Ex-CI	315±1	319±1	365±1	318±1

Mean±standard deviation

As shown by the thermograms, there is no noticeable influence of melt processing on well-dried PLA pellets. These results show that the thermal stability of PLA with 2% of D-units is not so sensitive to the small decrease in its molecular weight (up to –14%, as seen in the previous section).

A different trend was reported by Carrasco *et al*. [46] for PLA2002D after extrusion and injection moulding, i.e., a slightly shift of $T_{5\%}$, more sensitive to the drop of molecular weight, as a result of processing. This difference might be due to the higher injection temperature used by Carrasco *et al*. [46], which induced a decrease in molecular weight of PLA.

Figure 4b presents the TGA/DTG thermograms of cellulose fibres and PLA-biocomposites. Despite an effective first drying of the cellulose fibres, that decreased their moisture content from 7.5 to 0.6%, the TGA curve indicates a first weight loss in the temperature range from 30–110°C, which is most probably due to water evaporation. Indeed, as mentioned previously, the water uptake kinetics is rather fast (about 2 wt% in 15–30 min), and may explain at least in part, this first weight loss process. However, the main stage of weight loss of the cellulose fibres occurs between 180 and 410°C, and corresponds to cellulose decomposition in volatile molecules such as carbon monoxide and dioxide, water, methane, ethane [22, 48].

The thermal degradation of PLA-based biocomposites occurs in one-stage process. The addition of cellulose fibres in PLA matrix mainly results in slight decrease in the onset decomposition temperature ($T_{5\%}$) from 321 to 316 and 314°C after compounding and compounding/injection moulding, respectively. A similar trend is noticed in $T_{50\%}$, from 327 to 320 °C, after compounding, and without any further significant changes after injection moulding. It is in agreement with the results reported by Pan and Inoue [55], which indicated a drop of 4°C of $T_{50\%}$ with 10 wt% of kenaf in PLA, after compounding and injection moulding.

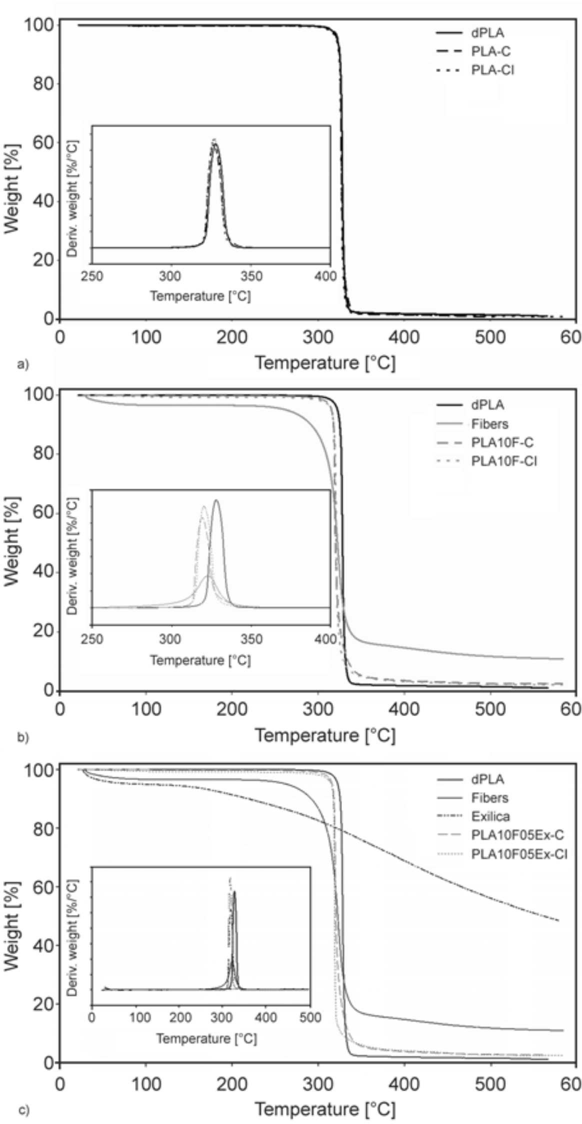

Figure 4. TGA/DTG thermograms of materials at different stages of processing: raw materials, pellets after compounding/2nd drying, and bars obtained by injection moulding: (a) processing of neat PLA; (b) preparation and processing of PLA10F biocomposite; (c) preparation and processing of PLA10F05Ex biocomposite

The addition of a low amount of absorbent agent (0.5 wt%) in biocomposites does not affect in a significant manner the thermal stability of compounded biocomposite pellets (Figure 4c). Similarly, no effect of the injection moulding process is noticed for cellulose/PLA/absorbent agent system.

3.7. Thermal properties

The thermal characteristics such as glass transition temperature (T_g), cold crystallization temperature (T_{cc}), crystallization enthalpy (ΔH_{cc}), melting temperature (T_m), melting enthalpy (ΔH_m) and crystallinity degree (χ_c) obtained from DSC studies are summarized in Table 3. The PLA *pellets, as received*, show a T_g at 61.7°C, a melting peak at 165.9°C, without cold crystallization and a crystallinity degree of 46%. The drying process of the pellets at 80°C for 22 h results in a broadening of glass transition and a slight increase of the T_g up to 64.0°C, without modifying the melting temperature and crystallinity degree (Figure 5a). According to Magoń *et al.* [49] and Zuza *et al.* [50], this increase in the T_g value may be due to the confinement of the mobile amorphous phase fraction (MAF) [51, 52]. Indeed, a three phases model (mobile amorphous, rigid amorphous and crystalline phases) can be used to explain the glass transition dynamics. Contrary to the rigid amorphous phase fraction (RAF), which cannot contribute to the glass transition due to the partial trapping of the molecules in the crystalline lamellae, the MAF, sensitive to the constrains in the matrix, relaxes at the glass transition temperature. This phenomenon is observed in the present case for compounded PLA pellets (ndPLA-C) submitted to drying at 80°C for 72 h. The second drying step acted as an isothermal cold crystallisation cycle [53], and the amorphous ndPLA-C pellets crystallised up to 37%. The implicit confinement of the MAF results in a large broadening and shift of the T_g, from about 54°C (for amorphous ndPLA-C pellets) to about 62°C (for semi crystalline dPLA-C pellets). These results are in agreement with data reported by Guinault *et al.* [54] for the crystallization of PLA 2002D at 85°C (4.3% of D-lactide).

As expected, the DSC analysis reveals that the PLA pellets obtained after compounding and granulation (ndPLA-C pellets) are mainly amorphous ($\chi_c \leq$ 3%), due to the fast cooling stage in the water bath at 20°C. The post-injection moulding cooling stage is short as well, and the slow crystallization kinetics of PLA at that temperature gradient does not allow the development of crystalline zones. Consequently, the crystallinity degree of PLA-CI bars is below 5%, and the T_g around 55°C. As shown in Figure 5a, the amorphous pellets of compounded PLA and the PLA bars present similar cold crystallization temperatures (≈105°C). However, these two samples

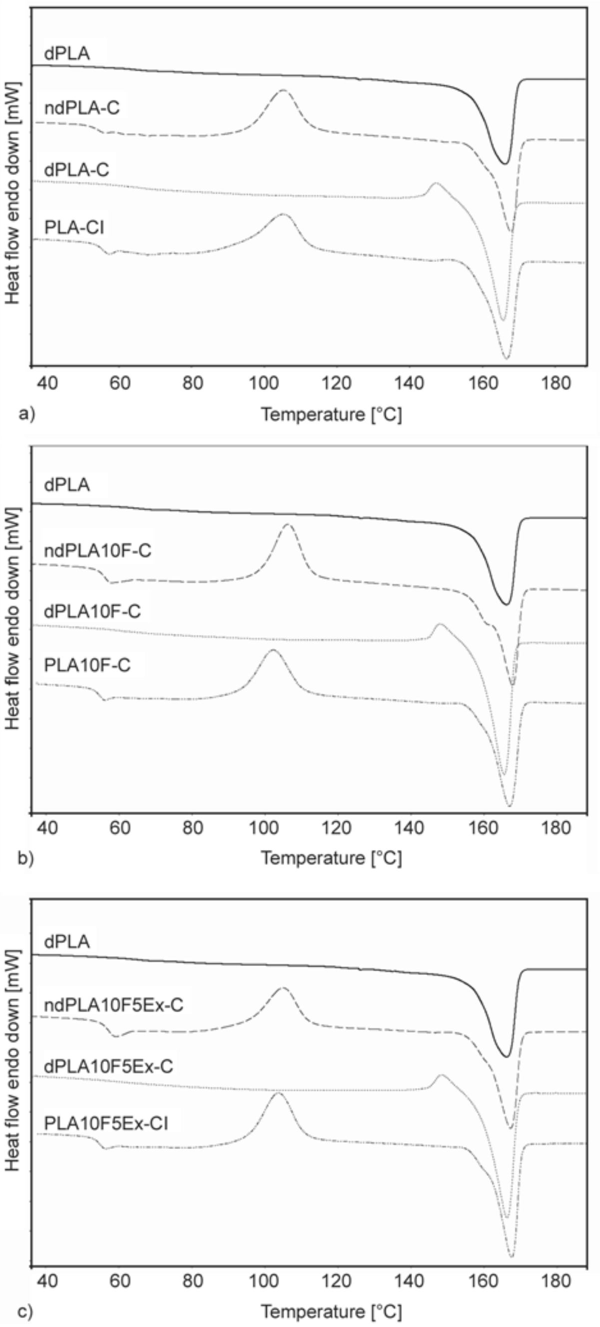

Figure 5. a) DSC thermograms of dPLA pellets, PLA-C pellets and PLA-CI bars, b) DSC thermograms of dPLA pellets, PLA10F-C pellets and PLA10F-CI bars. c) DSC thermograms of dPLA pellets, PLA10F05Ex-C pellets and PLA10F05Ex-CI bars

exhibit different melting behaviour: the ndPLA-C pellets resulted from compounding and granulation present a melting peak at 167.8°C with a shoulder (160.9°C), whereas after injection moulding, the PLA-CI materials shows an exotherm at 150.4°C, before the melting endotherm peak at 166.6°C. As explained by Pan and Inoue [55], and also observed by Courgneau *et al.* [53], this exotherm prior to the

Table 3. Thermal properties of PLA and PLA-biocomposites

Samples	T_g [°C]	T_{cc} [°C]	ΔH_{cc} [J/g]	T_m [°C]	ΔH_m [J/g]	χ_c [%]
ndPLA	61.7±1.5	–	–	165.9±0.8	41.9±1.4	46±1
dPLA	64.0±0.2	–	–	165.6±0.8	42.5±0.8	46±2
ndPLA-C	53.8±0.1	105.2±0.1	31.7±0.2	167.8±0.1 160.9±0.1*	34.0±0.9	2±1
dPLA-C	62.4±1.3	–	–	165.5±0.2	39.4±0.3	37±1
PLA-CI	55.0±0.3	105.1±0.3	31.4±0.7	166.6±0.1	34.5±0.5	3±1
ndPLA10F-C	55.4±0.5	106.3±0.1	30.8±0.3	168.1±0.4 161.1±0.2*	36.4±0.1	2±1
dPLA10F-C	62.4±0.8	–	–	165.9±0.4	31.4±0.3	37±1
PLA10F-CI	53.8±0.1	102.6±0.5	29.6±0.5	167.2±0.2 159.8±0.2*	35.7±0.1	4±1
ndPLA10F05Ex-C	55.9±0.1	104.5±0.8	29.0±0.3	167.4±0.2 160.0±0.1*	33.6±0.7	3±1
dPLA10F05Ex-C	62.5±0.3	–	–	166.0±0.4	33.0±0.6	37±1
PLA10F05Ex-CI	53.9±0.3	103.4±0.6	29.9±0.9	167.6±0.1 159.9±0.7*	33.1±0.4	4±1

Mean±standard deviation
*shoulder of endotherm peak.

endotherm peak is due to the rearrangement of the instable crystalline form (α′) of PLA into the stable crystalline form (α). The shoulder on the endotherm, already reported for neat PLA [33] and PLA/20 wt% hemp [28], can be explained by three main mechanisms, namely melt-recrystallization, dual lamellae population [28], and dual crystal structure [33].

The DSC thermograms of biocomposites with or without absorbent agent (Figure 5b and 5c) are similar to those of neat PLA. The data related to these thermograms are summarised in Table 3.

As noticed for neat PLA, drying the biocomposites pellets after compounding (i.e., drying ndPLA10F-C and ndPLA10F05Ex-C pellets) increases their crystallinity degree up to 37%, and probably induces the confinement of the mobile amorphous phase, as suggested by an increase in T_g and a broadening of the signal. The presence of cellulose fibres and 0.5 wt% fine absorbent microparticles in PLA generates a slight variation of T_{cc}, without significant changes in melting temperatures values (Table 3).

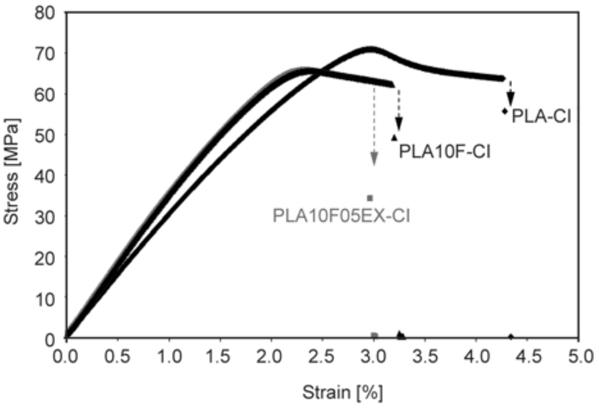

Figure 6. Stress-strain curves of neat PLA and PLA-based biocomposites

3.8. Mechanical properties of the biocomposites

Figure 6 presents the stress-strain curves of neat PLA and PLA-biocomposites. It is clearly shown that the tensile properties of injection moulded PLA and PLA-based biocomposites are close. Neat PLA specimens fracture suddenly after the yield point, without observing neck, which indicates the brittle behaviour of PLA. The addition of cellulose fibres does not modify the brittle behaviour of PLA. The stresses at break remain similar, ca. 63 MPa, whereas a slight increase in Young modulus and a slight decrease in the elongation at break is noticed with the incorporation of 10 wt% of cellulose fibres. This trend is commonly observed with biocomposites PLA/natural fibres [43, 56, 57]. As shown in Table 5, at similar content of hemp fibres in PLA, Masirek *et al.* [28] noticed a decrease in the elongation at break (–38%) and in the strength at yield (–23%). The kenaf fibres/PLA-biocomposites also showed a drop of these mechanical characteristics [33]. This general feature is due to the poor adhesion between natural fibres and PLA, which was pointed out in Figure 3, for the highly pure cellulose fibres. The existence of voids between the fibres and the PLA matrix prevents an effective stress transfer to the fibres, resulting in low strength values. Nevertheless, others factors may influence the mechanical properties, including PLA intrinsic properties (stereochemistry, molecular weight) and microstructure (crystallinity, preferentially chain orientation…), as well as fibres characteristics (chemical composition, mechanical properties, size and aspect ratio), and finally, parameters related to the volume fraction of fibres and their orientation in biocomposites. Adding 8.4 vol% (10 wt%) of highly pure cellulose fibres in PLA (Tables 4 and 5) increases the Young modulus (+18%). Huda *et al.* [43] showed similar increase for PLA with 10 wt% of cellulose fibres from newspaper/magazine or kraft paper. A higher increase in rigidity, ca. 25%, was found by Bax and Müssig [32] for PLLA with 10 wt% of flax fibres. Hence, the incorporation of fillers in polymer matrix increases its stiffness by restraining the chain movement and because of the high stiffness of cellulose [59].

The Charpy impact strength values of neat PLA and PLA-based biocomposite are reported in Table 4. Adding 10 wt% of cellulose fibres in PLA leads to a decrease in the impact strength from 24.1 to 17.3 kJ/m^2 (–28%). This Charpy impact strength drop may be due to the poor adhesion between fibres and matrix, which creates stress concentration. Hence, less energy is required to propagate cracks, initiated at the matrix/fibre interface or in high stress concentration regions. Similar decrease was noticed with 10 wt% of natural fibres (hemp, flax, ramie, cotton) in PLA (Table 5) [28, 32, 44]. Only the addition of synthetic cellulose fibres, Cordenka in PLA, by a completely different processing protocol based on pultrusion, granulation and injection moulding, showed a significant improvement (+170%) of the Charpy impact strength. This may be explained by a worse adhesion between synthetic cellulose fibres and matrix than between natural fibres with PLA. Consequently, the higher number of debondings, pull-outs and fractures of Cordenka fibres will absorb more energy during impact than for the other natural fibres/PLA-biocomposites [32].

As previously shown with the morphology and thermal properties, adding 0.5 wt% of absorbent fine powder does not change the mechanical properties, neither the tensile nor the impact properties of the PLA-biocomposites with 10 wt% cellulose fibres.

Table 4. Mechanical characteristics of PLA and PLA-biocomposites bars

Samples	**χ_c[*] [%]**	**Charpy impact strength [J/m]**	**Young's modulus [MPa]**	**Tensile strength at break [MPa]**	**Tensile strength at yield [MPa]**	**Elongation at break [%]**
PLA-CI	3±1	24.1±5.3	3755±25	63.1±2.9	68.7±2.7	4±1
PLA10F-CI	4±1	17.3±2.2	4426±58	62.6±1.2	65.4±0.8	3±1
PLA10F05Ex-CI	4±1	17.2±1.4	4460±140	62.1±2.0	64.8±0.9	3±1

[*] Crystallinity degree

Mean±standard deviation

Table 5. Mechanical properties of cellulose/PLA biocomposites and comparison with literature data for PLA-biocomposites with 10 wt% of natural fibres prepared according to different protocols. Values are relatives (in %) compared to values of analogous neat PLA samples

Fibre type	**Cellulose content[*] [wt%]**	**Charpy impact strength [%]**	**Young's modulus [%]**	**Tensile strength at yield [%]**	**Elongation at break [%]**	**Reference**
Cellulose	*99.5*	*72*	*118*	*95*	*75*	*This study*
Treated Hemp	70–92	50	102	77	62	[28]
Flax	60–81	62	125	95		[32]
Flax	60–81	66[**]				[44]
Kenaf	45–57		83	112	45	[33]
Ramie	68–76	75[**]				[44]
Cotton	82–96	77[**]				[44]
Recycled cellulose (from newsprint)	75 minimum	82[a,**]	119	97		[43]
Bamboo	26–43		99	71	77	[57]
Cordenka cellulose-based manmade fiber		269	105	113		[32]

[a] Notched Izod

[*] adapted from [58]

[**] calculated by using information reported in figures.

Similar trend was found with zeolites, pozzolan or white clay added to PLA/wood flour biocomposites to reduce the odour and VOCs emission [39]. Natural and synthetic zeolite have an average particle size over 7.7 and 9.7 µm, respectively, whereas pozzolan and white clay have one over 70 µm. Whatever the porous inorganic filler, at 3 wt%, they did not affect the tensile strength of the biocomposite [39]. These observations are opposite to those reported by Yuzay *et al.* [60] for similar filler content added to neat PLA to remove or absorb off-flavours and odours [61]. They found that 1% of zeolite, with an average particle size of 1–2 µm, did not modify the stiffness and the tensile strength whereas a higher content (3 or 5 wt% of zeolites) improves these mechanical characteristics of the material (+20%). They attributed this behaviour to a good enough interfacial adhesion between zeolites and PLA matrix and dispersion of zeolites in PLA [60].

3.9. Global odour analysis

Table 6 presents the results of odour analysis during the different processing stages needed to obtain car interior parts. The testing conditions, i.e. heating at 90°C for 2 h in a confined atmosphere (10 g/L), are based on typical testing requirements of OEM's, and are well adapted for simulating the most severe testing conditions for car interior applications. Results show that rating the global odour on a scale from 0 to 5, according to ISO 5496, is not sensitive enough to allow discrimination between samples. The same observation is noticed for the qualitative aspect of the odour: all the samples have common roasted and fatty odorous notes, except the cellulose that presents a unique fatty note.

At the opposite, dynamic olfactometry according to EN 13725 allows to demonstrate the impact of each processing step as well as the efficiency of the remediation agent.

The global odour concentration of dried raw materials (neat PLA pellets and cellulose fibres) is relatively low, of about 350 $uo_E.m^{-3}$.

The *compounding stage* results in a large increase in odour concentration, for both neat PLA and cellulose fibres/PLA-biocomposites. The odour concentration of compounded PLA pellets (PLA-C) is doubled with respect to the initial dried pellets (dPLA). Furthermore, *adding 10 wt% of cellulose fibres* in PLA matrix increases almost three times the odour concentration with respect to the initial dPLA pellets, despite the expected less odour-emissive nature of the chosen fibres. Indeed, as showed in Figure 4b and 4c, the fibres (99.5% of cellulose) do not significantly degrade in the temperature range used for the compounding stage (170–180°C). Experimental investigations on the nature of the emitted VOCs (not reported here) indicate that this important increase is due to both the PLA degradation and the onset degradation (264°C, Table 2) of cellulose fibres, during the 6 min residence in the extruder at around 180°C and under high shear rate induced by the co-rotating twin-screws at 110 rpm. The effect of these degradations is not only a decrease in molecular weight of PLA (as shown in §3.5), but also the formation and emission of volatile organic compounds (VOCs) with odour activity. The odorant notes emitted by processed neat PLA preconditioned for 2 h at 90 C were described as roasted and fatty, whereas the dried cellulose fibres emitted mainly fatty notes.

Table 6. Odour analysis: cellulose fibres, PLA and PLA-biocomposites (after 2 h at 90°C)

Samples	**Olfactometric measurements according to the European standard EN13725**		**Odour analysis according to ISO 5496 (Champs des odeurs® methodology)**		
	Odour concentration ($uo_E.m^{-3}$)	**Sniffers repeatability ($uo_E.m^{-3}$)**	**Global note***	**Confidence Interval (IC)***	**Odourous notes***
dPLA	355	55	2.6	0.2	Roasted (2.2), fatty (1.1)
dPLA-C	780	0	3.0	0.0	Roasted (2.4), fatty (1.6), rancid (0.9)
PLA-CI	625	130	2.7	0.2	Roasted (1.9), fatty (1.6)
Dried Cellulose fibres	340	90	2.0	0.0	Fatty (1.3)
dPLA10F-C	1025	80	2.6	0.3	Roasted (2.3), fatty (1.6)
PLA10F-CI	1025	80	3.1	0.2	Roasted (2.6), fatty (1.9)
dPLA10F05Ex-C	590	50	2.9	0.3	Roasted (2.5), fatty (1.6)
PLA10F05Ex-CI	660	90	2.8	0.3	Roasted (2.2), fatty (1.9)

*Quotation from 0 to 5: 0 – No perceptible odour; 5 – Outstanding odour on which the person's attention is focused

Quite unexpectedly, the *injection moulding* stage does not generate any additional odour emission, neither for the neat PLA nor for PLA-biocomposites, despite some slight degradation observed for this processing stage.

However, the odour level generated by the final injection moulded parts based on PLA-biocomposites with 10 wt% cellulose fibres requires the use of a remediating agent, for instance a compound able to absorb VOCs and so to entrap them inside the biocomposite. Recently, Kim and coworkers [37–39] proposed adding porous inorganic fillers into polymer biocomposites, to adsorb odour and VOCs. They noticed a significant decrease of VOC concentration with 3% of pozzolan or natural and synthetic zeolites in PLA-biocomposites [39], without affecting negatively the thermal and mechanical properties. The efficiency of pozzolan on VOC emission was also showed at lower content, down to 0.5 wt%, in the case of PP-based biocomposites [37]. Their second approach consisted in a bake-out process, by increasing the air temperature in an unoccupied but fully furnish car while maintaining some ventilation. The bake-out method applied to PLA-biocomposites (70°C for 5 h) allowed reducing by more than 80% the total VOC emission factor. However, Kim *et al.* [38] did not consider the impact of such a treatment on PLA degradation and mechanical performances of PLA parts.

Our own results show the efficiency of a recent absorbent agent, i.e., micrometer sized solid spherical particles made of poly(1-methylpyrrol-2-ylsquaraine), due to their internal amorphous porous network and small size. Indeed, adding only 0.5 wt% of this absorbent agent in PLA/cellulose fibres biocomposites is enough to divide by two the odour concentration of the compounded materials, as compared to the untreated biocomposites. As for the neat PLA and PLA-biocomposite, the injection moulding stage has no additional effect on the odour emission of the PLA-biocomposite with absorbent agent. The main odorant notes of the PLA-biocomposite with absorbent particles do not change, as compared with the untreated biocomposites.

4. Conclusions

Biocomposites parts made of PLA reinforced with 10 wt% of short pure cellulose fibres (99.5% cellulose) were obtained via compounding and injection moulding. The biocomposites exhibited a well-dispersed morphology, but a generally weak adhesion PLA- cellulose fibre.

The incorporation of cellulose fibres in PLA, by compounding in a twin-screw extruder, induced a slight drop of molecular weight of PLA, due to the combined effect of shearing at high temperature and hydrolysis of PLA chains, highly sensitive to the small amount of moisture introduced by the (pre-dried) cellulose fibres. The compounding stage and the second drying cycle caused the main part of PLA degradation, as observed via molecular weight and MFI evolution, while the injection moulding stage had no significant impact.

A clear relation was shown between the increase of odour emission and the polymers degradation after compounding and post-compounding drying stages, for both neat (processed) PLA and PLA-biocomposites. The evolution of global odour concentration and odorant notes after each processing stage was investigated.

Finally, the global odour level of the biocomposite could be reduced by adding an organic absorbent agent (porous spherical beads). Its efficiency at only 0.5 wt% was proved via a decrease in the odour concentration by a factor 2, without impairing the thermal and mechanical properties of the biocomposite. Further researches focusing on the nature of VOCs emitted by PLA-biocomposites are going on.

Acknowledgements

The authors would like to acknowledge INTERREG IV France – Wallonie-VLAANDEREN 2007-2013 (Project SENSOPLAST FW 1.1.2) and International Campus on Safety and Intermodality in Transportation (CISIT), Walloon Region (DGO6), Nord-Pas-de-Calais Region and European Community (FEDER) for financial support. Furthermore, the authors thank Annabelle Cingöz and Anne Borcy (CERTECH, Belgium) for the sensorial analysis, Adrian Boborodea for the SEC analysis (CERTECH, Belgium) and Aurélien Piroelle (Mines Douai, France) for his help in PLA physico-chemical and mechanical analysis.

References

[1] European Commission: Directive 2000/53/EC of the European parliament and the council of 18 Septembre 2000 on end-of-life vehicles. Official Journal of the European Communities (2000).

[2] Rusu D., Boyer S. A. E., Lacrampe M. F., Krawczak P.: Bioplastics and vegetal fiber reinforced bioplastics for automotive applications. in 'Handbook of bioplastics and biocomposites engineering applications' (Ed.: Pilla S.), Wiley-Scrivener, Weinheim, 397–448 (2011).
DOI: 10.1002/9781118203699.ch15

[3] Thouzeau C., Henneuse C., Sclavons M., Devaux J., Soulestin J., Stoclet G.: Emission of volatile organic compounds during processing and use of organoclay-based nanocomposites. Polymer Degradation and Stability, **98**, 557–565 (2013).
DOI: 10.1016/j.polymdegradstab.2012.11.019

[4] Kolstad J. J.: Crystallization kinetics of poly(L-lactide-*co*-*meso*-lactide). Journal of Applied Polymer Science, **62**, 1079–1091 (1996).
DOI: 10.1002/(SICI)1097-4628(19961114)62:7<1079::AID-APP14>3.0.CO;2-1

[5] Kalia S., Avérous L., Domenek S., Courgneau C., Ducruet V.: Characteristics and applications of poly (lactide). in 'Biopolymers: Biomedical and environmental applications' (Eds.: Kalia S., Avérous L.) Wiley, Weinheim, 183–224 (2011).
DOI: 10.1002/9781118164792.ch8

[6] Ramy-Ratiarison R., Soulestin J., Lacrampe M. F., Krawczak P.: Peculiar crystallization behaviour of injection-molded PLA parts. in 'Proceedings of the 3rd International Conference on Biodegradable and Biobased Polymers, BIOPOL 2011, Strasbourg, France' O–079 (2011).

[7] Julien J-M., Bénézet J-C., Lafranche E., Quantin J. C., Bergeret A., Lacrampe M. F., Krawczak P.: Development of poly(lactic acid) cellular materials: Physical and morphological characterizations. Polymer, **53**, 5885–5895 (2012).
DOI: 10.1016/j.polymer.2012.10.005

[8] Lim L-T., Auras R., Rubino M.: Processing technologies for poly(lactic acid). Progress in Polymer Science, **33**, 820–852 (2008).
DOI: 10.1016/j.progpolymsci.2008.05.004

[9] Tessier R., Lafranche E., Krawczak P.: Development of novel melt-compounded starch-grafted polypropylene/polypropylene-grafted maleic anhydride/organoclay ternary hybrids. Express Polymer Letters, **6**, 937–952 (2012).
DOI: 10.3144/expresspolymlett.2012.99

[10] Lafranche E., Krawczak P., Ciolczyk J-P., Maugey J.: Injection moulding of long glass fiber reinforced polyamide 66: Processing conditions/microstructure/flexural properties relationship. Advances in Polymer Technology, **24**, 114–131 (2005).
DOI: 10.1002/adv.20035

[11] Lafranche E., Krawczak P., Ciolczyk J. P., Maugey J.: Injection moulding of long glass fibre reinforced polyamide 6-6: Guidelines to improve flexural properties. Express Polymer Letters **1**, 456–466 (2007).
DOI: 10.3144/expresspolymlett.2007.64

[12] Cilleruelo L., Lafranche E., Krawczak P., Pardo P., Lucas P.: Injection moulding of long glass fibre reinforced poly(ethylene terephtalate): Influence of carbon black and nucleating agents on impact properties. Express Polymer Letters, **6**, 706–718 (2012).
DOI: 10.3144/expresspolymlett.2012.76

[13] Martins C. I., Lemos-Oliveira V. M., Lafranche E.: Processing, mechanical properties and morphology of injection moulding flax fibres reinforced polypropylene. in 'Proceedings of POLYCHAR 20, World Forum on Advanced Materials, Dubrovnik, Croatia', O 2–023 (2012).

[14] Kovács J. G., Soulestin J., Tábi T., Ramy-Ratiarison R., Lafranche E., Lacrampe M-F., Czigány T., Krawczak P.: Overall characterization of cellulose fiber reinforced PLA. in 'Proceedings of the 4th China-Europe Symposium on Processing and Properties of Reinforced Polymers, Guilin, China' O–085 (2009).

[15] Soulestin J., Quiévy N., Sclavons M., Devaux J.: Polyolefins–biofibre composites: A new way for an industrial production. Polymer Engineering and Science, **47**, 467–476 (2007).
DOI: 10.1002/pen.20706

[16] Senthil Kumar K., Lafranche E., Lacrampe M. F., Krawczak P.: Injection moulding of flax fibre-reinforced polypropylene: Influence of processing conditions on tensile and impact strengths. in 'Proceedings of the 25th Annual Meeting of the Polymer Processing Society, Symposium on Polymer Composites, Goa, India' GS-III:O7 (2009).

[17] Holbery J., Houston D.: Natural-fiber-reinforced polymer composites in automotive applications. Journal of the Minerals. Metals and Materials Society, **58**, 80–86 (2006).
DOI: 10.1007/s11837-006-0234-2

[18] van Voorn B., Smit H. H. G., Sinke R. J., de Klerk B.: Natural fibre reinforced sheet moulding compound. Composites Part A: Applied Science and Manufacturing, **32**, 1271–1279 (2001).
DOI: 10.1016/S1359-835X(01)00085-9

[19] Suddell B. C., Evans W. J.: Natural fiber composites in automotive applications. in 'Natural fibers, biopolymers and biocomposites' (Eds.: Mohanty A. K., Misra M., Drzal L. T.) CRC Press, Boca Raton, 237–266 (2005).
DOI: 10.1201/9780203508206.ch7

[20] Summerscales J., Dissanayake N., Virk A, Hall W.: A review of bast fibres and their composites. Part 2 – Composites. Composites Part A: Applied Science and Manufacturing, **41**, 1336–1344 (2010).
DOI: 10.1016/j.compositesa.2010.05.020

[21] Bledzki A. K., Faruk O., Sperber V. E.: Cars from biofibres. Macromolecular Materials and Engineering, **291**, 449–457 (2006).
DOI: 10.1002/mame.200600113

[22] Yang H., Yan R., Chen H., Lee D. H., Zheng C.: Characteristics of hemicellulose, cellulose and lignin pyrolysis. Fuel, **86**, 1781–1788 (2007).
DOI: 10.1016/j.fuel.2006.12.013

[23] Gassan J., Bledzki A. K.: Thermal degradation of flax and jute fibers. Journal of Applied Polymer Science, **82**, 1417–1422 (2001).
DOI: 10.1002/app.1979

[24] Ellison G. C., McNaught R., Eddleston E. P.: The use of natural fibres in nonwoven structures for applications as automotive component substrates. Ministry of Agriculture Fisheries and Food Agri-Industrial Materials, Research and development report (2000).

[25] Oksman K., Skrifvars M., Selin J-F.: Natural fibres as reinforcement in polylactic acid (PLA) composites. Composites Science and Technology, **63**, 1317–1324 (2003).
DOI: 10.1016/S0266-3538(03)00103-9

[26] Bodros E., Pillin I., Montrelay N., Baley C.: Could biopolymers reinforced by randomly scattered flax fibre be used in structural applications? Composites Science and Technology, **67**, 462–470 (2007).
DOI: 10.1016/j.compscitech.2006.08.024

[27] Akil H. M., Omar M. F., Mazuki A. A. M., Safiee S., Ishak Z. A. M., Abu Bakar A.: Kenaf fiber reinforced composites: A review. Materials and Design, **32**, 4107–4121 (2011).
DOI: 10.1016/j.matdes.2011.04.008

[28] Masirek R., Kulinski Z., Chionna D., Piorkowska E., Pracella M.: Composites of poly(L-lactide) with hemp fibers: Morphology and thermal and mechanical properties. Journal of Applied Polymer Science, **105**, 255–268 (2007).
DOI: 10.1002/app.26090

[29] Mathew A. P., Oksman K., Sain M.: The effect of morphology and chemical characteristics of cellulose reinforcements on the crystallinity of polylactic acid. Journal of Applied Polymer Science, **101**, 300–310 (2006).
DOI: 10.1002/app.23346

[30] Gregorova A., Sedlarik V., Pastorek M., Jachandra H., Stelzer F.: Effect of compatibilizing agent on the properties of highly crystalline composites based on poly (lactic acid) and wood flour and/or mica. Journal of Polymers and the Environment, **19**, 372–381 (2011).
DOI: 10.1007/s10924-011-0292-6

[31] Graupner N., Herrmann A. S., Müssig J.: Natural and man-made cellulose fibre-reinforced poly(lactic acid) (PLA) composites: An overview about mechanical characteristics and application areas. Composites Part A: Applied Science and Manufacturing, **40**, 810–821 (2009).
DOI: 10.1016/j.compositesa.2009.04.003

[32] Bax B., Müssig J.: Impact and tensile properties of PLA/Cordenka and PLA/flax composites. Composites Science and Technology, **68**, 1601–1607 (2008).
DOI: 10.1016/j.compscitech.2008.01.004

[33] Pan P., Zhu B., Kai W., Serizawa S., Iji M., Inoue Y.: Crystallization behavior and mechanical properties of bio-based green composites based on poly(L-lactide) and kenaf fiber. Journal of Applied Polymer Science, **105**, 1511–1520 (2007).
DOI: 10.1002/app.26407

[34] Mathew A. P., Oksman K., Sain M.: Mechanical properties of biodegradable composites from poly lactic acid (PLA) and microcrystalline cellulose (MCC). Journal of Applied Polymer Science, **97**, 2014–2025 (2005).
DOI: 10.1002/app.21779

[35] Cingoz A., Borcy A., Henneuse C., Piroelle A., Rusu D., Lacrampe M. F., Salazar R., Krawczak P., Ducruet V.: Odour and VOC emissions from PLA materials: Effect of processing. in '2nd International Meeting on Material/Bioproduct Interaction, MATBIM 2012, Dijon, France' O–57 (2012).

[36] Cingoz A., Borcy A., Henneuse C., Piroelle A., Courgneau C., Lacrampe M. F., Salazar R., Krawczak P., Ducruet V.: Odour and VOC emissions from PLA materials: Food packaging and automotive applications. in 'Proceedings of the 10th Edition „Emissions and odours from materials", Bruxelles, Belgium' O 3–3 (2012).

[37] Kim H-S., Kim S., Kim H-J., Kim H-G.: Physico-mechanical properties, odor and VOC emission of bio-flour-filled poly(propylene) bio-composites with different volcanic pozzolan contents. Macromolecular Materials and Engineering, **291**, 1255–1264 (2006).
DOI: 10.1002/mame.200600212

[38] Kim K-W., Lee B-H., Kim S., Kim H-J., Yun J-H., Yoo S-E., Sohn J. R.: Reduction of VOC emission from natural flours filled biodegradable bio-composites for automobile interior. Journal of Hazardous Materials, **187**, 37–43 (2011).
DOI: 10.1016/j.jhazmat.2010.07.075

[39] Kim H-S., Lee B-H., Kim H-J., Yang H-S.: Mechanical–thermal properties and VOC emissions of natural-flour-filled biodegradable polymer hybrid bio-composites. Journal of Polymers and the Environment, **19**, 628–636 (2011).
DOI: 10.1007/s10924-011-0313-5

[40] Fischer E. W., Sterzel H. J., Wegner G.: Investigation of the structure of solution grown crystals of lactide copolymers by means of chemical reactions. Kolloid-Zeitschrift und Zeitschrift für Polymere, **251**, 980–990 (1973).
DOI: 10.1007/BF01498927

[41] Jaubert J. N., Tapiero C., Dore J. C.: The field of odors: Toward a universal language for odor relationships. Perfumer and Flavorist, **20**, 1–16 (1995).

[42] Frone A. N., Berlioz S., Chailan J-F., Panaitescu D. M., Donescu D.: Cellulose fiber-reinforced polylactic acid. Polymer Composites, **32**, 976–985 (2011).
DOI: 10.1002/pc.21116

[43] Huda M. S., Mohanty A. K., Drzal L. T., Schut E., Misra M.: 'Green' composites from recycled cellulose and poly(lactic acid): Physico-mechanical and morphological properties evaluation. Journal of Materials Science, **40**, 4221–4229 (2005). DOI: 10.1007/s10853-005-1998-4

[44] van den Oever M. J. A., Beck B., Müssig J.: Agrofibre reinforced poly(lactic acid) composites: Effect of moisture on degradation and mechanical properties. Composites Part A: Applied Science and Manufacturing, **41**, 1628–1635 (2010). DOI: 10.1016/j.compositesa.2010.07.011

[45] Wang Y., Steinhoff B., Brinkmann C., Alig I.: In-line monitoring of the thermal degradation of poly(L-lactic acid) during melt extrusion by UV-vis spectroscopy. Polymer, **49**, 1257–1265 (2008). DOI: 10.1016/j.polymer.2008.01.010

[46] Carrasco F., Pagès P., Gámez-Pérez J., Santana O. O., Maspoch M. L.: Processing of poly(lactic acid): Characterization of chemical structure, thermal stability and mechanical properties. Polymer Degradation and Stability, **95**, 116–125 (2010). DOI: 10.1016/j.polymdegradstab.2009.11.045

[47] Pillin I., Montrelay N., Bourmaud A., Grohens Y.: Effect of thermo-mechanical cycles on the physico-chemical properties of poly(lactic acid). Polymer Degradation and Stability, **98**, 321–328 (2008). DOI: 10.1016/j.polymdegradstab.2007.12.005

[48] Jakab E., Mészáros E., Borsa J.: Effect of slight chemical modification on the pyrolysis behavior of cellulose fibers. Journal of Analytical and Applied Pyrolysis, **87**, 117–123 (2010). DOI: 10.1016/j.jaap.2009.10.012

[49] Magoń A., Pyda M.: Study of crystalline and amorphous phases of biodegradable poly(lactic acid) by advanced thermal analysis. Polymer, **50**, 3967–3973 (2009). DOI: 10.1016/j.polymer.2009.06.052

[50] Zuza E., Ugartemendia J. M., Lopez A., Meaurio E., Lejardi A., Sarasua J-R.: Glass transition behavior and dynamic fragility in polylactides containing mobile and rigid amorphous fractions. Polymer, **49**, 4427–4432 (2008). DOI: 10.1016/j.polymer.2008.08.012

[51] Delpouve N., Saiter A., Dargent E.: Cooperativity length evolution during crystallization of poly(lactic acid). European Polymer Journal, **47**, 2414–2423 (2011). DOI: 10.1016/j.eurpolymj.2011.09.027

[52] Righetti M. C., Tombari E.: Crystalline, mobile amorphous and rigid amorphous fractions in poly(L-lactic acid) by TMDSC. Thermochimica Acta, **522**, 118–127 (2011). DOI: 10.1016/j.tca.2010.12.024

[53] Courgneau C., Domenek S., Lebossé R., Guinault A., Avérous L., Ducruet V.: Effect of crystallization on barrier properties of formulated polylactide. Polymer International, **61**, 180–189 (2012). DOI: 10.1002/pi.3167

[54] Guinault A., Sollogoub C., Ducruet V., Domenek S.: Impact of crystallinity of poly(lactide) on helium and oxygen barrier properties. European Polymer Journal, **48**, 779–788 (2012). DOI: 10.1016/j.eurpolymj.2012.01.014

[55] Pan P., Inoue Y.: Polymorphism and isomorphism in biodegradable polyesters. Progress in Polymer Science, **34**, 605–640 (2009). DOI: 10.1016/j.progpolymsci.2009.01.003

[56] De Rosa I. M., Iannoni A., Kenny J. M., Puglia D., Santulli C., Sarasini F., Terenzi A.: Poly(lactic acid)/*phormium tenax* composites: Morphology and thermo-mechanical behavior. Polymer Composites, **32**, 1362–1368 (2011). DOI: 10.1002/pc.21159

[57] Lee S-H., Wang S.: Biodegradable polymers/bamboo fiber biocomposite with bio-based coupling agent. Composites Part A: Applied Science and Manufacturing, **37**, 80–91 (2006). DOI: 10.1016/j.compositesa.2005.04.015

[58] Bismarck A., Mishra S., Lampke T.: Plant fibers as reinforcement for green composites. in. 'Natural fibers, biopolymers and biocomposites' (Eds.: Mohanty A. K., Misra M., Drzal L. T) CRC Press, Boca Raton, 37–108 (2005).

[59] Qiu W., Zhang F., Endo T., Hirotsu T.: Preparation and characteristics of composites of high-crystalline cellulose with polypropylene: Effects of maleated polypropylene and cellulose content. Journal of Applied Polymer Science, **87**, 337–345 (2003). DOI: 10.1002/app.11446

[60] Yuzay I. E., Auras R., Selke S.: Poly(lactic acid) and zeolite composites prepared by melt processing: Morphological and physical–mechanical properties. Journal of Applied Polymer Science, **115**, 2262–2270 (2010). DOI: 10.1002/app.31322

[61] Auras R., Selke S., Yuzay I. E.: Poly(lactic acid) and zeolite composites and method of manufacturing the same. U.S. Patent 20100236969 A1, USA (2010).